Title

EQUILIBRATION IN THE REACTION OF 175 and 252 MeV 20Ne WITH 197Au

Author

Moulton, James Bennett

Publication Date

1978-06-01

LBL-7717

EQUILIBRATION IN THE REACTION OF 175 AND 252 MeV ^{20}Ne WITH ^{197}Au

James Bennett Moulton
(Ph.D. thesis)

June 1978

Lawrence Berkeley Laboratory

University of California
Berkeley, California 94720

Work performed under the auspices of the U.S. Department of Energy

Contents

ABSTRACT

The highly inelastic nuclear reaction of ^{197}Au with ^{20}Ne at 175 and 252 MeV laboratory energies is studied. Energy-, elemental-, and angular- distributions for atomic numbers 5 to 30 (175 MeV) or 34 (252 MeV) are presented.

The means and widths of the kinetic energy spectra for detected elements are compared with a theoretical calculation. The calculation postulates thermalization of the incident projectile kinetic energy, and includes one shape-vibrational degree of freedom and rigid rotation of the reaction complex. The effect of particle evaporation is considered. Good agreement of the experimental mean energies with the theory is obtained. Poorer agreement of the kinetic energy widths with the theory may be due to a low-temperature quantal effect.

The relative elemental yields are analyzed for their degree of equilibration, based on a model of diffusive nucleon exchange as described by the master equation. A similar degree of equilibration is observed for both reaction energies. The absolute elemental yields are reproduced qualitatively by employing an advanced diffusion code, coupled with calculation of the subsequent fission of heavy reaction products, including the compound nucleus.

The angular distributions are analyzed with a simple model, to estimate the reaction lifetime of selected elements.

ACKNOWLEDGMENTS

It is a pleasure to acknowledge the many people who have contributed to my education here at Berkeley, and to the development and completion of this thesis. I am especially indebted to:

Dr. Luciano G. Moretto, my thesis advisor, for opening to me the breadth of his knowledge and the many accomplishments of his research group. The years under his direction are unforgettable, and a great privilege. Without his serious commitment to the pursuit of excellence in science, this work would be even farther from that goal than it presently is.

Dr. Gordon J. Wozniak, my collaborator in parts of this thesis, for trying to transfer to me his considerable skill and patience as an experimentalist.

Doctors Joel Galen and Regis Babinet, former post-doc's, for gently inoculating me with some of my first doses of nuclear physics.

Richard P. Schmitt and Joseph S. Sventek, my peers, for being good fellows and for being in the same boat.

James B. Hunter and Richard C. Jared for top-flight assistance with everything electronic and mechanical, and to the faithful crews of the 88" Cyclotron for providing beams at all hours of day and night.

And finally, to my wife Miriam, for being my wife Miriam as well as a whole lot more.

Chapter I. Introduction

Viewed from a historical perspective, a distinctive and exacting feature of modern science is its overwhelming commitment to the process of induction. Contemplative deduction -- the view from the mountain top -- is relegated to a quite small though crucial segment of the scientist's endeavor. Needle-like specialization is a direct result of the contemporary investigator's thorough skepticism of his ability to understand the physical world from his intuition alone. As Sherlock Holmes is reported to have said, "It is a capital mistake to theorize before one has data". While engaged in the gargantuan task of collecting sufficient data, the scientist must never forget the ancient admonition that "Scientific knowledge is not possible through the act of perception. ... for perception must be of a particular, whereas scientific knowledge involves the recognition of the commensurate universal." (Ar 00).

In this light, the present thesis is scant indeed in scientific knowledge. It is a study of the extent of equilibration in two examples of highly inelastic heavy ion reactions. A measure of the knowledge contained is to be found in the selection and development of physical models and theories which may prove useful in further study of the atomic nucleus or other subjects displaying similar processes.

Highly inelastic reactions are characterized by transfer of a large fraction of the initial kinetic energy of the projectile to internal degrees of freedom of the reaction complex. Nucleon transfer between the reacting nuclei also occurs, and may result in significant mass change. These features dramatically distinguish highly inelastic reactions from direct reactions by involving a huge number of states in the reaction. When it is possible to identify individual modes such as with shape oscillations or particle transfer within the reaction complex, they can usually be handled most readily in the context of a macroscopic, phenomenological model rather than in a fundamental manner (Co 63, Ni 65, Ni 67, Ni 69).

While this treatment of reaction modes arises from the difficulty of identifying or keeping track of the vast number of underlying single-particle degrees of freedom, this certainly need not be seen as a limitation on the scientific utility of highly inelastic reactions. On the contrary, the complexity of such reactions is in fact a doorway to understanding properties of nuclear matter which we know little about from spectroscopic studies alone. These reactions allow one to explore such areas as the mechanisms and dynamics leading to transfer of large amounts of nuclear matter, collective nuclear motion like vibration and rotation, statistical nuclear properties such as particle emission, and the systematics of fission at high temperatures.

In the present analysis of equilibration in the Ne + Au reaction, a specific well known reaction model is used throughout (Mo 75). Upon collision of the reacting nuclei, the initial relative motion is quickly damped and the pair assumes a sticking configuration in which the identity of the two nuclei is preserved. The pair rotates about their collective center of mass, and undergoes shape vibrations. Energy flows between the nuclei, and they exchange nucleons through the contact area. Eventually, the pair breaks apart. The energy of the resulting fragments arises from the Coulomb repulsion between them and from their centrifugal acceleration. The distribution of atomic numbers is determined by the distribution of lifetimes of the complex and by the rate of exchange of nucleons between the nuclei. The potential energy and temperature which govern this nucleon exchange can be calculated with a liquid drop model.

The popularity of this picture of the interaction arises from the ease with which it can be quantified, and the versatility with which it can incorporate many factors participating in the reaction. Such factors include the range of angular momenta which contribute to the reaction cross section, (Bl 72, Ca 74, Ga 74), the possibility of fluid or rigid motion of the nuclei and specific collective modes like the giant resonance (My 77).

An important limitation to the model must be recognized in its ability to account for only one pathway for the formation of a compound nucleus. (Complete absorption of one nucleus by the other, by stepwise transfer of nucleons). A compound nucleus is by definition a fully equilibrated species. Since the sticking-nuclei model described above is able to encompass all degrees of equilibration, excluding the direct fusion reaction pathway would seem to be a small loss. Indeed this is the root of the difficulty in distinguishing experimentally between the two reaction mechanisms. The deficiency in not considering the direct fusion-fission channel lies in the fact that its dynamics may be quite different from those of a reaction in which the nuclei retain their identity (Sw 72).

Direct observation of reaction dynamics is unfortunately impossible; only clues are available. The most promising experimental access to the reaction dynamics is inference of the internal angular momentum of the reaction products through measuring their gamma-ray multiplicities (for instance see Ma 74, Al 77, Gl 77). With this technique one could perhaps produce evidence for a different angular momentum range (and thus a different reaction mechanism) for products heavy enough to have come from fission, from lighter products only somewhat different in mass from the projectile. Such information is not available for the reaction under study.

With the data which have been taken on the Ne + Au reaction, resolution of the reaction-pathway problem is highly unlikely. Nor is selection between alternative mechanisms for the specific processes involved in the reaction (charge transfer, energy damping) likely to be possible. This thesis therefore concentrates on examining, in a phenomenological way, the degree to which equilibration is attained in several degrees of freedom of the reaction, rather than on determining the processes through which the reaction proceeds.

Chapter II. Experimental Facilities and Data Analysis

A. Experimental Facilities

1. Ion Beam and Detection System

The experiments described in this thesis, were performed at the Lawrence Berkeley Laboratory's 88-Inch Cyclotron. This is a variable energy, sector-focussed machine (Ke 62). The maximum energy of the machine is 140 Q^2/A, where Q is the ion charge and A its mass number. Beams of 175 and 252 MeV $^{20}Ne^{6+}$ ions were utilized. Although obtained at lower intensity, the $^{20}Ne^{6+}$ 175 MeV beam was preferred over the $^{20}Ne^{5+}$ beam to avoid possible contamination by $^{16}O^{4+}$ or $^{12}C^{3+}$ beams, which have the same Q/A ratio. The beams were generated in a Phillip's Ion Gauge (PIG) Source.

The ion beam was electrostatically extracted from the cyclotron and directed to the experimental area through a series of bending and focussing magnets. The typical beam current on target was 100 nano-amperes (Ne^{+10}). The dimensional cross section of the beam on the target was circular, and approximately 3 mm in diameter. Pressure in the scattering chamber was maintained by a turbomolecular pump at about 2×10^{-4} torr. The self-supporting Au targets were from 0.8 to 0.9 mg/cm^2 in thickness. Two rotating arms in the scattering chamber each held one particle detector telescope. These were positioned on opposite sides of the chamber with the front surface typically 6 cm from the target, and at angles ranging from 25° to 150° from the beam axis.

Reaction products were detected with compound "E-ΔE" detector telescopes. A schematic drawing is shown in Fig. 1. A fraction of the

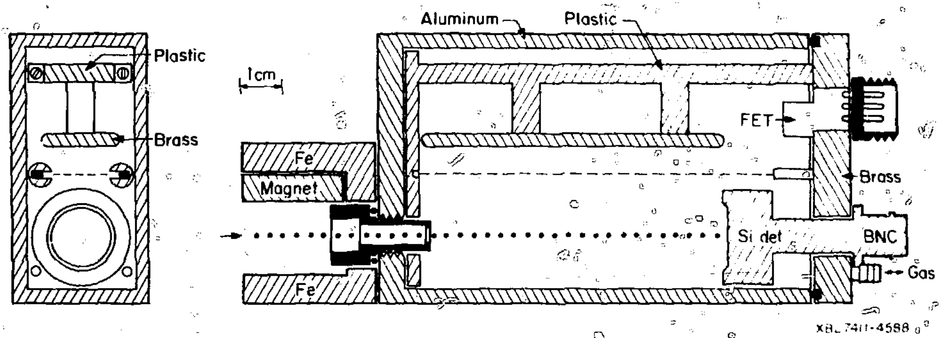

Fig. 1 Schematic diagram of E-ΔE detector telescope.

energy (less than 25%) was deposited in the ΔE ionization counter. This counter is described in Fo 74. The counter was fed with pure methane gas. The flow rate was about 100 cm^3/minute. The gas pressure in the counter ranged from 4 to 8 cm of Hg, was monitored by mercury and oil manometers, and was regulated by a Cartesian manostat. The thicknesses of the gas corresponding to these operating pressures and for a detector length of 6 cm are 0.24 and 0.48 mg/cm^2 of methane, respectively. A 0.050 mg/cm^2 plastic window (FORMVAR or VYNS) was glued on the entrance window of the counter to insulate the pressurized counter from the evacuated scattering chamber.

After traversing the active region of the ΔE counter, the ion deposits the rest of its energy in a thick Si surface barrier detector (the "E" counter), positioned in the back of the ΔE counter housing (See Fig. 1). The E counters were fully reverse biased, producing a charge-carrier-depleted collection region 300 μm thick. The detector is circular with 1 cm diameter.

2. Electronics

A schematic diagram of the electronics is shown in Fig. 2. Four charge-sensitive pre-amplifiers, positioned outside the scattering chamber, amplified the primary pulses originating at each of the detectors (one ΔE and one E signal from each detector telescope), for transmission to the main amplifiers several hundred feet away. The first amplification stage of each ΔE preamplifier was located in the detector housing. These main amplifiers are moduler units employing double-delay-line pulse shaping. Bipolar pulses of 4 micro-second

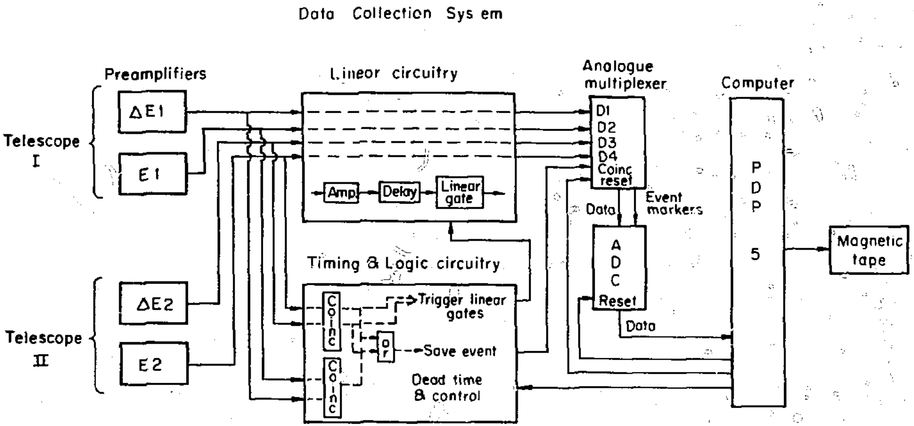

XBL 737-3334A

Fig. 2 Schematic diagram of electronic data collection system.

total duration were typically used. Coincidence timing between the ΔE and E signals from the same detector was effected with constant-fraction discriminators. Coincidence was required between logical pulses typically 0.5 micro-seconds wide. A central "OR" gate driven by the coincidence signals from the two E-ΔE telescopes was used for control and triggering of data transmission to the computer. At angles for which the rate of elastic events was large, a single channel analyzer (SCA) was sometimes used to exclude those events from transmission to the computer. Digital scalars driven by SCA and coincidence logic pulses were used for measuring the system percent live time (typically 70 to 90%). An analogue multiplexer was used to time-stretch data pulses which satisfied the SCA and coincidence requirements. This unit fed the analogue signals sequentially to a 4096-channel analogue-to-digital-converter, which transformed the data pulses to digital form and transferred them to a PDP-5 computer to be written on magnetic tape.

B. Data Analysis

1. Calibrations

The solid-angular efficiency of the detector telescope, defined by the window aperture, was measured by irradiating the detector for five minutes with an alpha-emitting ^{241}Am source of 9.77 μCi activity. Solid angular efficiencies of 0.00015 were usually obtained, corresponding to 0.0019 steradians.

Energy calibration of the solid-state E counter was obtained in a two step process. First a linear mercury pulser was calibrated with a ^{241}Am source, emitting alpha particles of 5.486 MeV average energy and 40 keV width. The pulser was then used to produce 5 or 6 peaks spaced throughout the dynamic range of each amplifier system, at each gain setting. The channel numbers of these peaks were fit, as a function of pulser amplitude, to a straight line by a linear least-squares method. Finally, the alpha-particle calibration of the pulser was used to produce an energy calibration equation. The calibration equation was checked against the elastically scattered projectile at known angle, whose spectrum was taken with no gas in the ΔE counter and no plastic window at the front aperture. Small adjustments to the calibration equation were sometimes necessary, the final accuracy of the calibration equation being ± 0.5 MeV.

The energy calibration of the ΔE counter was obtained in two stages. The mercury pulser was used to produce 5 or 6 peaks spaced throughout the dynamic range of the ΔE amplifier system. A straight-line fit relating pulser setting to channel number was obtained. Then, having prepared the energy calibration equation of the E counter, one completes the calibration equation for the ΔE counter as follows. The detector was set at a fixed angle forward of the projectile grazing angle. The elastic spectrum was collected with no gas in the ΔE detector, and the energy deposited in the E counter is computed. With the detector at the same angle, the ΔE counter was pressurized and the elastic spectrum collected again. The elastic energy deposited in the E counter was again computed, and was less than in the "no-gas" case -- the difference in the energy having been deposited in the ΔE counter.

The ΔE channel at which the elastic peak appeared was determined. The final energy calibration line was obtained by multiplying the fitted pulser calibrated line by an appropriate factor to relate the ΔE elastic channel to the elastic energy known to have been deposited in the ΔE counter.

A note on dead layer corrections. Two corrections to the energies were necessary in performing the above calibrations, and in computing the energy of actual data events. It was necessary to account for the energy lost in the target iself, and in the plastic window on the ΔE counter. In computing the elastic energy for calibration calculations, it was assumed that the scatter event took place midway through the target. The Northcliffe-Schilling stopping power tables (No 70) were used to evaluate the degradation of the energy of the projectile over its full path in the target, taking account of the angle at which it energes from the target. Energy lost in the plastic window was also calculated. For correcting the energy of detected reaction products, it was assumed that the interaction took place midway through the target. These corrections are most important for high Z's detected at low energies, and may be as much as 10% or even 20% of the total energy. In most cases, the energy corrections are less than 5% of the measured energy.

2. Data Analysis Procedure

The procedure for reduction of the primary data to useful form proceeds in four stages. Each data event exists on magnetic tape as two channel numbers -- one from the ΔE and one from the E detector.

In the first stage of analysis, a two-dimensional spectrum is computed: one axis is the ΔE channel number and the other axis is the E channel number. One such "E-ΔE map" is computed for each gain setting at each angle. This map is stored on magnetic tape. An example of such a map from the reaction of Ar + Ag is displayed in Fig. 3. The slanted ridges are clusters of events of the same atomic number. From such a map one is able to compute the yield and energy spectrum for each element at the laboratory angle at which the data was collected. The ridge corresponding to events of the same atomic number as the projectile is identified by the greater yield, the presence of an elastic peak, or the presence of low energy projectile events resulting from multiple scattering on the collimating slits. The atomic number for all other ridges is then known.

In the second stage of the data analysis, the ridges on each map are identified and fitted with fifth-order polynomials (called "ridge lines") which are functions of the E coordinate. A detailed discussion of the computerized interactive ridge-hunting procedure can be found in Gl 76.

In the third stage of the analysis, energy spectra for each element at each angle are computed in both the laboratory and center-of-mass (CM) reference frames. Ridge lines are overlayed on each map, and "valley lines" midway between each successive ridge line are computed. A "Z-bin" is defined as that region on the map between two successive valley lines. All events within each Z-bin are ascribed to the element whose ridge line is enclosed within the Z-bin. Even if the yield of successive ridges overlap, as in the high-Z range of

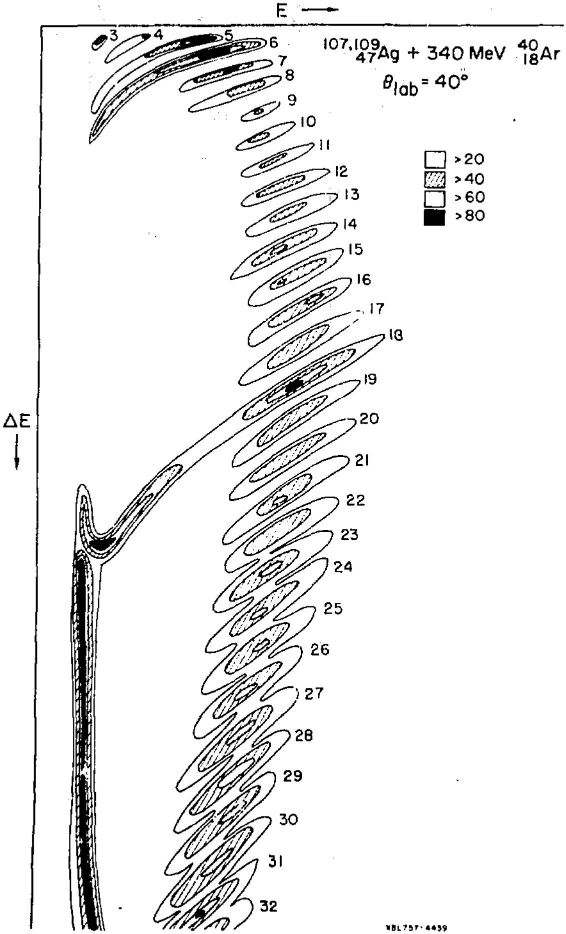

Fig. 3 Two-dimensional "E-ΔE map" from the reaction Ar + Ag. Ridges are clusters of events of the elements indicated to the right of each ridge.

of Fig. 3, this procedure is quite accurate as long as the yield does not vary greatly from one element to the next. The laboratory energy of each event in each Z-bin is computed using the calibration equations and dead layer correction procedures discussed in section II.B.1. Transformation of the spectra to the CM frame requires knowledge of the mass of each fragment. The mass is obtained from a charge-equilibrium model. The total mass and overall neutron-to-proton ratio is fixed. That partition of neutrons is computed which minimizes the ground state mass, as a function of the atomic number of one fragment. No evaporation of particles is considered. This entire stage is completely computerized. An evaluation of alternative procedures for choosing the mass is presented elsewhere (Ba 75, Ga 75).

In the fourth and final stage of primary data analysis, the CM energy spectra just prepared are edited, when necessary, to remove spurious or unwanted peaks arising from elastic events, or low-energy high-Z "turn over" events (the high intensity vertical ridge at low energy parallel to the data in Fig. 3). The energy spectra are then integrated, and the first and second moments computed. Also the mean CM angle for each spectrum is calculated. CM angular distributions are plotted for each element by ascribing the cross section at each laboratory angle to the mean CM angle for the Z. Except where the measured cross section varies greatly with angle, this procedure introduces little error. The spectrum editing and moment-calculation is done interactively with a computer.

Chapter III. Results and Discussion

A. Energy Spectra

1. Introduction - Internal Energy, Temperature, Degeneracy

Before entering the thicket of a detailed discussion of the energy aspects of the Ne + Au reaction, it is worthwhile to develop the concepts of internal energy and temperature, as they apply to reacting nuclear systems.

We shall begin by defining the internal energy. The products of highly inelastic reactions display kinetic energies which apparently arise from the Coulomb repulsion and centrifugal acceleration of the complex at breakup. The final kinetic energy is largely decoupled from -- and far less than -- the entrance channel kinetic energy. (A quantitative treatment of this phenomenon will be given in the next section). In this way a large amount of energy is made available, during the reaction, for excitation of modes other than collective relative motion of the reacting nuclei. This "internal" energy must be distributed, perhaps thermally, among single particle states, collective vibrations and rotations and transfer of nucleons between the two nuclei.

It is difficult to ascertain that the internal energy is in fact distributed statistically among the available modes. A nuclear reaction of the type we are studying here can hardly be said to be an equilibrium process. One must imagine it as a collision whose dynamics are quite important to the details of the event. If, however, the time required for transfer of the initial kinetic energy to the internal modes is small compared to the reaction time, the concept of energy thermalization seems relevant.

One can define the internal energy, U, available to a thermalized system at the time of breakup as

$$U = E_{cm} + Q_{g.s.} - V_{rot} - \Delta V_{sur} - \Delta V_{sc} - V_{Coul}$$

where:

E_{cm} = center of mass kinetic energy, $Q_{g.s.}$ = ground state mass change from initial to final configuration. One envisions the reacting nuclei retaining their identity during the reaction. V_{rot} = total rigid rotational energy of the reaction complex. Possible elastic or fluid contributions to the moment of inertia have been ignored. ΔV_{sur} = (positive) change in the surface energy of both fragments, above the spherical value, due to deformation of the touching nuclei to equlibrium shape (defined as that shape which minimizes the total potential energy). ΔV_{sc} = (negative) change in the self Coulomb energy of both fragments below the spherical value, due to deformation to equilibrium shape. V_{Coul} = Coulomb repulsion between the two nuclei at equilibrium deformation.

It must be understood that the last four potential energy terms are evaluated at equilibrium deformation of the touching pair of nuclei. Aside from this, subtraction of the total rigid rotational energy is an approximation. One can argue that collective rotation is built from single particle states which are very much a part of the internal excitation energy -- before the collision the nuclei were in their ground states. One must realize however, that the requirement of angular momentum conservation forces the nuclei to keep a certain amount of energy in the rotational mode, regardless of the degree of thermalization and of the amount of energy in other modes. The total rigid rotational energy is an approximation to this "frozen" energy.

Examination of Fig. 4 gives some feeling for the magnitude of internal energy present in the Ne + Au system. This figure shows, for both projectile energies, the total internal energy shared by the two nuclei during the reaction. The abscissa is the atomic number, Z_1, of one fragment. The typical internal energy at the lower projectile energy is about 70 MeV, or 0.32 MeV/nucleon. At the higher projectile energy the typical internal energy is about 125 MeV, or 0.58 MeV/nucleon.

Nearly all of the internal energy is deposited in the single particle states because of their overwhelming statistical weight. Fluctuations in the energy of the collective modes leave the single particle energy very nearly unchanged. In this way, the single particle degrees of freedom act as a "heat bath" for the other degrees of freedom, and it is quite useful to discuss the temperature of that bath. One is used to talk of the temperature of a system containing moles of particles rather than a few hundred. However, recall the definition of temperature: as the inverse of the change in entropy with internal energy. That is, $\frac{1}{T} = \frac{dS}{dU}$. In order for the temperature to be a meaningful quantity, we must assure ourselves that this derivative is a smooth function. Entropy is defined as the logarithm of the number of states available to the system (La 69 Eq. (7.7)). The density of energy levels as a function of internal energy can be estimated as $W(U) = 0.005 \exp(2\sqrt{10U})$ MeV/level (Bl 52, pp. 371-2; also Er 60). At 60 MeV excitation, this gives a level density of 9.4×10^{18} levels/MeV, or a level spacing of 1.1×10^{-19} MeV/level. Because of the very short life

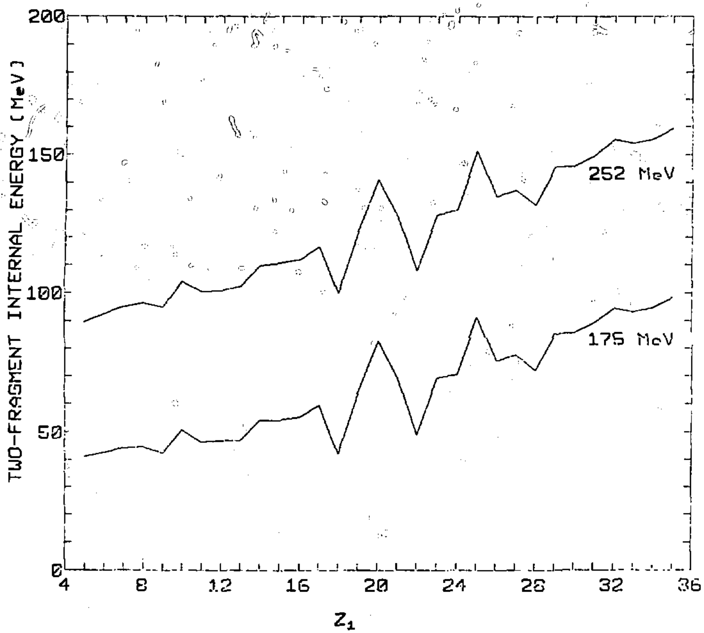

XBL 7712-11203

Fig. 4 Internal energy (defined in Section III.A.1) of the two-nucleus reaction complex versus the atomic number of the lighter fragment.

time of the reaction system ($\sim 10^{-20}$ seconds), the uncertainty in its energy is $\Delta E \cong \hbar/t \cong 6.6$ KeV. This is far greater than the level spacing, so the level density (and entropy) will increase smoothly with internal energy.

In Fig. 5 we show calculations of the temperature versus Z_1 based on the internal energies shown in Fig. 4. The temperature here is calculated as $T = \sqrt{10U/A}$, where A = mass number of the reacting complex = 217 and U = internal energy of the complex. This is entirely equivalent to calculating the temperature of each fragment with the assumption that the internal energy is partitioned between the two fragments proportional to their masses. That is, the temperature of fragment 1 is $T_1 = \sqrt{\dfrac{E_1}{A_1/10}} = \sqrt{\dfrac{\frac{E A_1}{A}}{A_1/10}} = \sqrt{\dfrac{E}{A/10}}$.

A quick look at Fig. 5 shows a typical temperature of 1.8 MeV for the lower bombarding energy, and 2.4 MeV for the higher bombarding energy. These values allow us to estimate the degree to which the ground state occupation density distribution function is perturbed. Recalling that the distribution function of a Fermi gas is described by (La 69, Section 56):

$$n(E) = \frac{1}{e^{(E-\mu)/T} + 1} \quad ,$$

one finds that the energy difference between an occupation number of 0.8 and 0.2 is $2.77T$. This roughly represents the width of the distribution function around the Fermi surface, and should be compared with a chemical potential of about 40 MeV. For the lower bombarding

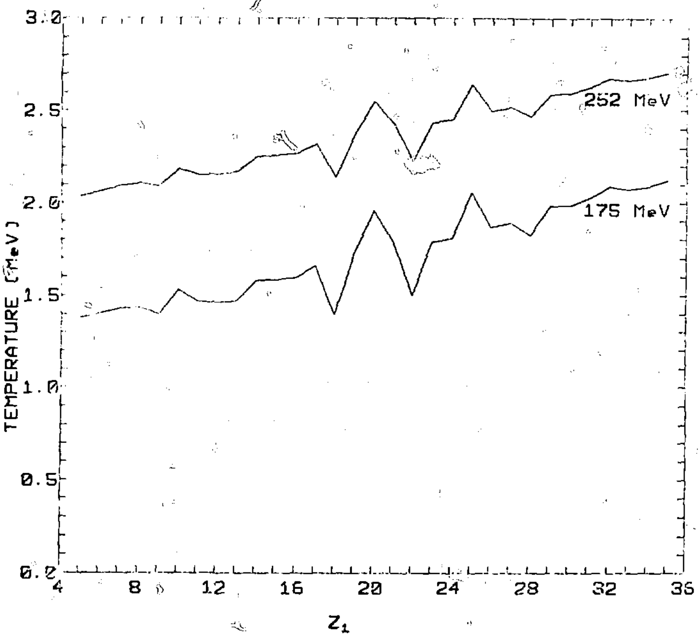

XBL 7712-11204

Fig. 5 Temperature of the two-nucleus reaction complex versus the atomic number of the lighter fragment.

energy this width is 5.0 MeV and for the upper bombarding energy this is 6.6 MeV. One sees that each nucleus is still a strongly degenerate Fermi gas despite the large amount of excitation energy.

2. Qualitative Explanation of the Fragment Kinetic Energies

The most obvious feature of the center-of-mass kinetic energy distributions of the light fragments produced in the reaction of Ne with Au is the simple behavior of the centroids. These are shown in Figs. 6 and 7, averaged over the angles at which the measurements were made. The transformation of the measured laboratory energies to center of mass values requires knowledge of the fragment mass. Since only the atomic number is measured, the mass is determined from the assumption that the neutron-to-proton ratios of the two fragments are those which minimize the energy of the system in this degree of freedom, at fixed neutron-to-proton ratio and fixed total mass. No correction of the fragment energy to account for rotation or particle evaporation has been made but will be considered later. The two smooth curves show the Coulomb repulsive energy for two spherical nuclei, and for two spheroidal nuclei allowed to deform to their equilibrium shapes given the constraint that they be in contact. The lower set of points on each graph shows the full width at half maximum (FWHM) of the kinetic energy spectrum. The error bars represent the standard deviation of the measured value over angle.

The appearance of the data is very similar for both the 175 and 252 MeV projectile energy. The mean energies for products heavier than Ne vary smoothly with atomic number, and fall between the "spheres" and "spheroids" curves. The energies for products of the 175 MeV

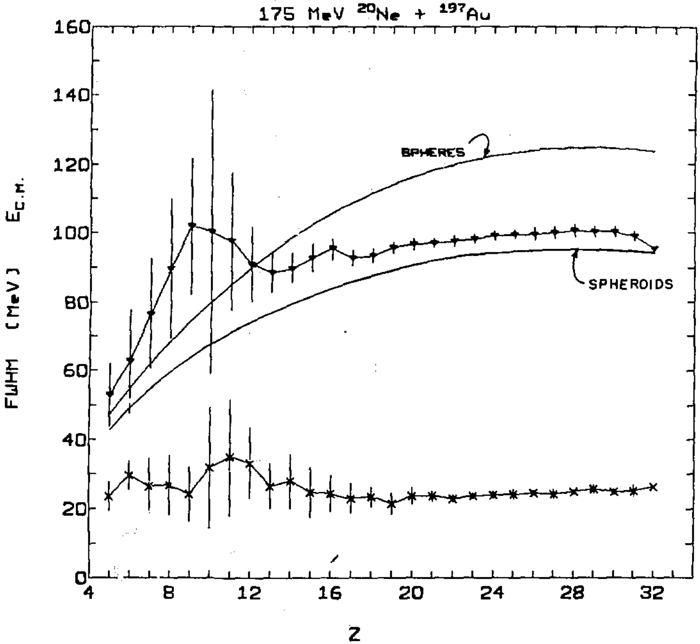

XBL7710-6941

Fig. 6 Experimental center of mass mean kinetic energy (upper points) and FWHM (lower points) of the light fragment, averaged over angle. *Error bars are ± one standard deviation. Smooth curves are Coulomb* energy for touching spheres (upper curve) and spheroids(lower curve) at equilibrium deformation. 175 MeV laboratory projectile energy.

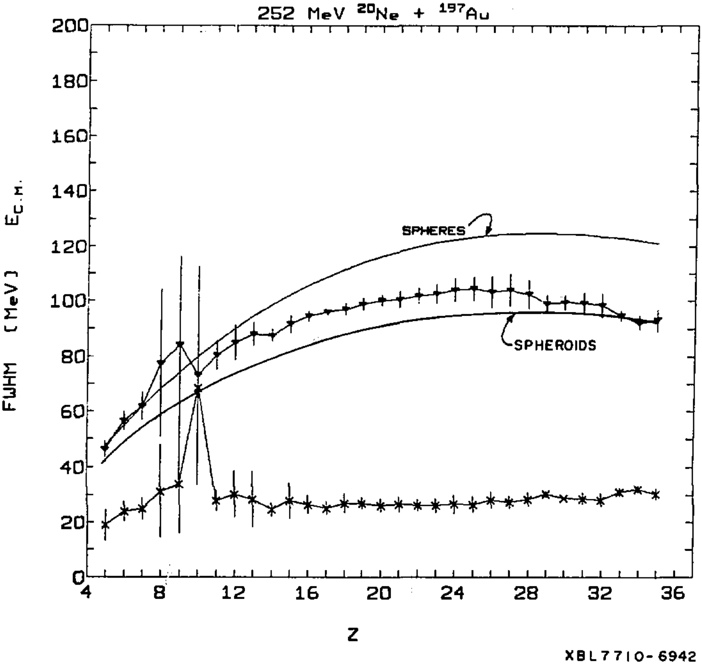

Fig. 7 Same as Fig. 6 for 252 MeV laboratory projectile energy.

reaction similar to or lighter than Ne substantially exceed the "spheres" energy. This arises from the difficulty of completely separating quasi-elastic events, in which a substantial amount of the initial projectile kinetic energy remains as kinetic energy, from much more highly inelastic events. The energies of products below Z = 13 should be viewed as representing an admixture of reactions over a continuum of reaction type -- from elastic to quasi-elastic direct reactions to highly inelastic reactions. This effect is much less pronounced in the 252 MeV case. Here we see appreciable deviation above the "spheres" energy only for atomic numbers 8 and 9. This arises from the fact that the quasi-elastic reactions occur at appreciably higher energy and at more forward angles in this case, allowing for cleaner separation from the deep inelastic component. Experimental kinetic energy spectra are shown in Figs. 8 and 9. The large widths of the spectra for Z's 7 and 12 in the 175 MeV case are explained by the above mentioned mixture of reaction types.

This difference between the light products at the two bombarding energies is not of primary importance to the understanding of highly inelastic reactions -- arising, as it does, from an admixture of other reaction types. More important is the close agreement between the two sets of data for Z's above 12. One notices that the mean center of mass kinetic energies agree to within about 5 MeV, the data at 252 MeV being consistently higher. Since the kinetic energy spectra of these fragments are quite broad (20 to 25 MeV FWHM) this difference is of marginal significance. We see immediately a fundamental characteristic of

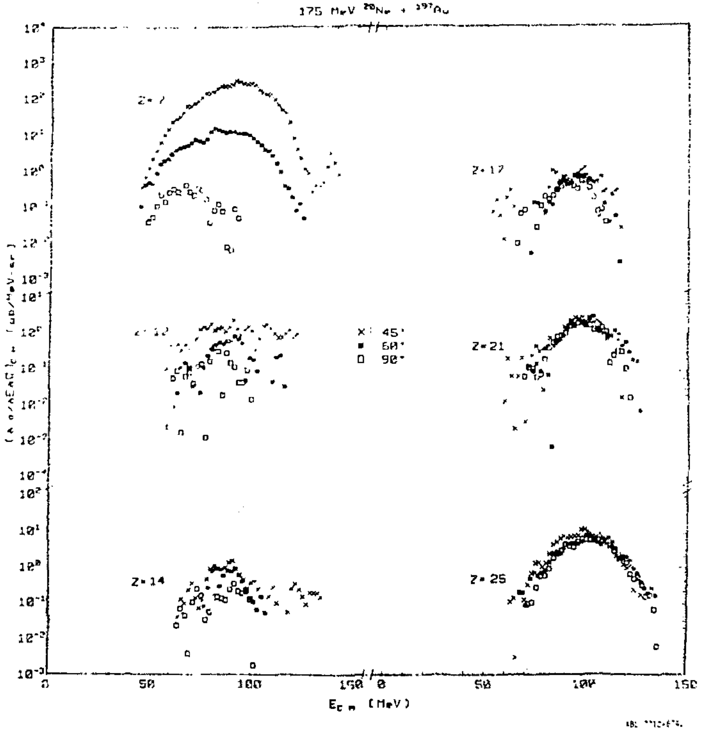

Fig. 8 Center of mass kinetic energy spectra. 175 MeV projectile energy.

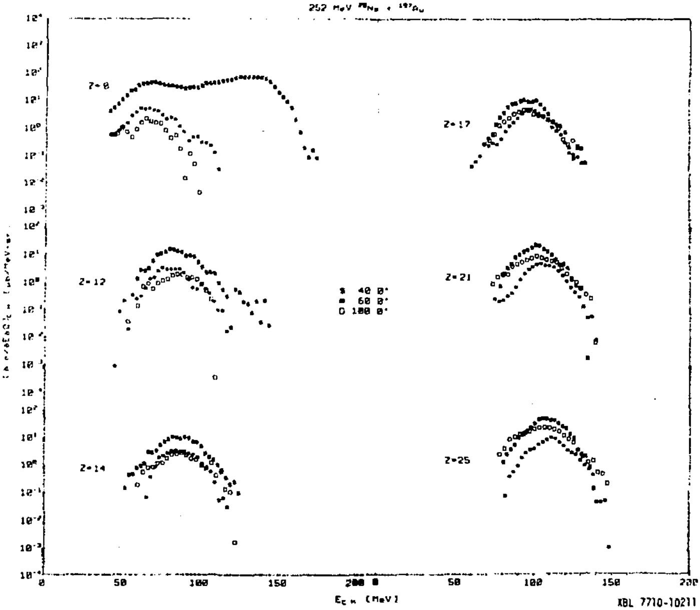

Fig. 9 Center of mass kinetic energy spectra. 252 MeV projectile energy.

fragment energies observed in highly inelastic reactions: the mean center of mass kinetic energies are (very nearly) independent of the initial projectile energy.

A qualitative understanding of this observation is not difficult to obtain. The kinetic energy of the fragments arises from their Coulomb repulsion and centrifugal acceleration as they move apart. The average Coulomb potential energy depends on the degree of stretching of the nuclei but not (directly) on the initial projectile energy. The average rotational energy depends on the mean angular momentum leading to deep inelastic reaction of the two nuclei, and thus increases with the bombarding energy. However, the greater the rotational energy, the greater will be the centrifugal stretching of the nuclei, leading to lowering of the Coulomb energy. We should expect a trade-off between these two components in the kinetic energy. That the final kinetic energies are close, indicates that the rotational-Coulomb trade-off is fairly even. This picture of the origin of the fragment kinetic energy is supported by much work (Ba 75, Ga 75, Mo 75a, We 76, Ca 77, Ru 77, Wo 77). Reproduction of the experimental results with a mathematical model has received less attention (Ni 63, Eg 76).

Another characteristic feature of the kinetic energy spectra of highly inelastic reactions is that their widths are much greater than the temperature. The typical FWHM is 20 to 25 MeV. This can be understood qualitatively on the basis of the well known "amplification model" (Mo 75b). Figure 9a shows a schematic representation of the total potential energy (parabola of curvature a) and final kinetic

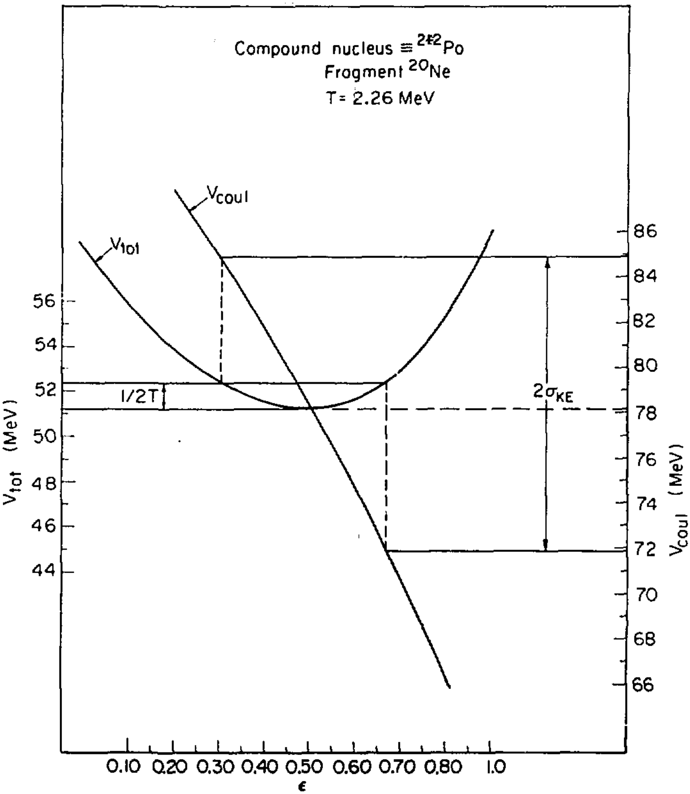

XBL752-2333

Fig. 9a Schematic diagram of the total potential energy (parabola), and the final kinetic energy (nearly straight line). Illustrates the "amplification" effect for origin of large kinetic energy width.

energy (nearly straight line of slope-b), versus the deformation of the touching fragments. The average energy in the deformation mode is ½T, giving rise to the maximal and minimal deformations d_+ and d_-. Specifically,

$$d_{\pm} = \pm \sqrt{\frac{T}{2a}} \quad .$$

This range of deformation results in a range of kinetic energies of the value

$$2\sigma_{KE} = -b(d_- - d_+) = b \sqrt{\frac{2T}{a}} \quad .$$

The "amplification" factor is $b\sqrt{\frac{2}{a}}$. Since the curvature, a, is quite small and the slope, b, considerable, the kinetic energy width exceeds the temperature.

3. Description of the Quantitative Model

An accurate quantitative understanding of the kinetic energy means and widths can be obtained with the use of a simple model, whose success leads to an important insight into the degree of thermal equilibration of the reaction complex. The model must provide a method of calculating the distribution of the Coulomb plus rotational kinetic energy at the time of the breakup.

Calculations with this model are based on the following functions.

$E_C(\rho)$ = Coulomb interaction as a function of shape of the reacting nuclei.

$E_r(\rho,L)$ = total rotational energy as a function of shape and angular momentum.

$E_S(\rho)$ = surface energy as a function of shape.

$E_{sc}(\rho)$ = self Coulomb energy as a function of shape.

$V(\rho,L)$ = total potential energy as a function of shape and angular momentum = $E_c + E_s + E_{sc} + E_r$.

$E_{orb}(\rho,L)$ = orbital rotational energy as a function of shape and angular momentum.

$E_{ke}(\rho,L)$ = total kinetic energy at infinite separation = $E_c(\rho) + E_{orb}(\rho,L)$.

The most important hypothesis of the model is that the energy moments can be calculated by treating the nucleus as a classical canonical ensemble at thermal equilibrium whose temperature is fixed by the internal energy of the single particle degrees of freedom, according to the discussion in section III. A.1. The kinetic energy in the shape oscillation mode before breakup is small (in the mass-range studied here) compared to the final Coulomb + rotational kinetic energy and is ignored. This has been discussed elsewhere (Mo 75b).

The equations described above can be used to calculate the n-th moment of the fragment kinetic energy. At a specified angular momentum, L, the n-th moment of the kinetic energy $E_{ke}(\rho,L)$ is summed over the deformation, ρ, and multiplied by a normalized Boltzmann factor. This expression is then averaged over the angular momentum range, multiplying each L-wave by its geometrical weight -- $\pi \lambda\!\!\!^{-2}(2L+1)$, where $\lambda\!\!\!^{-}$ is the DeBroglie wavelength divided by 2π. The n^{th} moment of the fragment kinetic energy is

$$\langle E_{ke}^{n} \rangle = \frac{\displaystyle\sum_{L_{min}}^{L_{max}} \left[\pi \lambda^2 (2L+1) \, \frac{\sum_{\rho} E_{ke}(\rho,L)^n \exp(-V(\rho,L)/T)}{\sum_{\rho} \exp(-V(\rho,L)/T)} \right]}{\displaystyle\sum_{L_{min}}^{L_{max}} \pi \lambda^2 (2L+1)} \qquad (1)$$

The following additional assumptions complete the hypotheses of the model, and are to be tested by comparison with the observed kinetic energies.

1. Each fragment deforms as an ellipsoid. The deformation axes are colinear, the eccentricities of the two fragments are the same, and the volume of each fragment is independent of its deformation. For a given mass asymmetry, the shape can therefore be parameterized with just one variable. The most important physical restriction imposed by these simplifications is that the nuclei vibrate in phase reaching maximal and minimal stretching simultaneously. The effect of out-of-phase vibration is not included. This has little effect on the evaluation of the mean kinetic energy, because the potential is fairly symmetrical about the equilibrium deformation, so the mean value of the kinetic energy is close to the value at equilibrium deformation. The width of the kinetic energy is also only slightly underestimated by ignoring the out-of-phase normal mode. This is because the greatest range in energy arises from the in-phase mode; inclusion of the smaller out-of-phase contribution in a quadrature sum of widths would increase the width only slightly.

2. The rotational energy is that for rigid sticking ellipsoids. No slipping of the nuclei against one another is included, nor is any hydrodynamical effect on the moment of inertial considered.

3. The cross section for each angular momentum is $P_L = \pi ƛ^2(2L+1)$, between L = 0 and L = L_{max}. ƛ is the reduced wavelength of the projectile. The upper limit on the angular momentum is close to the grazing value. The lower limit is zero because any cross section for compound nucleus formation at low angular momentum is most likely to result in fission and be detected as part of the highly inelastic cross section.

The detailed derivation of the kinetic and potential energy equations is given in Appendix 1.1. The total potential energy, from Eqs. (4), (9), (10) and (13) in that Appendix, is

$$V(\rho,L) = E_r(\rho,L) + E_s(\rho) + E_c(\rho) + E_{sc}(\rho)$$

$$= \frac{E_{ro}}{F(\rho)} + E_{so}G_x(\rho) + E_{co}W(x_1,x_2) + E_{sco}K_x(\rho) \qquad (2)$$

The subscript x in $G_x(\rho)$ and $K_x(\rho)$ is p or o as needed, to indicate prolate or oblate ellipsoid. The variables x_1 and x_2 are functions of the deformation, ρ, and are defined in the Appendix. E_{ro}, E_{so}, E_{co} and E_{sco} are the values of the rotational and surface energies, Coulomb interaction energy and self-Coulomb energy of the two nuclei when they are spherical. Equation (2) shows that the total potential can be factored into a sum of four terms, each of which is the value for touching spheres times a dimensionless function of the shape.

The kinetic energy is, from Eq. (6) and (10) in Appendix I:

$$E_{ke}(\rho,L) = E_{orb}(\rho,L) + E_c(\rho) = \frac{\rho^2}{F(\rho)^2} \; E_{orb,o} + E_{co} W(x_1,x_2) \; , \qquad (3)$$

Figures 10 through 14 show the total potential energy versus ρ for five values of Z_1: 6,12,18,24 and 30. Each figure shows four values of the angular momentum: 0,80,160 and 240 ħ. The grazing angular momentum in the 175 and 252 MeV reactions is about 97 ħ and 137 ħ respectively. The minimum of the potential energy of the touching nuclei shifts to larger deformation, ρ, as the angular momentum, L, increases. One notices in these figures that the curvature and position of the minimum changes markedly with L for the low Z's. For the higher Z's the effect of L on the potential energy is quite reduced. Figure 15 shows the equilibrium deformation as a function of L. Figures 16 through 20 show the total kinetic energy versus ρ for the same values of Z_1 and angular momentum. The kinetic energy increases markedly with L at fixed deformation. However, the kinetic energy at ρ_{min} for the four values of L varies by only 10 MeV or less. This is an important observation, and represents the trade-off between Coulomb and rotational energy, as mentioned earlier in this section.

4. Correction of the Data for Particle Evaporation

We are now able to calculate moments of the kinetic energy distribution, with Eqs. (1), (2) and (3). These equations attempt to describe the kinetic energy of the two fragments before any evaporation of particles from the fragments takes place. However, the kinetic

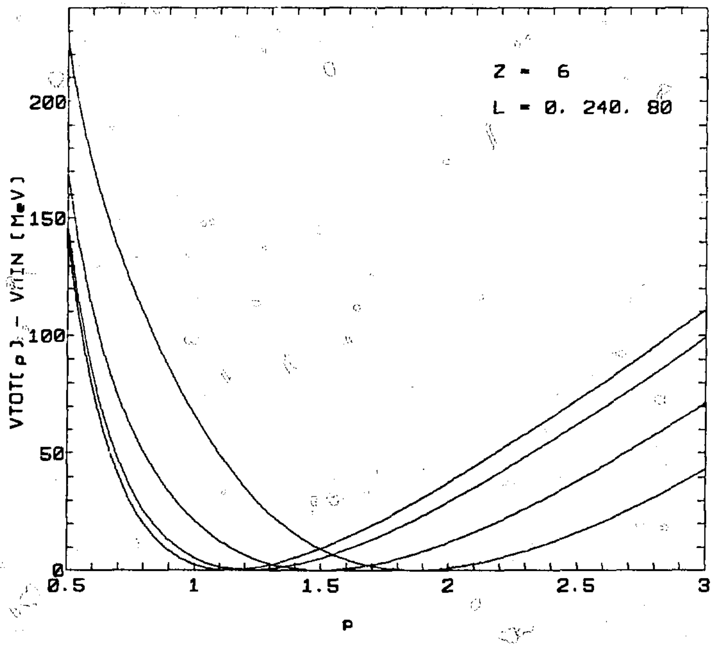

XBL 7711-10803

Fig. 10 Calculated potential energy versus fragment deformation for atomic number 6, at four angular momenta: 0, 80, 160 and 240 ħ.

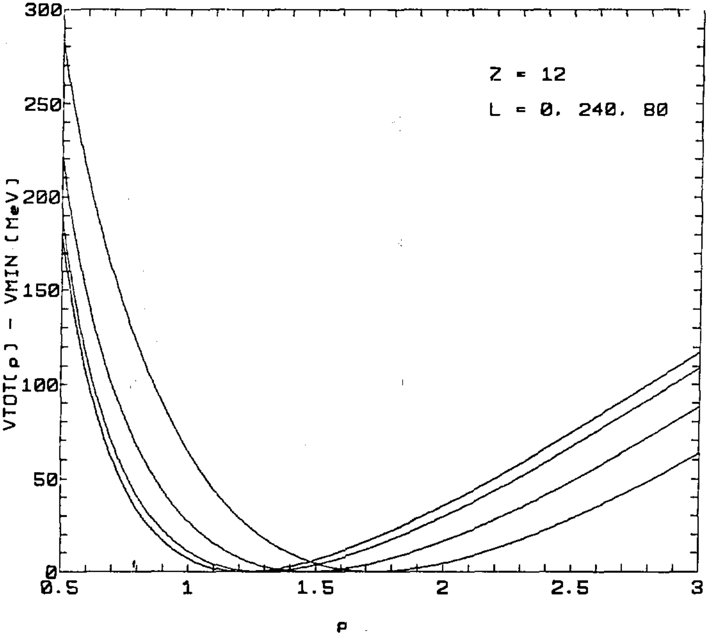

XBL 7711-10811

Fig. 11 Same as Fig. 10 for atomic number 12.

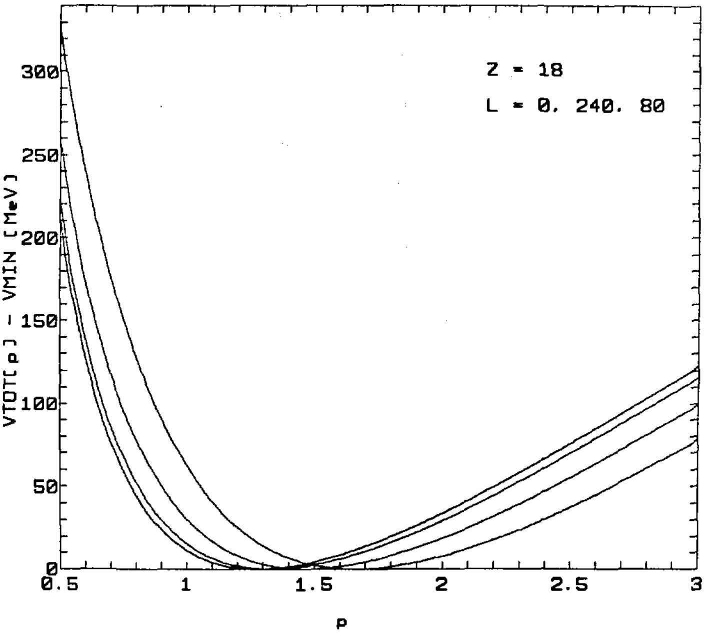

XBL 7711-10809

Fig. 12 Same as Fig. 10 for atomic number 18.

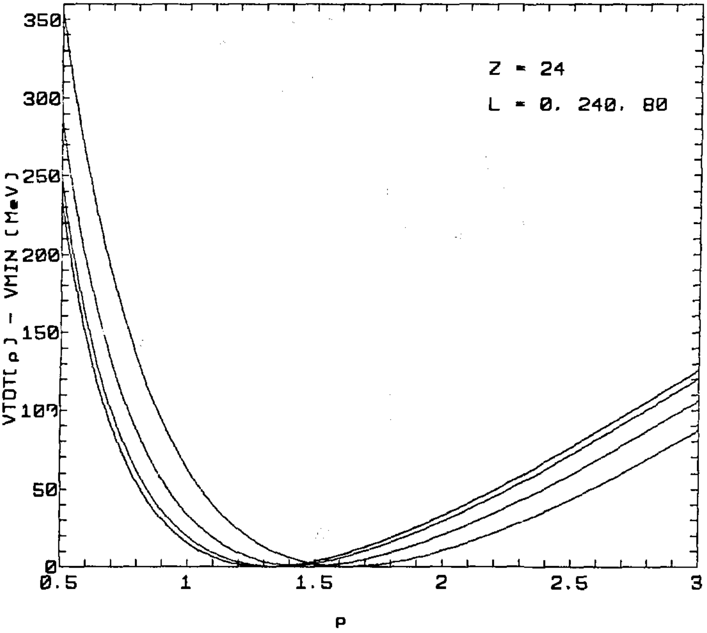

XBL 7711-10808

Fig. 13 Same as Fig. 10 for atomic number 24.

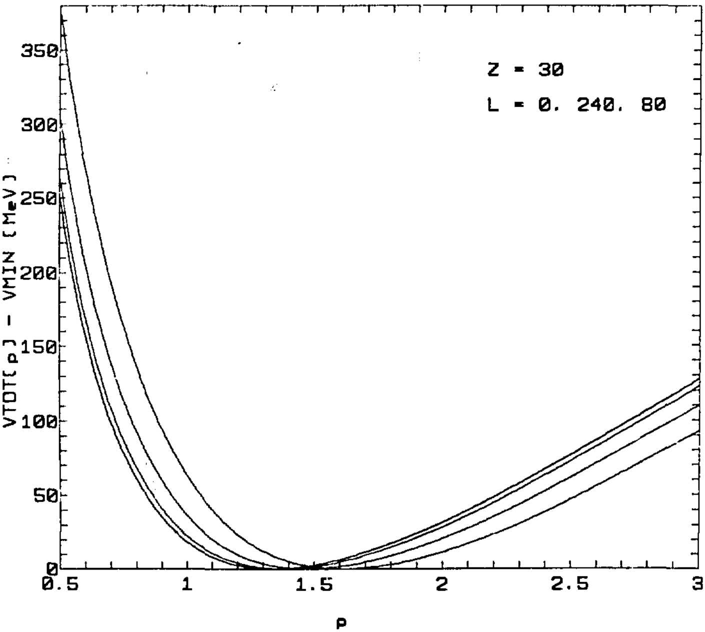

XBL 7711-10810

Fig. 14 Same as Fig. 10 for atomic number 30.

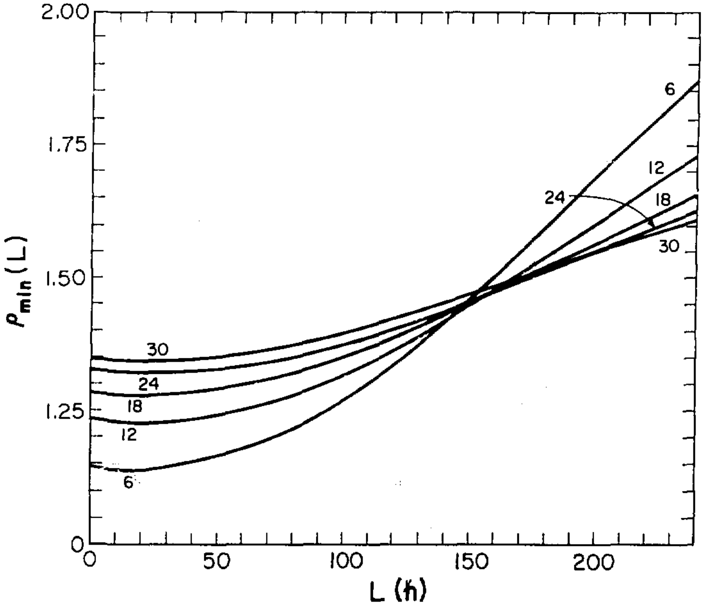

XBL 781-135

Fig. 15 Fragment deformation at minimum potential energy versus angular momentum.

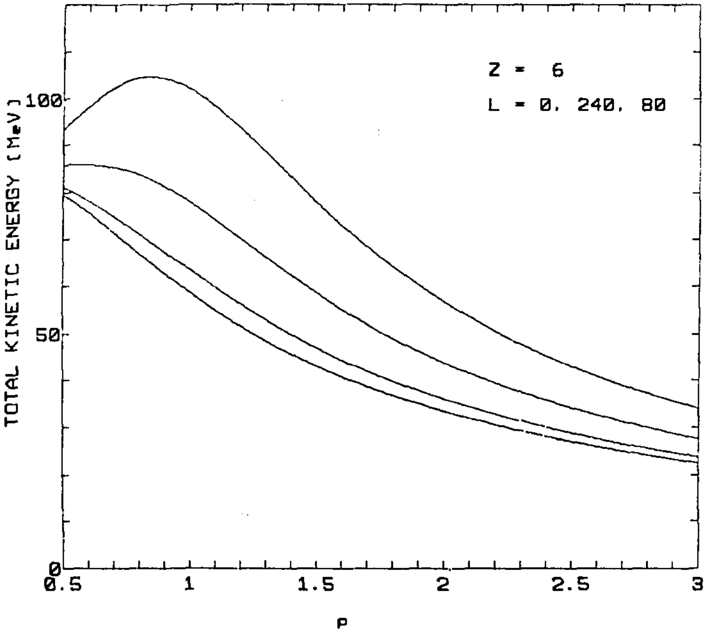

XBL 7711-10804

Fig. 16 Calculated total center of mass kinetic energy versus fragment deformation for atomic number 6, at four angular momenta: 0, 80, 160 and 240ħ. Angular momentum increases from lower to upper curves.

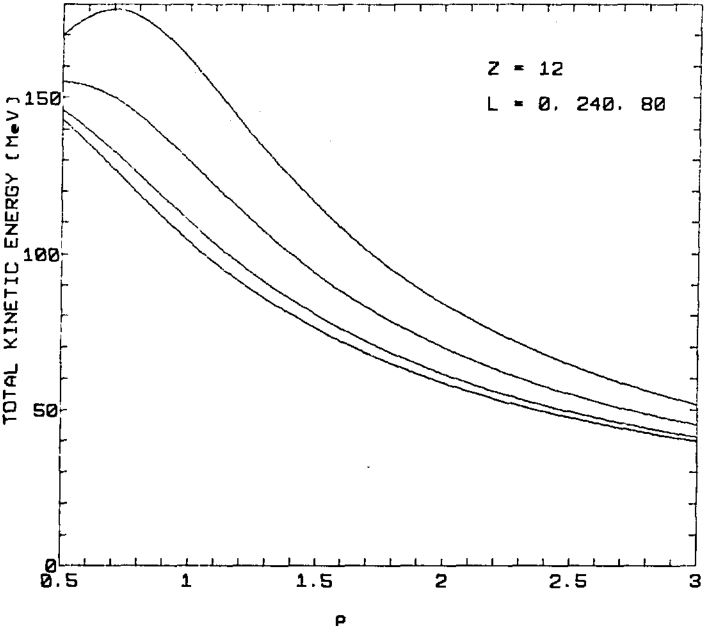

XBL 7711-10805

Fig. 17 Same as Fig. 16 for atomic number 12.

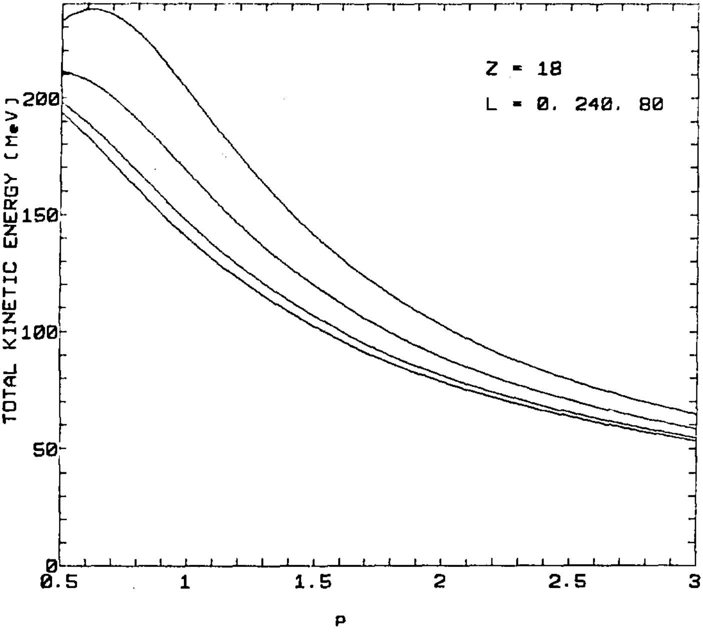

XBL 7711-10806

Fig. 18 Same as Fig. 16 for atomic number 18.

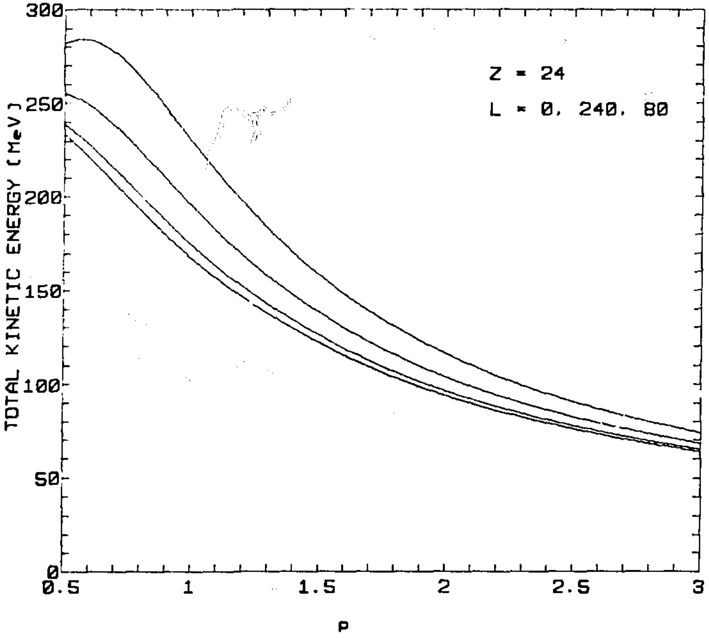

XBL 7711-10807

Fig. 19 Same as Fig. 16 for atomic number 24.

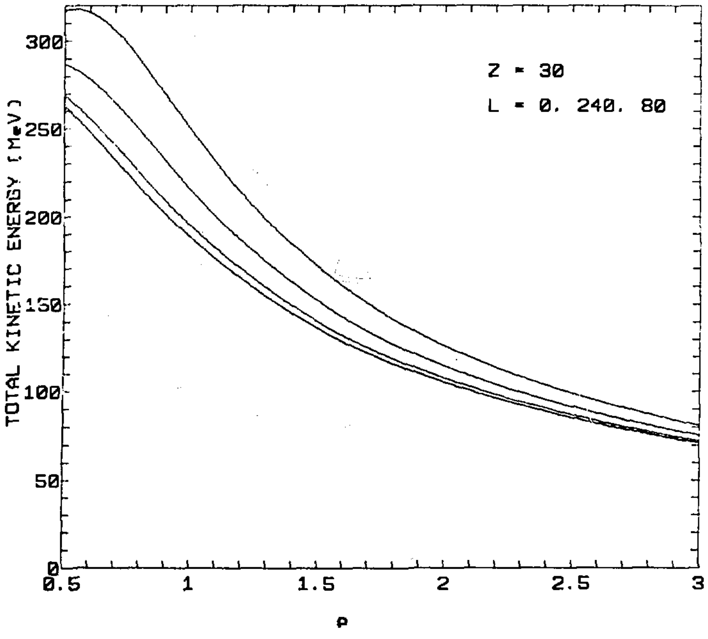

XBL 7711-10812

Fig. 20 Same as Fig. 16 for atomic number 30.

energies measured in the laboratory are post-evaporation values, since the fragment flight time to the detector (several nanoseconds) is far greater than the particle evaporation time (10^{-20} to 10^{-16} seconds). Before comparing the calculated kinetic energy moments with the data, it is necessary to correct those data for the effect of evaporation.

a) Evaporated Particles

It is first necessary to determine what particles are likely to be evaporated. The statistical width for evaporation of light particles of any energy from an excited nucleus is of the form (We 57):

$$\Gamma = \frac{1}{2} \frac{gm}{\pi\hbar^2} \bar{\sigma} T^2 e^{-(E_o + V_c)/T}$$

where g = spin multiplicity. 2 for nucleons, 1 for alpha particles.

$\bar{\sigma}$ = energy-averaged absorption cross section of the light particle, to form the excited compound nucleus.

m = mass of evaporated particle.

T = temperature of the post-evaporation nucleus.

E_o = binding energy of the particle.

V_c = Coulomb energy of the particle, if charged.

We can see that emission of alpha particles is generally quite a bit less probable than emission of neutrons. Table 1 shows the binding energy of alpha particles (B_α) and neutrons (B_n) for a range of nuclei, as well as the Coulomb energy (V_c) of the alpha particle with the daughter nucleus. The ratio of alpha to neutron width is calculated for three temperatures, 1.5, 2.0 and 2.5 MeV.

The calculations of Table 1 show us that emission of alpha particles from nuclei near the line of beta stability is generally less probable than emission of neutrons, except for light nuclei. For instance, the values of Γ_α/Γ_n for elements 18, 24 and 34 are 0.53, 0.18 and 0.12 respectively. However, the evaporative decay chain of an excited nucleus may well pass through nuclei far from the beta stability line. Such nuclei have neutron and alpha binding energies quite different from the beta-stable values. Emission of some alpha particles is to be expected, and may even be less depressed than our simple calculations indicated. As a first order approximation we shall ignore alpha particle emission. Proton emission is to be expected in order to maintain the proper neutron-to-proton ratio, although proton emission will be depressed with respect to neutron emission because of the Coulomb barrier. It will simplify our effort to ignore the greater kinetic energy of protons compared to neutrons, arising from the Coulomb repulsion. Finally, we shall assume that all evaporation occurs after breakup of the reaction complex, since its lifetime is thought to be significantly shorter than the evaporation time. (Reaction times will be discussed in Section III.C.). It must be realized, however, that all the evaporation takes place in a very short time compared to the flight time of the fragment to the detector. This means that all angular deflection of the fragment due to its recoil from the emitted particles can be considered to take place in the target itself.

Table 1

Z	A	B_α (MeV)	B_n (MeV)	V_c (MeV)	Γ_α / Γ_n T=1.5	T=2.0	T=2.5
10	20	4.7	16.9	3.3	776.6	173.3	70.9
18	40	6.8	9.9	5.8	0.34	0.53	0.69
20	40	7.0	15.6	6.5	8.17	5.75	4.65
24	52	9.3	12.0	7.5	0.079	0.18	0.29
30	66	4.5	11.0	9.2	0.34	0.53	0.69
34	78	6.0	10.5	10.1	0.047	0.12	0.21
40	92	3.0	8.6	11.7	0.035	0.097	0.18
50	118	4.1	9.3	14.0	0.0057	0.025	0.060
60	146	1.4	7.6	16.2	0.0026	0.014	0.037
70	172	-1.3	8.1	18.3	0.0053	0.023	0.057
80	200	-0.7	8.0	20.3	0.00087	0.0060	0.019

b) A Typical Calculation of the Particle Evaporation Correction

In Appendix I.2 we develop an expression for the post-emission center of mass energy of the parent fragment as a function of its net recoil angle, θ_e, in its own frame of reference. With this result we will examine the first and second moments of this energy, and see that the only significant correction to the mean fragment kinetic energy arises from the evaporative mass loss and not from recoil from the emitted particles, but that the kinetic energy widths are sensitive to emission recoil. Finally in that Appendix we develop an expression for estimating the kinetic energy width due to particle emission, as measured by a detector of finite size.

From Eq. (20) of Appendix I.2 we know that the first moment of the recoil kinetic energy, averaged over all possible recoil angles, is

$$\langle E_f \rangle = (1 - n)\, E_o + \frac{n}{1-n} E_n \tag{4}$$

where n = evaporated mass fraction.

E_o = pre-emission fragment energy in the center of mass.

E_n = mean energy of the emitted particle in the parent frame.

The standard deviation of the recoil kinetic energy (Eq. (21) of Appendix I.2.) is

$$\sigma_{E_f} = 2\left[\frac{1}{3}\, nE_o\, E_n\right]^{\frac{1}{2}} \tag{5}$$

For a Gaussian distribution, the full width at half maximum height (FWHM) is related to the standard deviation by

$$\mathrm{FWHM} = \sqrt{2\ \ln 2}\ \sigma \cong 2.3548\ \sigma \tag{6}$$

In discussing the widths of kinetic energy distributions, we shall refer to the "FWHM", where this quantity is defined by Eq. (6), even if the distribution is not Gaussian. Thus, the FWHM of the energy distribution is, from Eqs. (5) and (6)

$$\mathrm{FWHM} = 2.719\ \sqrt{nE_oE_n} \tag{7}$$

We will now evaluate Eqs. (4) and (7) for typical values of the variables. The number of nucleons emitted is evaluated as the internal energy, U, divided by the sum of the nucleon binding energy plus the mean nucleon kinetic energy. The binding energy is approximated as 6 MeV, and the mean kinetic energy is twice the mean temperature, T. This mean is taken as half the pre-emission temperature at the average angular momentum. The fraction of mass lost from the ^{20}Ne + ^{197}Au reaction is

$$n = \frac{U}{217(6+2T)}$$

Calculation of the internal energy and temperature were described in Section III.A.1. Calculated values of n for both bombarding energies are presented in Table 2.

The fraction of mass lost through evaporation, n, is typically 0.05, and varies from 0.03 to 0.08. The pre-emission temperature, as we know from Fig. 5, is typically 2 MeV. The average kinetic energy of the emitted neutron is just twice the temperature. In the course of the evaporative decay the temperature is reduced from the pre-emission

Table 2

		175 MeV				252 MeV			
Z	A	n(calc)	FWHM$_1$ (exp)	FWHM (calc) due to evap	FWHM TOT	n(calc)	FWHM$_1$ (exp)	FWHM (calc) due to evap	FWHM TOT
5	12	.026	23	4.45	23.89	.052	19	7.69	18.39
6	15	.027	29	4.89	30.70	.053	23	8.46	22.98
7	17	.027	27	5.31	28.72	.054	24	9.12	24.09
8	20	.028	27	5.64	29.08	.055	31	9.71	32.43
9	22	.026	24	5.67	25.95	.054	33	10.00	35.0
11	27	.029	35	6.48	39.28	.057	28	11.15	29.33
12	29	.029	33	6.64	37.32	.057	30	11.49	31.98
13	32	.029	27	6.88	30.74	.058	28	11.90	29.73
14	34	.033	28	7.79	31.89	.061	25	12.79	25.47
15	37	.033	25	7.97	28.57	.062	28	13.11	33.47
16	39	.033	24	8.22	27.49	.062	26	13.48	27.10
17	41	.036	23	8.82	26.19	.065	25	14.11	25.45
18	44	.026	23	7.06	27.46	.056	27	12.90	29.75
19	46	.037	21	9.29	23.90	.067	27	15.00	28.49
20	49	.048	23	11.57	25.68	.076	26	16.77	25.67
21	51	.041	23	10.38	26.82	.070	26	15.90	26.89
22	54	.030	23	8.26	28.58	.060	26	14.34	28.88
23	56	.041	23	10.62	27.50	.070	26	16.31	27.29
24	59	.042	23	10.89	27.83	.071	26	16.62	27.45
25	61	.052	24	13.14	27.93	.081	26	18.57	25.32
26	63	.044	24	11.61	29.59	.083	28	17.37	30.94
27	66	.045	24	11.92	29.93	.074	27	17.70	29.30
28	68	.042	25	11.42	32.39	.072	28	17.39	31.97
29	71	.049	25	12.91	31.82	.078	30	18.67	34.89
30	73	.049	25	13.02	32.16	.078	29	18.81	35.26
31	76	.051	25	13.47	32.41	.080	29	19.25	33.38
32	78	.054	26	14.10	34.10	.082	28	19.84	30.85
33	80	.053	-	14.03	-	.082	31	19.84	37.73
34	83	.054	-	14.26	-	.083	32	20.05	40.39
35	85	.056	-	14.69	-	.084	30	20.46	36.07

value to nearly zero, giving a decay-chain average temperature of about 1 MeV. Thus the average neutron emission energy is about 2 MeV. The single fragment kinetic energy, E_f, (Figs. 6 and 7) varies with Z from about 50 to 100 MeV, with a typical value of 75 MeV. Using these values, the mean corrected energy is 78.9 MeV. The dominant term obtained from inverting Eq. (4), $\frac{1}{1-n}$ E_f, represents the loss in kinetic energy due just to evaporative mass loss, and in this typical case equals 79.0 MeV. The second term, $\frac{-n}{(1-n)^2} E_n$, arises from the recoil of the parent fragment, and equals only -0.1 MeV. Very little error is made by ignoring the recoil term when correcting the observed mean energies for the effect of evaporation. Even taking account of proton emission -- for which E_n is larger due to the Coulomb repulsion -- has little effect on the correction. From now on, correction of mean kinetic energies will involve just the mass-loss term.

Using the same typical numbers to evaluate the FWHM, we find it equal to 7.6 MeV. Here we are rather sensitive to the values of the recoil energy, E_n, and the evaporated mass fraction, n, which are used. Ignoring the effect of proton emission can be quite significant, because its energy can be several times the thermal (2T) energy of the proton. Ignoring fluctuations in the evaporated mass fraction may also introduce some error to this formula.

Estimation of the FWHM with Eq. (7) is deficient also because it does not consider the finite size of the detector, and the fact that particles originally directed away from the detector may be deflected -- by evaporative recoil -- into the detector. This latter effect is particularly important because it is large deflections which cause large changes of the kinetic energy, and thus contribute significantly to the FWHM. Because recoil of the parent fragment does not significantly alter the mean fragment energy, the effect of detector size on the mean kinetic energy can be ignored.

c) Correction of the FWHM - Finite Detector

The FWHM due to evaporation, as measured by a detector of non-zero area, is developed in Appendix I.3. The final formula, Eq. (22) in the Appendix, can be evaluated numerically, and the results are presented in Table 2. Columns 1 and 2 give the atomic number and mass number. Columns 3 and 7 show the evaporated mass fraction n for the 175 and 252 MeV reactions. Columns 4 and 8 show the experimental FWHM. Columns 5 and 9 show the calculated FWHM due to evaporation. Both the experimental and calculated widths are for a single fragment, while the widths calculated with Eq. (1) are for the total (two-fragment) energy distribution. Because the pre-emission energies of the two fragments are completely correlated, the single-fragment widths, σ_i, and the total width, σ, are related by

$$\sigma_1 + \sigma_2 = \sigma$$

and $$\sigma_2 = \frac{M_1}{M_2}\sigma_1 \tag{8}$$

So $$\sigma = \frac{M_1 + M_2}{M_2}\sigma_1$$

Columns 6 and 10 show the total pre-emission widths for the 175 and 252 MeV reactions. These are calculated as the quadrature difference between the experimental widths and the calculated evaporation widths and multiplied by the appropriate mass fraction. That is

$$\mathrm{FWHM}_{\mathrm{tot}} = \frac{M_1+M_2}{M_2}\left[\mathrm{FWHM}^2(\mathrm{exp}) - \mathrm{FWHM}^2(\mathrm{evap})\right]^{1/2}$$

Two features of the numbers in Table 2 should be noted. First, that the evaporation correction does not make a large change in the width. Second, the corrected total widths are fairly independent of atomic number, and equal for both bombarding energies. The large experimental widths observed at 252 MeV are offset by larger evaporative widths due to the greater temperature.

These corrected widths must be viewed as being rather approximate. The width is quite sensitive to the energy of the emitted particle as well as to the number of evaporations. These calculations take no account of charged particle emission, which is sure to be important in the case of protons, and may be important for alpha particles. Also, fluctuations in the amount of mass emitted is not considered. Finally, it should be noted that the calculation of the kinetic energy width according to Eq. (22) of Appendix I assumes that the irradiated area of the target is infinitesimal. In fact, the "beam spot" on the target is about the size of the detector window.

5. Comparison of Theoretical Calculation and Corrected Data

We are finally ready and able to compare the calculated kinetic energy means and widths (based on Eq. (1)) with the corrected experimental means and widths. The graphical comparison appears in Figs. 21 and 22. The discrete points are the data, and the closely spaced smooth curves are the calculations based on two different values of the upper angular momentum limit: the grazing angular momentum and 30 ħ less. In the 175 MeV case these angular momentum limits are 97 and 67 ħ. In the 252 MeV case the limits are 137 and 107 ħ. The choice of the angular momentum upper limit has little effect on the calculation. This recalls our discussion of the trade-off between rotational and Coulomb energy as the angular momentum increases: the rotational energy rises and the Coulomb energy falls.

We begin by considering the mean kinetic energies. In both the 175 and 252 MeV reactions the agreement between data and calculation is fairly good for elements not too similar to Ne. The agreement with the 175 MeV data is somewhat better than with the 252 MeV data. That the data exceed the calculations may, in part, be due to the fact that the detected atomic number is in fact slightly less than the pre-emission value. This means that the data should be shifted somewhat to the right. One can estimate the branching ratio between emitted protons and neutrons by employing the emission width formula used in Section III. A.4. The fraction of emitted particles which are protons is approximately $\Gamma_p/(\Gamma_p + \Gamma_n)$. The total number of emitted particles is nA, where n is the evaporated mass fraction and A is the atomic number of the parent fragment. So, the shift in atomic number is

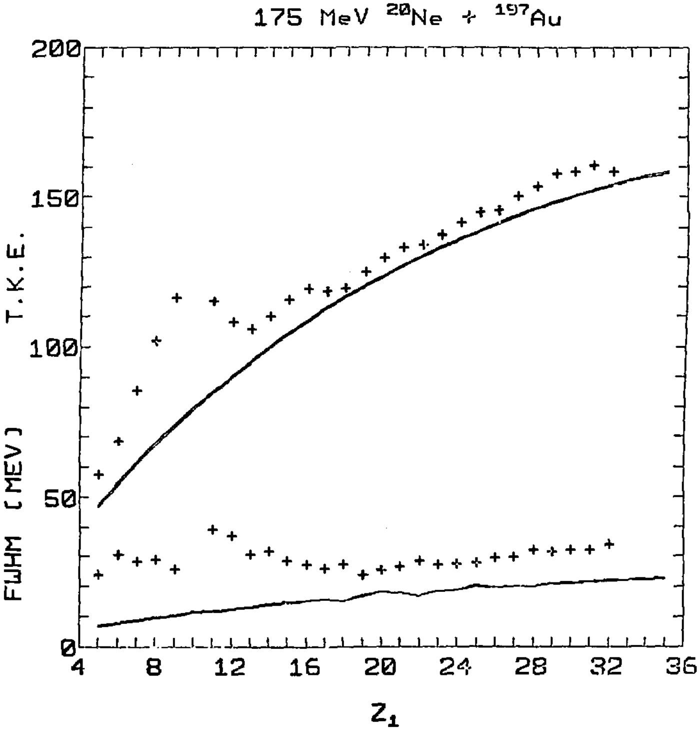

XBL 782-7425

Fig. 21 Experimental two-fragment center of mass kinetic energy (upper points) and FWHM (lower points) versus the light fragment atomic number. Corrected for evaporation. Adjacent smooth curves are calculated values. 175 MeV projectile energy.

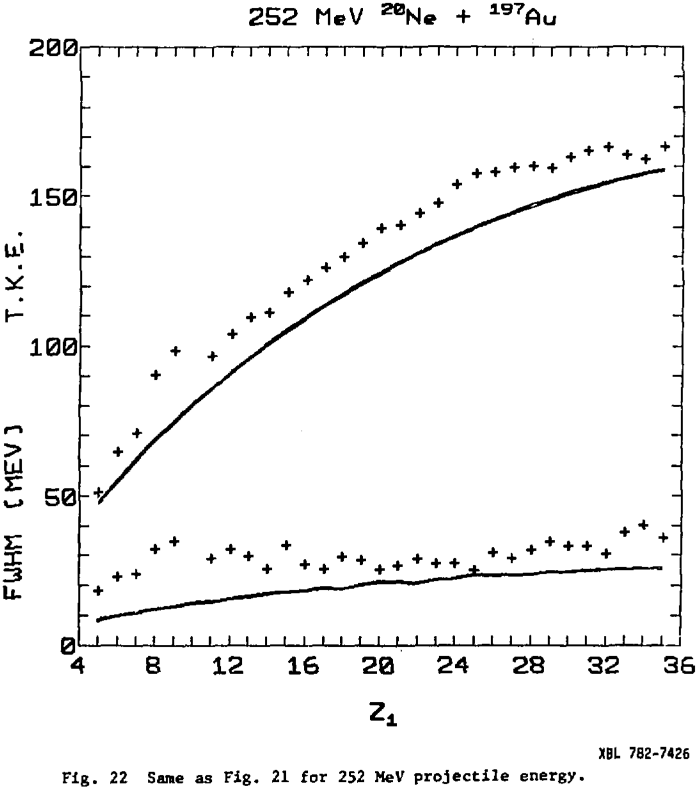

XBL 782-7426

Fig. 22 Same as Fig. 21 for 252 MeV projectile energy.

$$\Delta Z = nA \frac{\Gamma_p}{\Gamma_p + \Gamma_n}$$

Numerical calculations show the shift to be significantly less than one mass unit -- not enough to explain the discrepancy.

The fidelity of the calculation to the data -- over such a large mass range and for two different projectile energies -- is strong support for the hypotheses of the model. The most fundamental and dominant assumption is the treatment of the reaction system as a canonical ensemble at thermal equilibrium. Equation (1) applies only to such a system, and calculation of the temperature (or internal energy) has assumed that all the initial projectile kinetic energy is distributed thermally among the available degrees of freedom.

The major reservation one must have in accepting this conclusion arises from the degree of simplification of the dynamical factors -- limitation to one ellipsoidal shape degree of freedom and consideration of only rigid sticking rotation. Certainly the actual behavior is more complex. Independent shape vibration of the reacting nuclei is to be expected, complicated tri-axial shapes may well appear, and slipping of the nuclei against each other is probably important, at least early in the reaction. Nevertheless, the model need only predict the behavior of the system at the time it breaks up. The picture of the nuclei being in thermal equilibrium when they break up suggests that these complexities are fast transients which largely disappear during the reaction.

We will now direct our attention to the kinetic energy widths. We have already emphasized the severe limitations in evaluation of the pre-emission widths. It is therefore not too surprising when we find the calculations deviating from the data by a healthy margin. What is interesting is that the agreement in the "hotter" system (252 MeV) is not too bad, while the calculations in the "cooler" system fall short of the data by 30 percent or more. The explanation for this may lie in the purely classical nature of the calculation. As the temperature (expressed in energy units) approaches the energy of a single phonon ($h\nu$), the purely classical formula (Eq. (1)) used to evaluate the kinetic energy moments is no longer valid -- the quantized nature of the vibration spectrum has not been accounted for. Quantitative evaluation of the phonon vibration energy requires knowing the inertia of the vibration mode. We can estimate that the phonon energy is on the order of a few MeV. At temperatures from 1.5 to 2.5 MeV, we see that significant quantal effects should be expected.

We can estimate the magnitude of the quantal effect on the kinetic energy widths by employing a simple model. Consider classical vibration in a harmonic potential of the form $V = \frac{1}{2}cx^2$. (Figures 10 to 14 show that this is not too bad an approximation). The average total energy of the oscillator is just the ensemble temperature T. This means that on the average, the system is vibrating between $+\sqrt{\frac{2T}{c}}$ and $-\sqrt{\frac{2T}{c}}$. We can approximate the total fragment kinetic energy (after breakup) as having a linear dependence on the vibration degree of freedom (see Figs. 16 to 20). That is, $E = -ax + b$. Then the kinetic energy width generated by the system vibrating between its extremes is

$$\Delta E_{c\ell} = E(-\sqrt{\frac{2T}{c}}) - E\ (+\ \sqrt{\frac{2T}{c}}) = 2a\ \sqrt{\frac{2T}{c}} = 2a\ \sqrt{\frac{2u}{c}} \tag{9}$$

where u represents the average energy of the oscillator.

However, the correct quantum mechanical expression for the average total energy of a harmonic oscillator is (So 56, p. 239):

$$u = \frac{1}{2}\ h\nu + \frac{h\nu}{e^{h\nu/T}-1} \tag{10}$$

where hν = phonon energy. This reduces to the classical result when the temperature far exceeds the phonon energy.

Nix (Ni 69) has calculated the phonon energy for low-order Legendre polynomial vibrations as a function of the fissility parameter. A fissility parameter of 0.55 is found for the heavy partner of element 25. At this fissility parameter, the phonon energy of the lowest two symmetrical modes (n = 2 and n = 4) range from 2 to 4 MeV. We will consider a phonon energy of 3 MeV. Typical temperatures for the 175 and 252 MeV reactions are 1.75 and 2.25 MeV, respectively. Using Eq. (10) to find the average quantum oscillator energy in these two reactions, and substituting these values for the mean energy, u, into Eq. (9), we obtain a quantum mechanical approximation to the kinetic energy widths. The ratio of the quantum to classical widths in this example are

$$\frac{\Delta E_{QM}}{\Delta E_{c\ell}} = \begin{cases} 1.11, & T = 1.75\ \text{MeV} \\ 1.07, & T = 2.25\ \text{MeV} \end{cases}$$

These results suggest that a proper treatment of the kinetic energy widths requires that attention be given to the quantum nature of the vibration. However, we have presented no evidence concerning the magnitude of the vibration phonon. Until it is obtained, the quantum contribution to the kinetic energy widths must remain unclear. It is important to realize, however, that a large quantal effect on the mean kinetic energies is not to be expected. Because the potential energy is fairly symmetric about its minimum, the average kinetic energy is determined primarily by the equilibrium deformation. Our earlier conclusions concerning energy thermalization before breakup remain intact.

B. Charge Distributions

1. General Considerations

In the past few years, very successful applications have been made of the master equation in theoretical treatments of the elemental or mass distributions arising in highly inelastic reactions. The central feature of these applications is the diffusion of the reaction complex along the mass asymmetry degree of freedom (Mo 75). The exchange of nucleons is recognized as a stochastic transport phenomenon, well known in statistical mechanics (No 74).

It is convenient to label the mass asymmetry of the reaction complex by the atomic number (Z) of one of the two contacting nuclei. The time evolution of the mass asymmetry population, C(Z,t), can be expressed by the master equation as:

$$\dot{C}(Z,t) = \sum_{Z'} (p_{Z'Z}C(Z',t) - p_{ZZ'}C(Z,t)) \qquad (4)$$

where $\dot{C}$ is the time derivative of the population, and $p_{ZZ'}$ is the macroscopic transition probability from configuration Z to Z'.

Nörenberg (No 75) has identified three physical conditions which must be satisfied in order for the master equation to be applied:

(i) The relative kinetic energy and/or the projectile and target masses must be sufficiently large, so that the wave length of relative motion is small compared with the size of the interaction region.

(ii) The identity of the two reacting nuclei must be maintained during the reaction in order for the mass asymmetry to be a relevant degree of freedom.

(iii) Many degrees of freedom must be involved in the reaction, to insure that the nucleon transfer process is a stochastic one. Excitations of specific collective modes must decay into equilibrium with the other degrees of freedom on a time scale which is small compared to the reaction time.

The applicability of the master equation is discussed in some detail by Moretto (Mo 76c) and Nörenberg (No 76). One needs now to evaluate the transition probabilities $p_{ZZ'}$ and to identify the range of summation in Eq. (1).

The macroscopic transition probabilities can be written as (see Re 65, section 15.2):

$$P_{ZZ'} = \lambda_{ZZ'}\rho_{Z'}$$

$$P_{Z'Z} = \lambda_{Z'Z}\rho_{Z}$$

$$\lambda_{ZZ'} = \lambda_{Z'Z}$$

where $\lambda_{ZZ'}$ is the microscopic transition probability (which is symmetric because of microscopic reversibility); ρ_Z and $\rho_{Z'}$ are the statistical weights of the macroscopic configurations Z and Z'. The statistical weight can be identified with the level density of the reaction complex:

$$\rho_Z = \rho(E - V(Z))$$

where E is the total energy and V(Z) is the potential (including rotational) energy. When V(Z) is small the level density can be expanded (Mo 75):

$$\rho(E-V(Z)) = \rho(E)\ e^{-V(Z)/T}$$

where

$$\frac{1}{T} = \left(\frac{\partial \ln \rho}{\partial E}\right)_E$$

which is the inverse of the temperature.

The microscopic transition probability has been usefully expressed as (Mo 75):

$$\lambda_{ZZ'} = \frac{kf}{\sqrt{\rho_Z \rho_{Z'}}}$$

where k is a term having the units of flux, and f is a form factor equal to the contact area between the reacting model:

$$f = 2\pi \frac{R_1 R_2}{R_1 + R_2}\ d, \quad d = 1\ \text{fm}$$

where R_1 and R_2 are the radii of the nuclei. The macroscopic transition probabilities can now be rewritten as:

$$p_{ZZ'} = kf \exp\left(\frac{V(Z) - V(Z')}{2T}\right) \tag{2}$$

The sum in Eq. (1) can be restricted to $Z' = Z \pm 1$, in the context of the independent particle model. The master equation can be written as:

$$\dot{C}(Z,t) = \sum_{Z'=Z\pm 1} kf \exp\left(\frac{V(Z')+V(Z)}{2T}\right) \Big[C(Z',t)\exp(-V(Z)/T) - C(Z,t)\exp(-V(Z')/T)\Big] \tag{3}$$

This equation has been successfully used in the analysis of several heavy ion reactions (Mo 76b, Wo 77, Ca 78).

2. The Z Distribution in the Ne + Au Reaction

We have mentioned earlier that highly inelastic reactions involve transfer of a large fraction of the projectile kinetic energy to internal degrees of freedom of the system, and may also be accompanied by exchange of many nucleons between the reacting nuclei.

Our analysis in Section III.A. led us to conclude that the kinetic energy of deep inelastic Ne + Au reactions proceeds to equilibration during the lifetime of reactions for which the light-product atomic number is greater than 12. (The admixture of a continuum of reaction types from elastic to deep inelastic prevented analysis of lighter products). We shall now investigate the extent to which the distribution of reaction product atomic numbers can be characterized by just the temperature of the system and its total mass -- independent of the initial mass asymmetry.

The laboratory differential cross section as a function of atomic number, Z, for the 175 and 252 MeV reactions, is shown in Figs. 23 and 24. Data for 8 different laboratory angles are shown. Figures 25 and 26 show the center of mass differential cross sections. The differential cross sections ($d\sigma/d\Omega$) for elements above atomic number 14 have been fitted with 2nd order polynomials and integrated from 0 to 360 degrees. The results are shown in Fig. 27. The large yield in Figs. 25 and 26 of products similar to Ne reflects, in part, a contribtuion of quasi-elastic reactions. However, this cannot explain the increase in yield

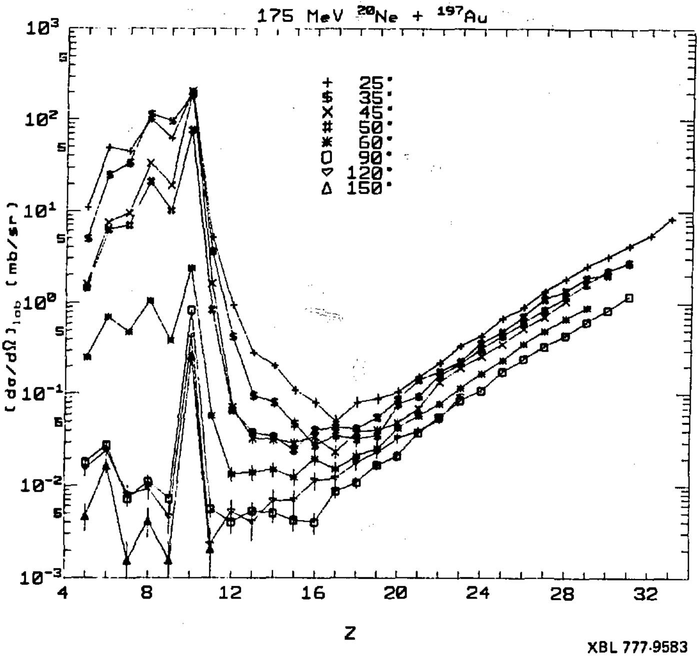

XBL 777-9583

Fig. 23 Experimental laboratory cross sections versus the atomic number of the light fragment. Eight laboratory angles. Error bars indicate ± one standard deviation. 175 MeV projectile energy.

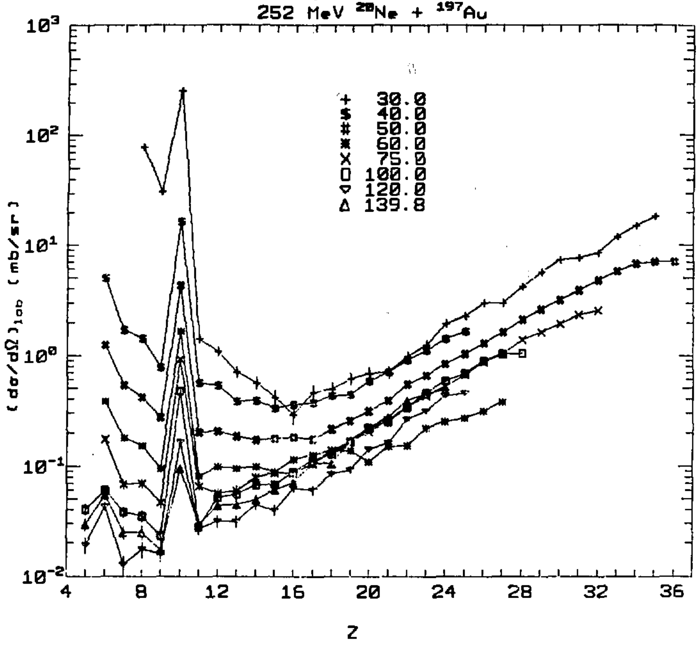

XBL 778 2919

Fig. 24 Same as Fig. 23 for 252 MeV projectile energy.

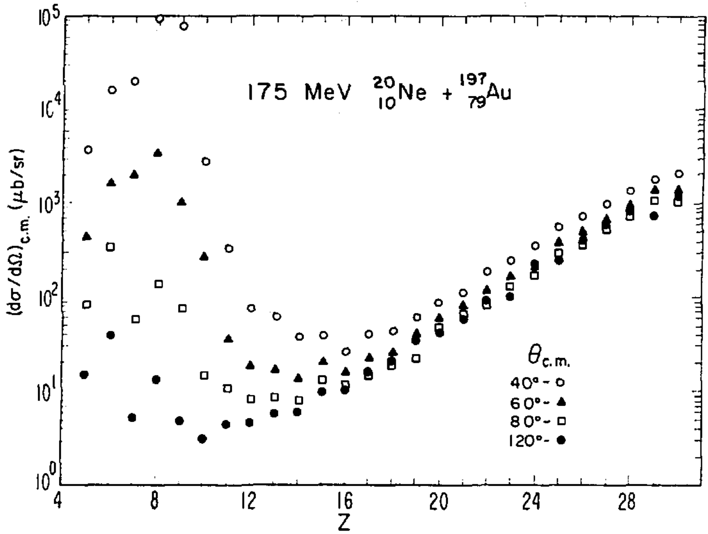

XBL 7710-2393

Fig. 25 Experimental center of mass cross sections versus the atomic number of the light fragment. Data collected at four laboratory angles. 175 MeV projectile energy.

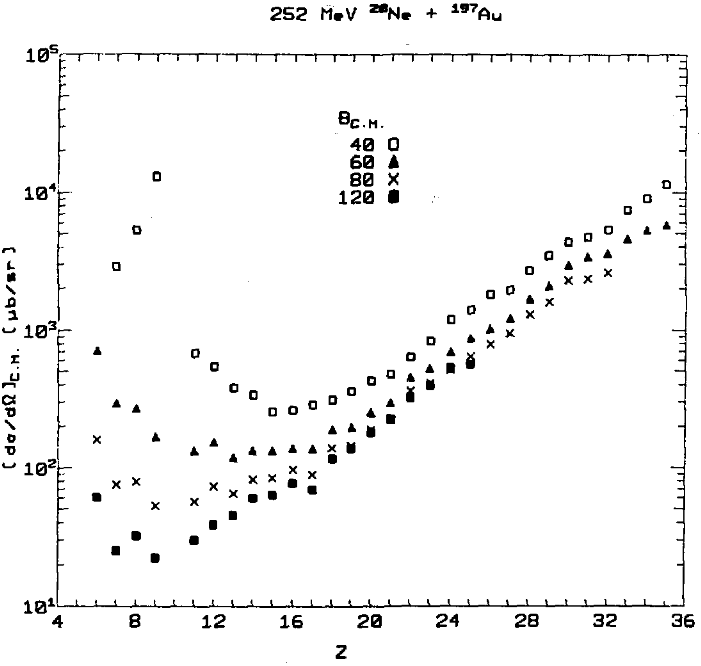

XBL 7710-10310

Fig. 26 Same as Fig. 25 for 252 MeV projectile energy.

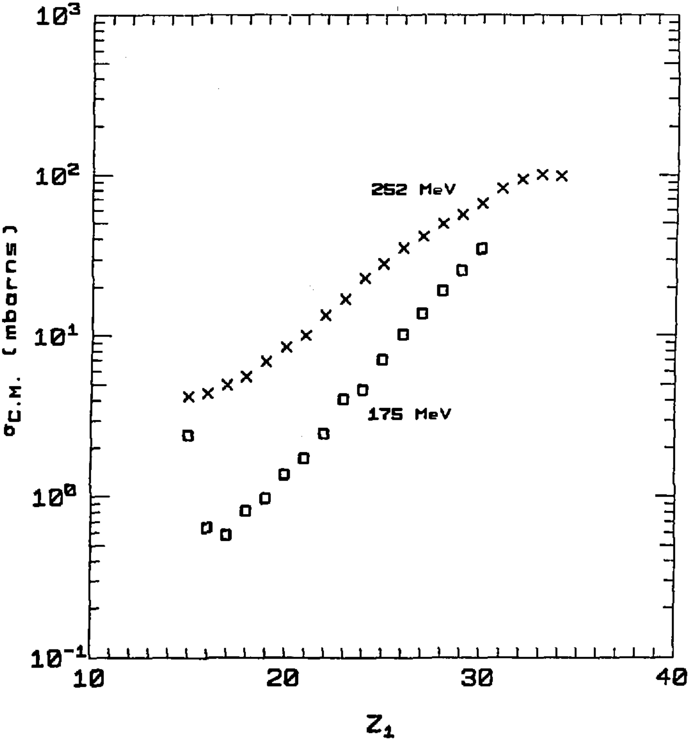

XBL 782-7035

Fig. 27 Angle-integrated cross sections for elements above atomic number 14. Integrated over full angular range.

from atomic numbers 16 to 13 at forward and intermediate angles, because the kinetic energies of these products are thermalized. The explanation lies in examination of the degree to which the Z distribution has reached equilibration, as has been observed in other highly inelastic reactions (Ba 75, Ga 75, Mo 75c, Mo 76, Ru 77).

3. Testing the Equilibration

We shall now develop a theoretical expression for the equilibrium atomic number distribution, and compare it with the observed distributions. For the potential energy as a function of atomic number, V(Z), we will use the liquid drop formula developed in Section III.A.2, evaluated at the equilibrium deformation of the two touching nuclei. The temperature, T(Z), is also evaluated at the equilibrium deformation. Figure 28 shows the potential energy versus Z for a range of angular momenta. In our discussion we will consider only the average angular momentum for each reaction energy: 67ħ for 175 MeV and 97ħ for 252 MeV. The normalized equilibrium distribution is:

$$W(Z) = \frac{e^{-V(Z)/T(Z)}}{\sum_{Z} e^{-V(Z)/T(Z)}} \qquad (4)$$

We begin our analysis by comparing the observed relative population of different mass asymmetries (atomic numbers) with the theoretical equilibrium values. The following quantity is to be considered:

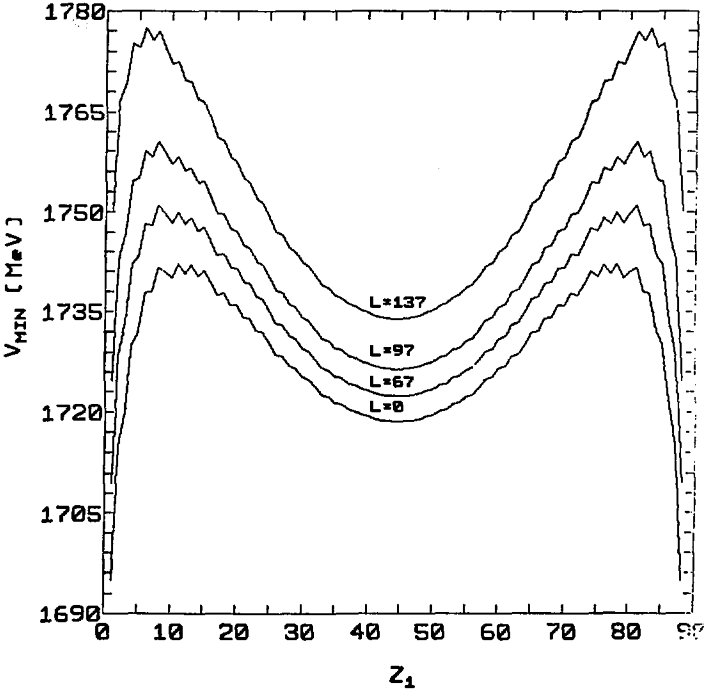

XBL 782-7424

Fig. 28 Minimum potential energy along deformation coordinate for touching nuclei, versus atomic number of the light fragment.

$$R(Z) = \frac{W(Z)/W(30)}{\sigma(Z)/\sigma(30)} \tag{5}$$

where $W(Z)$ is evaluated from Eq. (4), and $\sigma(Z)$ is based on the data of Fig. 27. The ratio $W(Z)/W(30)$ represents the shape of the distribution at equilibrium, if we neglect the possibility of fission of the heavy partners of the lightest elements. However, fission of these heavy elements would not greatly alter the shape of the Z distribution, if it is fully equilibrated, because their masses are nearly equal to the total mass of the Ne + Au system.

If the experimental distribution is equilibrated, the ratio $R(Z)$ will equal unity for all elements. The values of $R(Z)$ for both projectile energies are shown in Fig. 29. We see that $R(Z)$ is less than unity for atomic numbers less than 30 and (for the 252 MeV reaction) greater than unity for atomic numbers above 30. This means that the experimental distribution is less steep than the theoretical equilibrium distribution at both reaction energies. In other words, the experimental distributions are weighted towards the initial mass asymmetry more than are the equilibrium distributions. Nucleon exchange does not proceed long enough for the reaction system to fully sample all mass asymmetries and to populate them according to their statistical weights.

It is very interesting to note, however, that the function $R(Z)$ at the two different reaction energies agrees closely. This certainly does not represent a close similarity between the experimental distributions, which we see from Fig. 27 are quite different in slope.

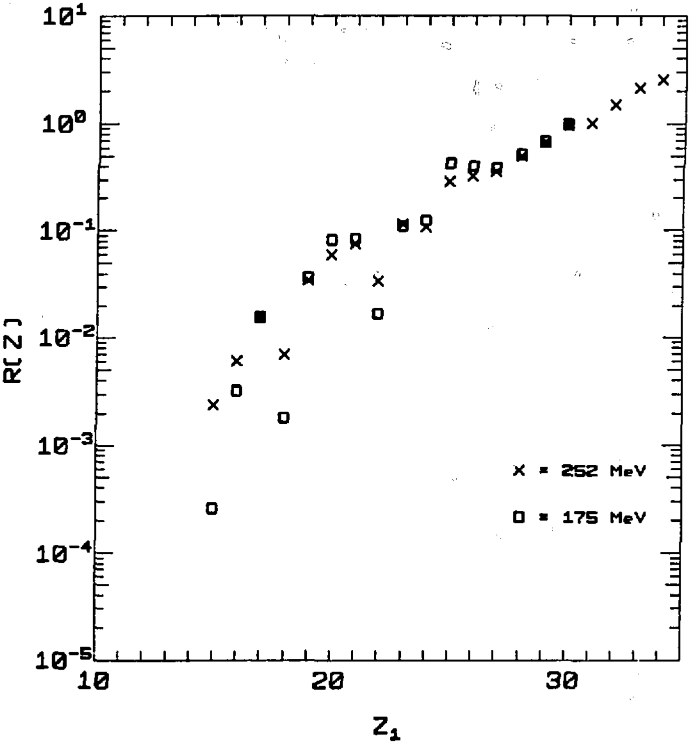

XBL 783-7429

Fig. 29 R(Z) versus the atomic number of the light fragment. See text.

Rather, we see here that the degree to which the system has approached an equilibrium Z distribution is very similar for the two reaction energies.

4. Non-Equilibrium Model

We shall now attempt to provide a somewhat fundamental context in which to understand the degree of equilibration of the Z distribution. Consider an ensemble of Ne + Au nuclei, all of which started reacting at the same instant. We shall define the following quantities for this ensemble: $C(Z,t)$ = the number of reacting pairs for which the light-fragment atomic number is Z, at time t.

$p_+(Z)$ = the probability per unit time Δt of transfer of one proton to the light fragment (of atomic number Z), to increase the asymmetry index from Z to Z+1.

$p_-(Z+1)$ = the probability per unit time Δt of transfer of one proton from the light fragment (of atomic number Z+1) to decrease the asymmetry index from Z+1 to Z.

The unit of time, Δt, is defined in such a way that the transfer probabilities $p_+(Z)$ and $p_-(Z+1)$ are normalized to unity:

$$p_+(Z) + p_-(Z+1) = 1 \tag{6}$$

For any specified values of Z and Z+1, the unit of time Δt is a well defined ensemble average. The absolute rate of transfer of one proton to the light fragment of atomic number Z is, from Eq. (2):

$$p_{Z,Z+1} = kf\,e^{x}$$

where $x \equiv \frac{V(Z)-V(Z+1)}{2T} \cong \frac{-1}{2T}\frac{\partial V}{\partial Z}$. The absolute rate of transfer of one proton from the light fragment of atomic number Z+1 is likewise:

$$p_{Z+1,Z} = kf\ e^{-x}.$$

The ensemble-averaged time Δt *and the relative transfer probabilities* $p_+(Z)$ and $p_-(Z+1)$ are:

$$\Delta t = \frac{1}{p_{Z,Z+1} + p_{Z+1,Z}} ,$$

$$p_+(Z) = \frac{p_{Z,Z+1}}{p_{Z,Z+1} + p_{Z+1,Z}} ,$$

$$p_-(Z+1) = \frac{p_{Z+1,Z}}{p_{Z,Z+1} + p_{Z+1,Z}} .$$

One can readily see the relation between the time interval Δt and the coefficient, kf, which contains the absolute rate information. From the definition of Δt:

$$\Delta t = \frac{1}{kf}\frac{1}{e^{x} + e^{-x}} = \frac{1}{2kf}\,\mathrm{sech}(x) = \frac{1}{2kf}\left(1 - \frac{x^2}{2} + - \ldots\right).$$

Noting that $x \cong \frac{-1}{2T}\frac{\partial V}{\partial Z}$ which is usually small (Mo 76c), we see that

$$\Delta t \cong \frac{1}{2kf} .$$

It is evident that Δt is a precisely defined and physically meaningful quantity. We encounter an approximation, however, when we assume that a single value of the time interval, Δt, normalizes the transfer probabilities for all values of Z. In so doing, we ignore the variation, with mass asymmetry, of the absolute transfer rate. This variation arises predominantly from the variation in the size of the window opening between the nuclei. The temperature variation with Z might also be expected to cause some variation in the transfer rate.

We shall now develop expressions for the normalized transfer probabilities. The net flux between two successive elements of atomic number Z and Z+1 is

$$J_{Z,Z+1} = C(Z,t)p_+(Z) - C(Z+1,t)p_-(Z+1) \quad . \tag{7}$$

When the Z distribution has equilibrated, this flux must vanish. This condition of equilibrium can be expressed by the relation:

$$\frac{C(Z,t=\infty)}{C(Z+1,t=\infty)} = \frac{p_-(Z+1)}{p_+(Z)} \quad . \tag{8}$$

From Eq. (4) we know that the equilibrium distribution is of the form $C_Z = A\exp(-V(Z)/T(Z))$. Combining this result with the normalization condition, Eq. (6), one obtains the following functional forms for the normalized transfer probabilities at equilibrium:

$$p_+(Z) = \frac{e^{-V(Z+1)/T(Z+1)}}{e^{-V(Z+1)/T(Z+1)} + e^{-V(Z)/T(Z)}} \tag{9}$$

$$p_-(Z+1) = \frac{e^{-V(Z)/T(Z)}}{e^{-V(Z+1)/T(Z+1)} + e^{-V(Z)/T(Z)}} \tag{10}$$

By assuming that the time development towards equilibrium of the Z distribution is governed by the phase space available to each asymmetry, the transfer probabilities determined at equilibrium can be applied throughout the time development. This assumption is in fact Nörenberg's third condition for the applicability of the master equation, as described in Section III.B.1.

It should be noted that the physical basis of these equations is the same as that for the expression derived by Moretto (Mo 76c) and presented as Eq. (2) above. Equations (9) and (10), however, contain no information about the absolute rate. One can readily see that Eqs. (9) and (10) are of the same form as Eq. (2), to within a multi-multiplicative factor containing the absolute rate information. We ignore the Z dependence of the temperature, and define:

$$x = \frac{V(Z) - V(Z+1)}{T} \doteq -\frac{1}{T}\left(\frac{\partial V}{\partial Z}\right)_c$$

which is commonly a small number (Mo 76c). Then $p_+(Z)$ can be written as:

$$p_+(Z) = \frac{e^x}{e^x+1} \doteq \frac{e^x}{1+(1+x+\ldots)} = \frac{1}{2}\,\frac{e^x}{1+\frac{1}{2}x+\ldots} \doteq \frac{1}{2}\,e^{\frac{1}{2}x}$$

$$\doteq \frac{1}{2}\,e^{\frac{V(Z)-V(Z+1)}{2T}}$$

which is proportional to the expression in Eq. (2).

The Z-dependent potential and temperature which we used earlier have each been fitted with a second order polynomial in the Z range from 10 to 79, and the resulting equations were used to evaluate p_+ and p_- for the 175 and 252 MeV reactions. The resulting transfer probabilities are shown in Fig. 30. If the potential energy divided by the temperature, as a function of atomic number, were perfectly flat, p_+ and p_- would each equal $\frac{1}{2}$. Where V/T has a negative slope (as in the Z range from 10 to 45) the Z distribution will drift "downhill" towards larger atomic numbers, so p_+ will exceed p_-.

We are now in a position to calculate the time development, in units of Δt, of the 175 and 252 MeV Z distributions. We employ the following form of the master equation for the change in C(Z,t) during one transfer time Δt:

$$\frac{\Delta C(Z,t)}{\Delta t} = J_{Z-1,Z} - J_{Z,Z+1}$$

$$= C(Z+1,t)p_-(Z+1) + C(Z-1,t)p_+(Z-1) - C(Z,t)(p_+(Z) + p_-(Z)) \qquad (11)$$

We have developed values for the transfer probability in the Z range from 10 to 79. We shall simplify this calculation by permanently removing all reaction pairs from the ensemble of reacting nuclei, which diffuse outside this range. This corresponds to those pairs "dropping" into the very steep potential well at the extremes of the Z range.

The ensemble is started at t=0 with 1000 Ne + Au pairs. Figures 31 and 32 show the Z distributions at six different times, for the 175 and 252 MeV cases. The times in units of Δt are 10, 20, 40, 80,

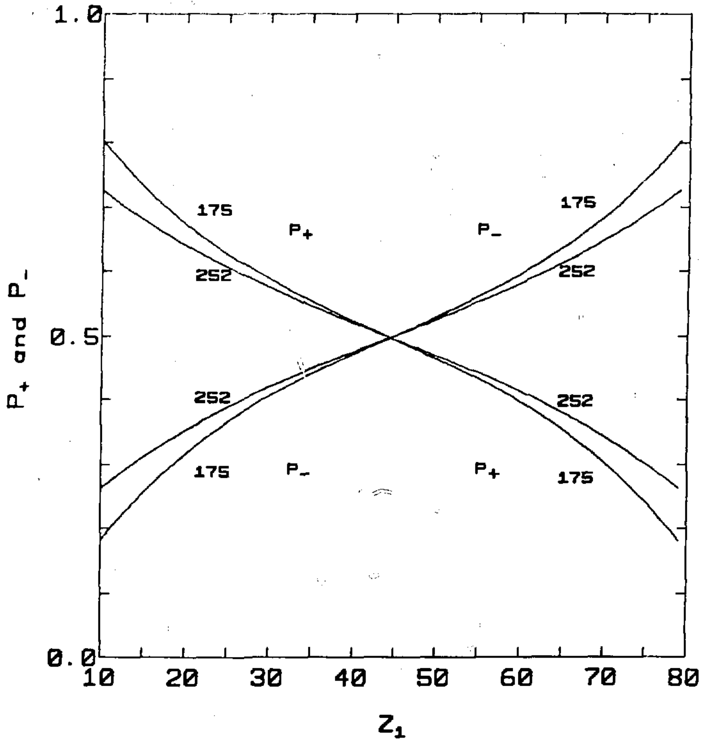

XBL 783-7430

Fig. 30 Transfer probabilities versus the light-fragment atomic number, for both 175 and 252 MeV projectile energies.

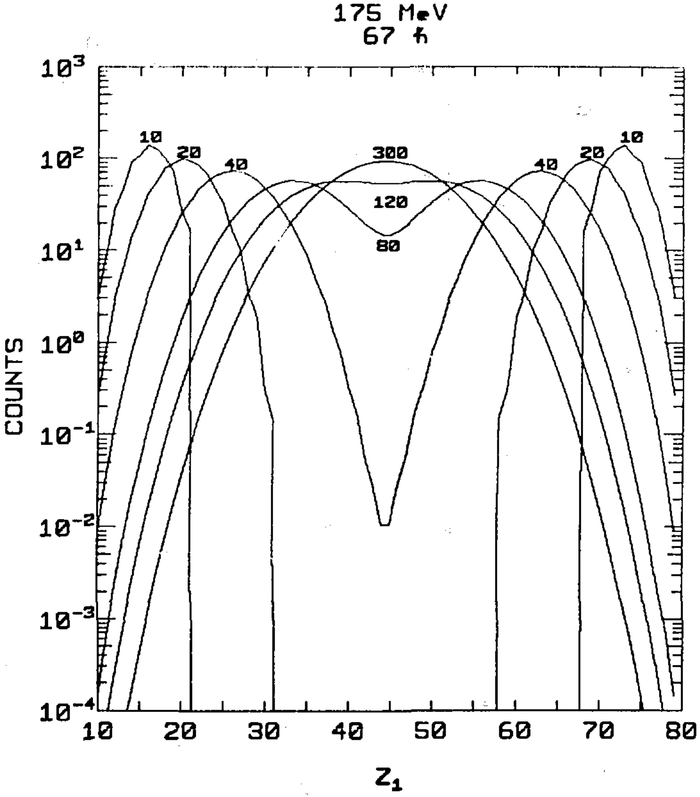

XBL 783-7431

Fig. 31 Calculated distribution of elements at six different times, based on diffusion model. 175 MeV projectile energy.

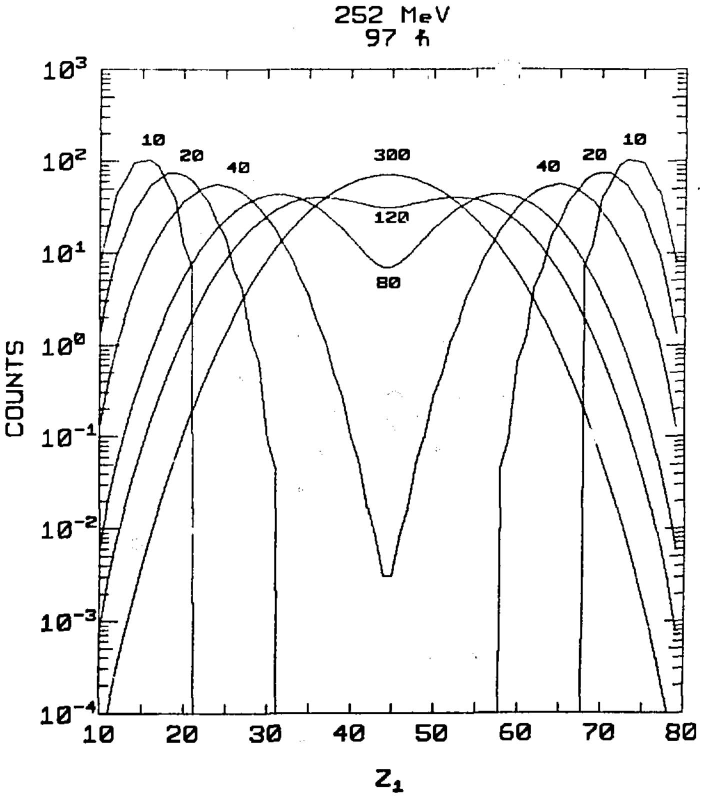

XBL 783-7432

Fig. 32 Same as Fig. 31 for 252 MeV projectile energy.

120 and 300. We see the drift of the light and heavy mass fragments towards symmetry. The movement is quick early in the reaction, slowing down as the equilibrium distribution is obtained.

In Figure 33 we overlay the Z distributions for both reaction energies at four times - 10, 40,80 and 300 Δt units. The distribution in the 175 MeV case moves slightly faster because the positive transfer probability is somewhat larger. On the other hand, the equilibrium in the 252 MeV case is somewhat broader, due to the greater temperature at this reaction energy. We see in both cases that the distribution is fully equilibrated at t = 300, and that the degree of equilibration at the other times is similar for both reactions. We can now understand our earlier observation that the degree of equilibration of the Z distribution at the two reaction energies is quite similar. This arises from the fact that the time development and lifetime (in Δt units) for both systems are alike for Z's from 20 to 30.

5. Calculation of Diffusion with Secondary Fission

Up to this point, our analysis of the elemental distributions has focussed on understanding their degree of equilibration. To this end, we have studied the relative yield as a function of Z. It is now appropriate to test our understanding of the absolute cross section.

Considerable theoretical effort has been devoted to explaining the Z distributions of heavy ion reactions, employing a diffusion model based on the master equation (see section III.B.1.) We have used a code developed by Sventek and Moretto to calculate Z distributions in the 175 and 252 MeV Ne + Au reactions (Mo 75, Sv 78).

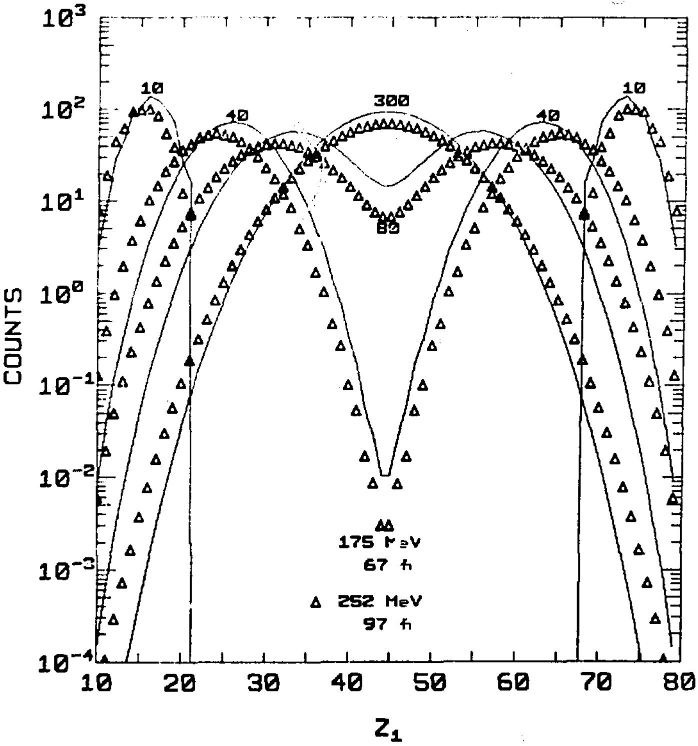

XBL 783-7433

Fig. 33 Same as Figs. 32 and 33 - overlay of diffusion calculations at both 175 and 252 MeV projectile energies at four different times.

This program solves the equations of motion for the reaction by employing a liquid drop potential augmented by one-body friction. From this it calculates several key dynamical properties: the mean reaction lifetime, the average overlap of the nuclei and the amount of angular momentum converted to internal spin of the fragments produced. With this information it then calculates the Z distribution produced by diffusion and the angular distribution for each product. This code has successfully reproduced the Z distributions of several reactions. When applied to the Ne + Au case, the calculated Z distribution differs greatly from the data in both magnitude and slope. The observed center of mass cross section increases monotonically from about 1 to 100 mbarns, in the Z range from 20 to 34. The calculated distribution in this Z range falls steadily from about 5 to less than 0.1 mbarns.

This discrepancy between theory and experiment may perhaps be rectified by accounting for the possibility of fission of the compound nucleus or of heavy fragments formed in the reaction. This has been tested in the following manner. The code mentioned above was used to calculate the Z distribution, as well as the excitation energy and internal spin of the heavy fragment, for each incident angular momentum (L). With this information the fission probability was calculated, in competition with neutron emission. The Z distributions from fission were calculated using a Gaussian function. The procedure will now be described in more detail.

The fission barrier with respect to the rotating equilibrium shape is

$$E_f^r = (M^r_{sad} + R^r_{sad}) - (M^r_{eq} + R^r_{eq}) \qquad (12)$$

where M^r_{sad} and M^r_{eq} are the masses of the rotating saddle and equilibrium shapes respectively, and R^r_{sad} and R^r_{eq} are the corresponding rotational energies. The energy of the rotating equilibrium shape with respect to the rotating spherical shape is

$$E_{II} = (M^r_{eq} + R^r_{eq}) - (M^r_{sph} + R^r_{sph}) \qquad (13)$$

where M^r_{sph} is the mass of the spherical nucleus and R^r_{sph} is the corresponding rotational energy. E_{II} is generally negative.

The quantities E_f^r and E_{II} are functions of the fissility parameter (x) and the rotation parameter (y). These are expressed in terms of spherical liquid drop energies as

$$x = E_c^o/2\,E_s^o = 0.01995\ Z^2/A$$

$$y = E_r^o/E_s^o = 1.879\ J^2/A^{7/3}$$

where E_c^o is the self-Coulomb energy, E_r^o is the rotational energy, E_s^o is the surface energy and J is the angular momentum. When calculating the rotation parameter of the heavy fragment, the J is taken as the internal spin obtained from Sventek's code. The quantities E_f^r and E_{II} have been calculated by Plasil and Swiatecki, and are tabulated by Vandenbosch et al (Va 73, pp 246, 248).

The excitation energy at specified L-wave, L, is calculated in Sventek's code with respect to the rotating spherical contacting nuclei. Therefore the fission barrier of interest is

$$B_f = E_f^r + E_H \tag{14}$$

The barrier to emission of an s-wave neutron, B_n, is taken as the normal ground-state neutron binding energy. Using these quantities, the ratio of neutron emission to fission probability can be expressed as (Va 73, Eq. VII-7):

$$\frac{\Gamma_n}{\Gamma_f} = \frac{4A^{2/3}a_f\,(E-B_n)}{K_o a_n [2a_f^{1/2}(E-E_f)^{1/2}-1]} \cdot \exp[2a_n^{1/2}(E-B_n)^{1/2} - 2a_f^{1/2}(E-E_f)^{1/2}] \tag{15}$$

where $K_o = h^2/2mr_o^2 \approx 10$ MeV, A is the atomic number, a_f and a_n are the level density parameters at the saddle point for fission and for neutron emission respectively. It has been noted by many authors that the ratio a_f/a_n may range from 1.0 to 1.5, depending on the mass and excitation energy (Va 73, p 236; Mo 73).

It is important to include the possibility of fission after single or multiple neutron emission. After each neutron emission, the excitation energy is revised by subtracting the neutron binding energy and the average neutron kinetic energy (twice the temperature of the residual nucleus). The ratio Γ_n/Γ_f is recalculated at each step. The total fission probability for the heavy fragment (or compound nucleus) of atomic number Z at angular momentum L is

$$P_f^I(Z) = \sum_{k=1}^{N} P_f^{(k)} \left(\prod_{i=1}^{k-1} (1-P_f^{(i)}) \right) \tag{16}$$

where $P_f^{(k)}$ is the fission probability at the k-th step. This is related to the neutron and fission widths at this step by

$$P_f^{(k)} = \Gamma_f^{(k)}/(\Gamma_f^{(k)} + \Gamma_n^{(k)}) \quad . \tag{17}$$

The upper limit of the sum in Eq. (16) is determined by allowing the iteration to proceed until either fission or neutron emission is overwhelmingly likely. The specific condition used for terminating the iteration is

$$P_f^{(k)} > 0.99 \quad \text{or} \quad P_f^{(k)} < 0.01 \quad .$$

The normalized distribution of elements Z_f arising from the fission of a heavy fragment of atomic number Z is approximated by (Ni 65)

$$F(Z_f ; Z) = N \exp[-(U - \tfrac{1}{2})^2 / C_m] \tag{18}$$

where: $U = Z_f/Z$

$C_m = 2T/K_m$

K_m = stiffness of the potential in the mass-asymmetry coordinate. Values for K_m were taken from Fig. 14 of Ni 65.

$$N = \text{normalization} = \int_0^1 \exp[-(U - \tfrac{1}{2})^2 / C_m] dU \quad .$$

The final fission yield of element Z is obtained by summing over the full L-wave and Z ranges:

$$\sigma_{\text{fission}}(Z_f) = \sum_L \sum_Z P_f^L(Z)\, \sigma_{\text{diff}}^L(Z)\, F(Z_f;\, Z) \qquad (19)$$

where $\sigma_{\text{diff}}^L(Z)$ is the calculated cross section for diffusive production of element Z at incident angular momentum L.

The distribution of heavy fragments $\sigma_{\text{diff}}^L(Z)$, as predicted by the diffusion calculation, are shown in Figs. 33.1 and 33.2 for five L-waves. One sees strong peaking of the distribution around Z = 80. The breadth of the distribution decreases with angular momentum. The diffusion calculation assumes that if the light-fragment atomic number is reduced to 4 or less, a compound nucleus is irrevocably formed. One sees that the compound nucleus cross section (at Z = 89) calculated in this way decreases with increasing L-wave, due to the decreasing life time.

The multi-chance fission probability of Eq. (16) is plotted in Figs. 33.3 through 33.9 for the 175 and 252 MeV cases. Values of the level density parameter ratio, a_f/a_n, ranging from 1.0 to 1.6 are used. Each figure shows the fission probability for three L-waves. Consider the 175 MeV case first. When the level density parameter ration (LDPR) is 1.0 (Fig. 33.3) the fission probability falls precipitously for all elements lighter than the compound nucleus. When the LDPR is 1.2 (Fig. 33.4) the compound nucleus and the several heaviest fragments have appreciable fission probabilities. When the LDPR is 1.4 (Fig. 33.5) fission occurs appreciably for fragments as

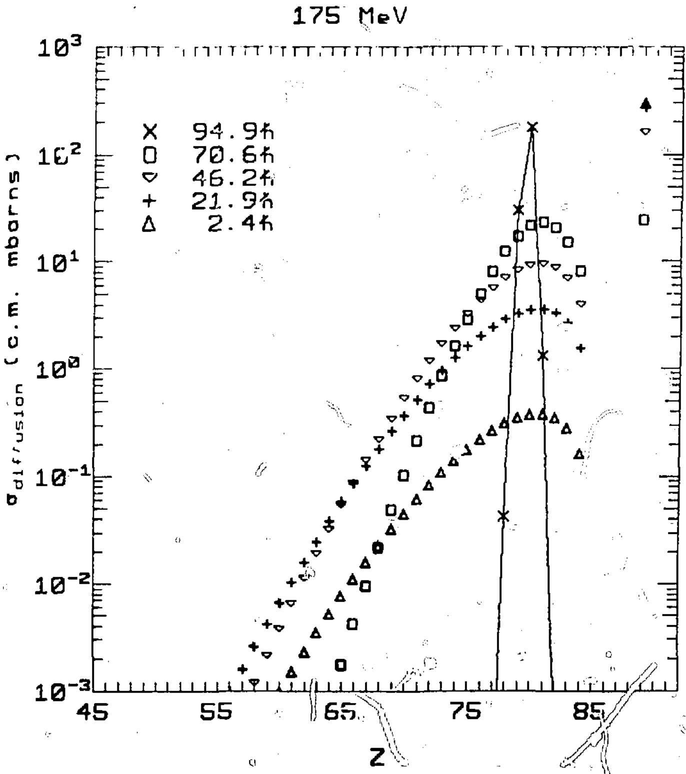

XBL 785-8004

Fig. 33.1 Calculated diffusion yield for heavy fragments, at five incident angular momenta. 175 MeV projectile energy.

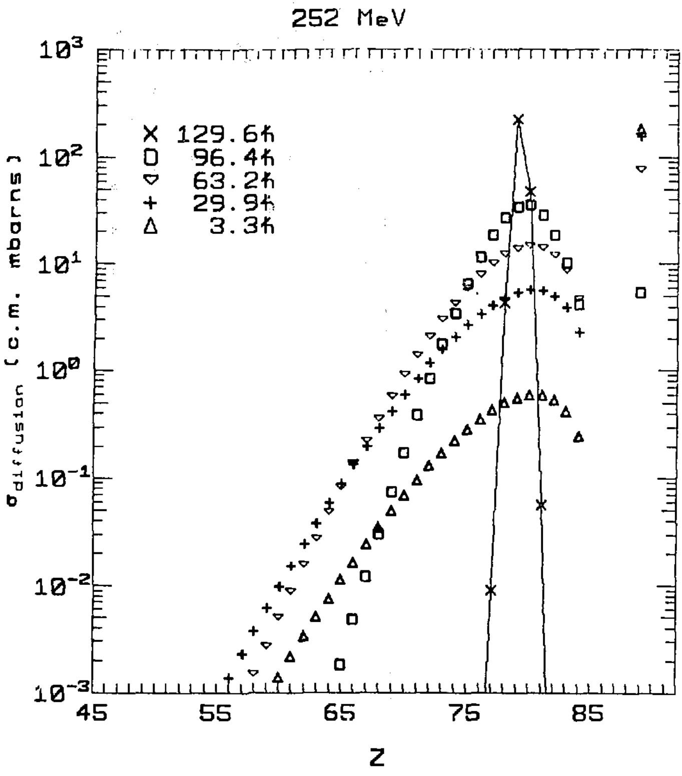

XBL 785-8903

Fig. 33.2 Same as Fig. 33.1. 252 MeV projectile energy.

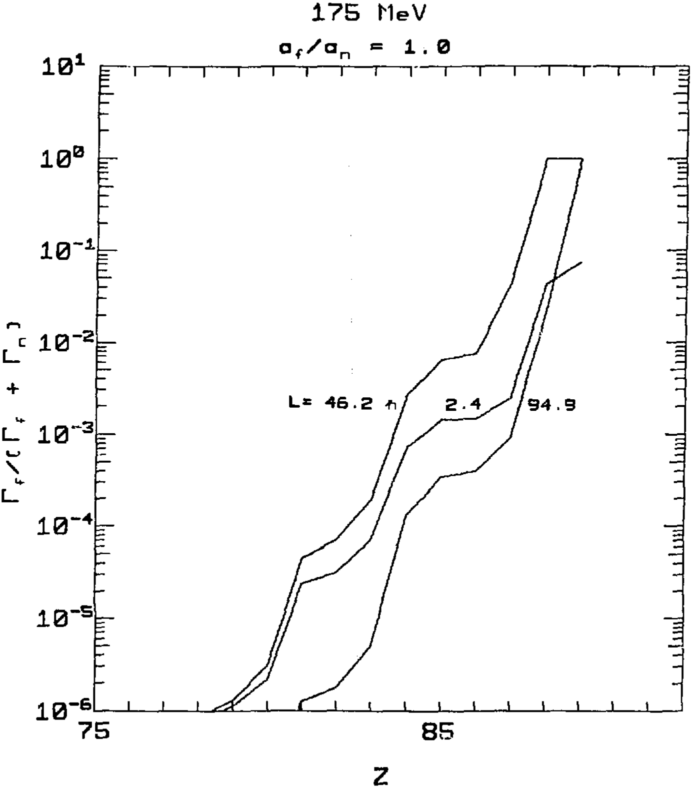

XBL 785-8908

Fig. 33.3 Calculated multi-chance fission probability for heavy elements, at 3 incident angular momenta. LDPR = 1.0. 175 MeV projectile energy.

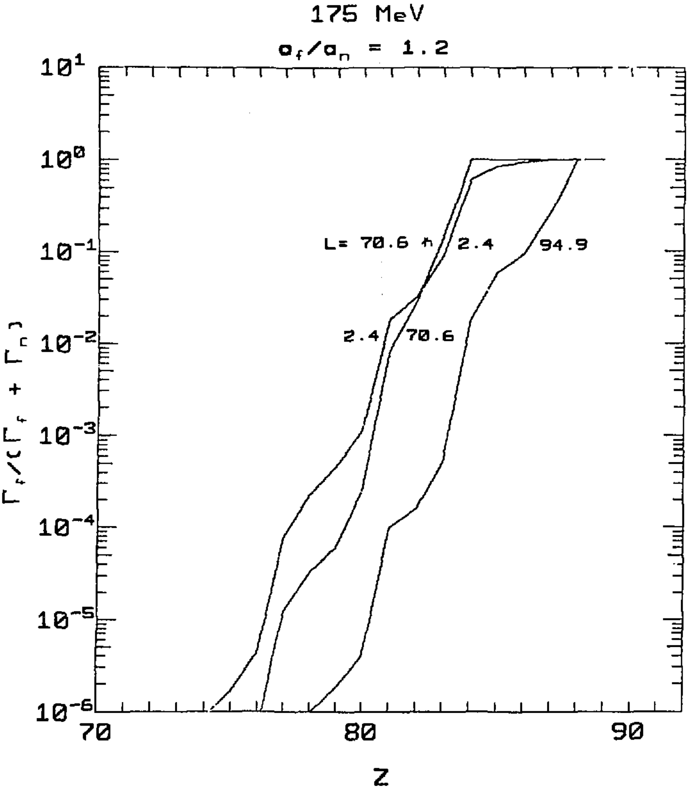

XBL 785-8909

Fig. 33.4 Same as Fig. 33.3. LDPR = 1.2. 175 MeV projectile energy.

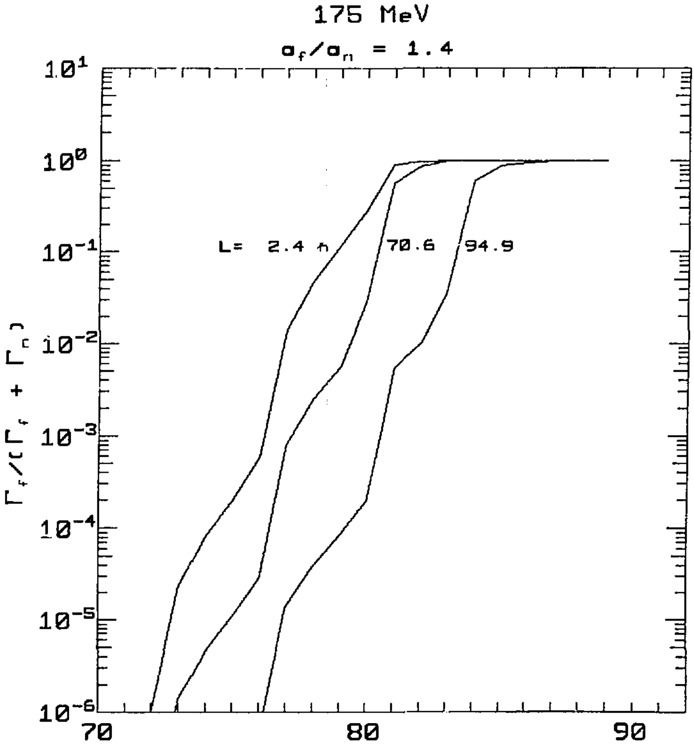

XBL 785-8910

Fig. 33.5 Same as Fig. 33.3. LDPR = 1.4. 175 MeV projectile energy.

light as the target. Further increase in the LDPR will extend the range of significant fissility to lighter products. However, since the calculated diffusion yield drops rapidly for products lighter than Au, additional increases in the LDPR will have diminishing effect on the fission yield. A similar phenomenon is observed in the 252 MeV case (Figs. 33.6 to 33.9). When the LDPR is 1.4, appreciable fissility is to be expected from fragments somewhat lighter than Au (as well as heavier ones). Increase of the LDPR to 1.6 indeed extends the range of fissility to lighter fragments. It will be seen that this has a diminished effect on the fission yield, due to the sharp decrease in diffusion cross section for these lighter nuclei.

By employing the largest values of the LDPR (1.4 at 175 MeV, 1.6 at 252 MeV) qualitative agreement can be obtained between calculation and experiment in the Z range from about 20 to 34. In Figs. 33.10 and 33.11 the fission yield is added to the diffusion yield, and compared with the experimental data (the single points). Also, the diffusion yield is shown alone. One sees that above about Z = 25 the fission yield dominates the calculated cross section. The fission yield increases with increasing Z, as does the data, while the diffusion yield decreases. One notices that the diffusion yield dominates for the lighter products, and considerably exceeds the data. This is most likely to be due to the limited angular range over which the experimental data were measured. The cross section at the most forward angles may have been significantly underestimated by extrapolation from the measured angular range,

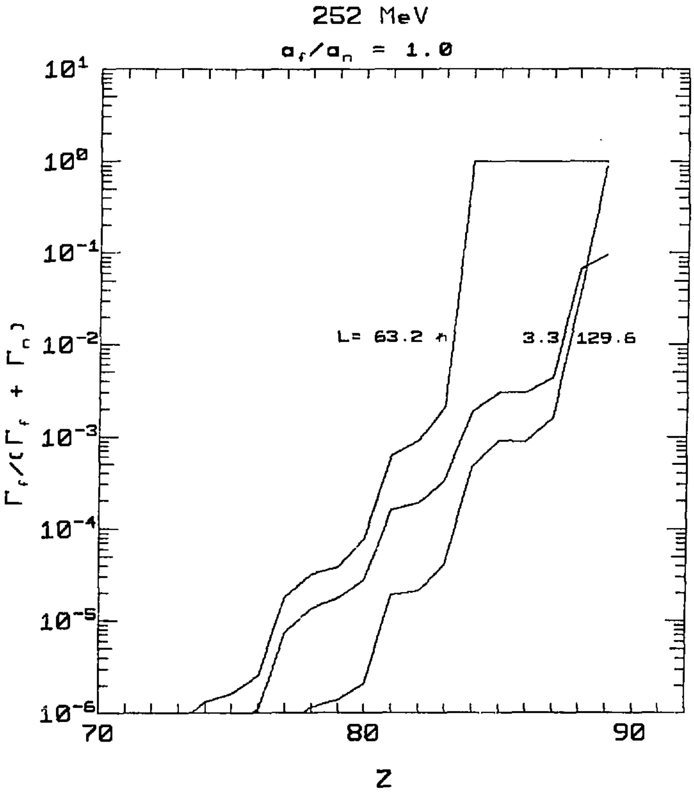

XBL 785-8905

Fig. 33.6 Same as Fig. 33.3. LDPR = 1.0. 252 MeV projectile energy.

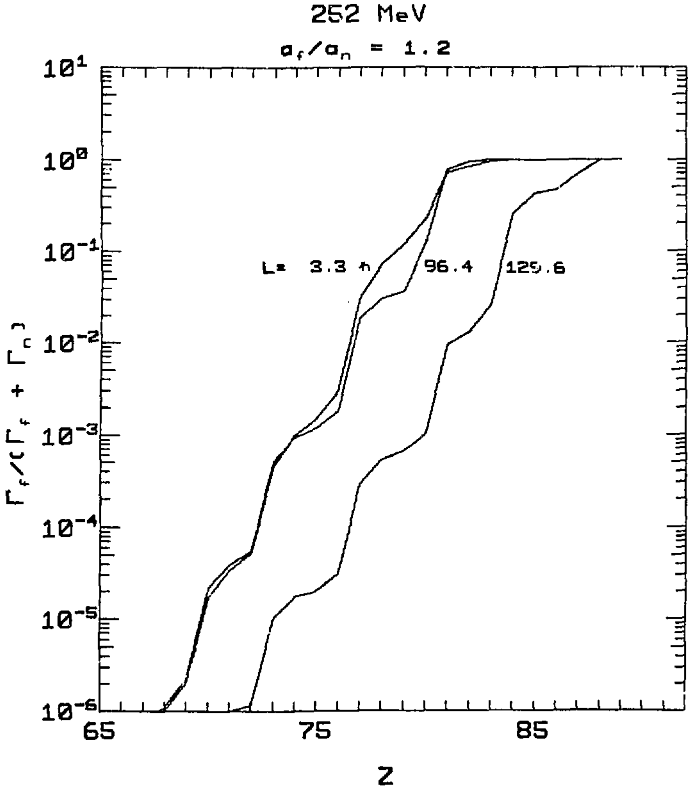

XBL 785-8906

Fig. 33.7 Same as Fig. 33.3. LDPR = 1.2. 252 MeV projectile energy.

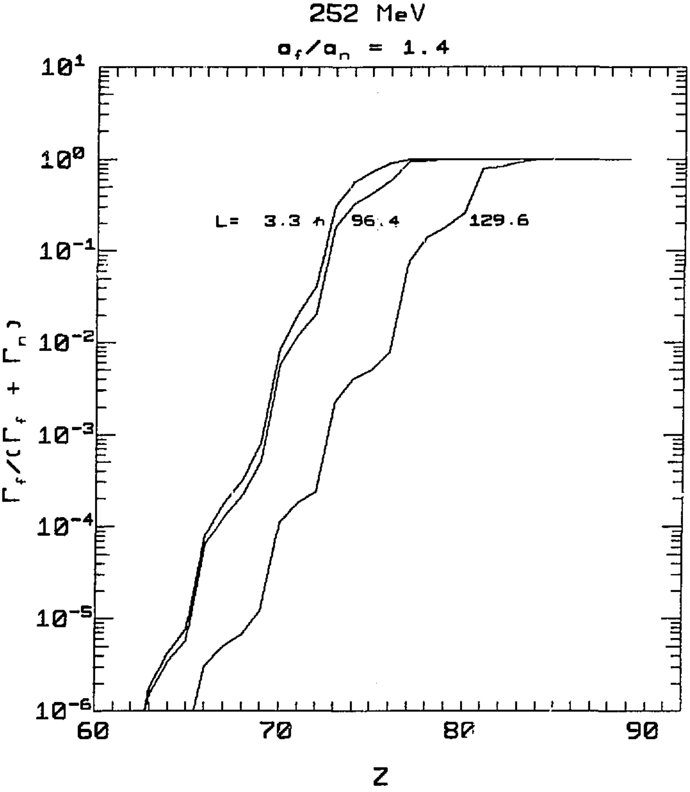

XBL 785-8907

Fig. 33.8 Same as Fig. 33.3 LDPR = 1.4. 252 MeV projectile energy.

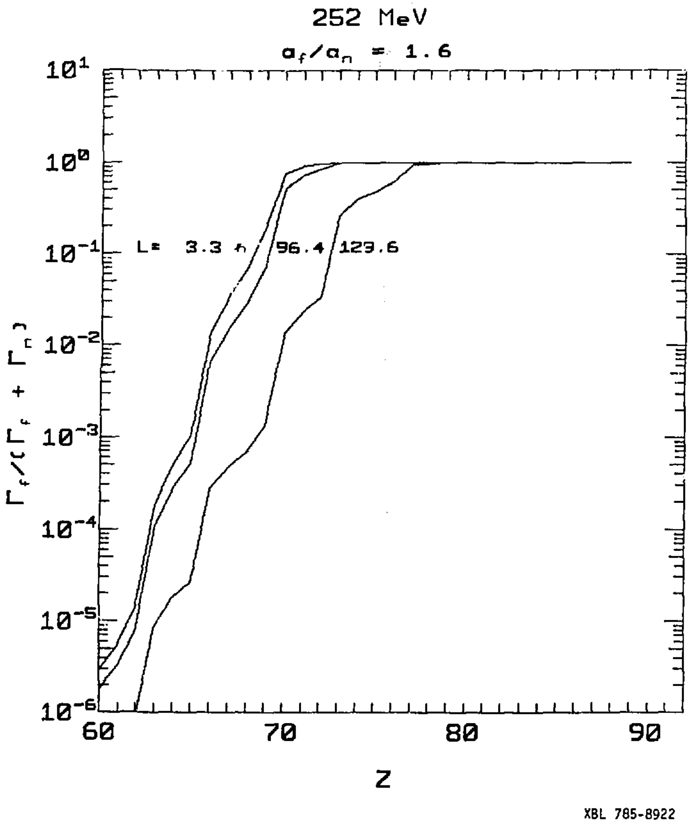

XBL 785-8922

Fig. 33.9 Same as Fig. 33.3. LDPR = 1.6. 252 MeV projectile energy.

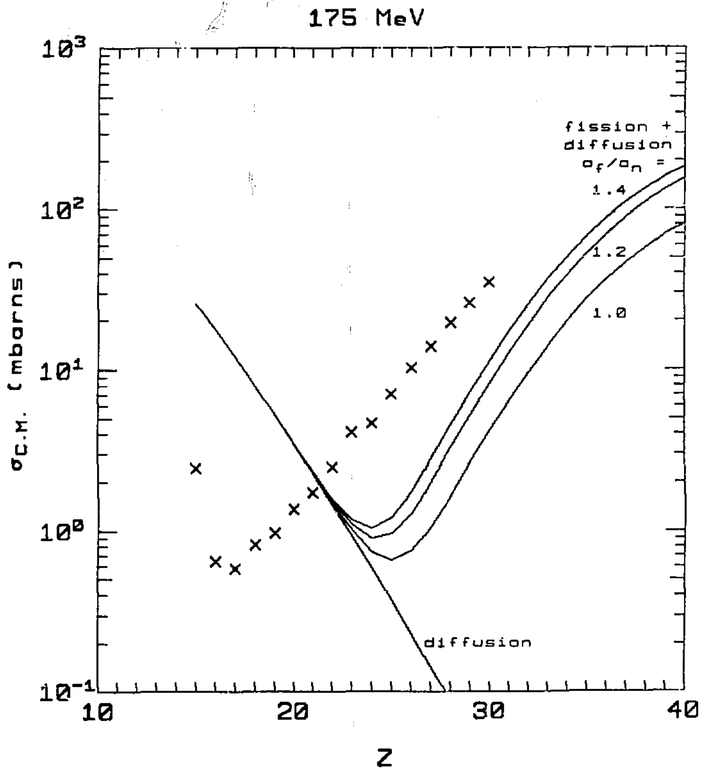

XBL 785-8902

Fig. 33.10 Calculated diffusion and diffusion + fission yield versus Z, for 3 different values of the LDPR. The points (X's) are measured cross sections extrapolated over the full angular range. 175 MeV projectile energy.

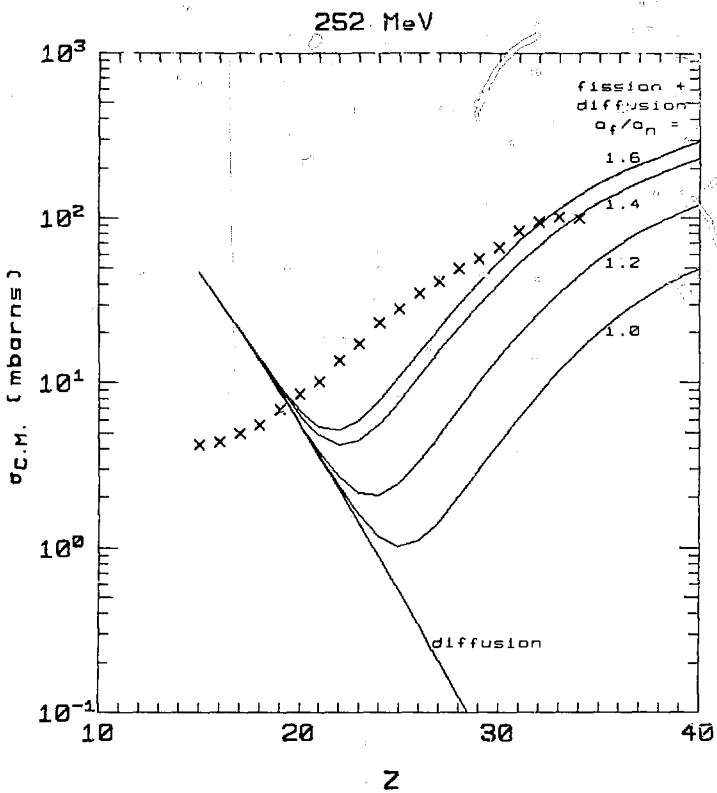

XBL 785-8923

Fig. 33.11 Same as Fig. 33.10 for four values of the LDPR and 252 MeV projectile energy.

because the slope of the angular distribution of these lighter products increases at forward angles.

In the 175 MeV case the calculated fission + diffusion yield falls short of the data (above $Z = 24$) by a factor ranging from 3 to 4. In the 252 MeV case, the ratio of the experiment to theory ranges from 2 (at $Z = 22$) to 1 (at $Z = 32$). Considering the simplicity of the fission calculation, this discrepancy is not too discouraging. One is encouraged to think that secondary statistical fission of diffusion-produced heavy fragments (including the compound nucleus) may be the dominant source of reaction products above about $Z = 20$. Consistent with this, products of the 252 MeV reaction heavier than about $Z = 21$ display nearly or completely symmetrical angular distributions of the form $1/\sin\theta$. Angular symmetry for products of the 175 MeV reaction first appears at somewhat heavier Z's. Upon considering the fact that the data exceeds the theoretical calculation, one is tempted to wonder if an additional fission path may be available to the system. One such possibility -- dubbed "proximity" fission -- envisions enhanced fission of the target under the influence of the Coulomb field of the proximal projectile nucleus. Further theoretical and experimental study is needed.

C. Angular Distributions

1. General Considerations

Examination of the angular distributions of products of highly inelastic reactions provides a direct qualitative review and confirmation of our understanding of these reactions. We shall provide this review by consideration of four reactions, before returning to the Ne + Au case.

The angular distributions of reactions produced by N, Ne and Ar projectiles provides a simple illustration of the non-compound-nucleus nature of these reactions. Center of mass angular distributions for the N + Ag (Mo 75a), Ne + Ag (Ba 75) and Ar + Au (Mo 76) reactions are shown in Figs. 34 to 36. These distributions are generally asymmetrically peaked in the forward direction, especially for products similar to the projectile. This indicates a coupling between entrance and exit channels. The reaction complex can distinguish the forward and backward directions, which a compound nucleus cannot do.

The degree of forward peaking provides insight into the lifetime of the reaction complex. The lifetime must be short, but not too short, compared with the mean rotational period of the complex. It must be short enough to prevent multiple rotations before breakup, which would cause the angular distribution to be symmetrical about 90°; it must be long enough to provide some rotation past 0°, otherwise the angular distributions would peak at a side angle. Such side peaking is in fact observed in the reaction of Kr + Au (Sv 76, Ru 77). In Fig. 37 one sees that angular distributions for products of this reaction not too different in mass from the projectile display very marked side-angle peaks.

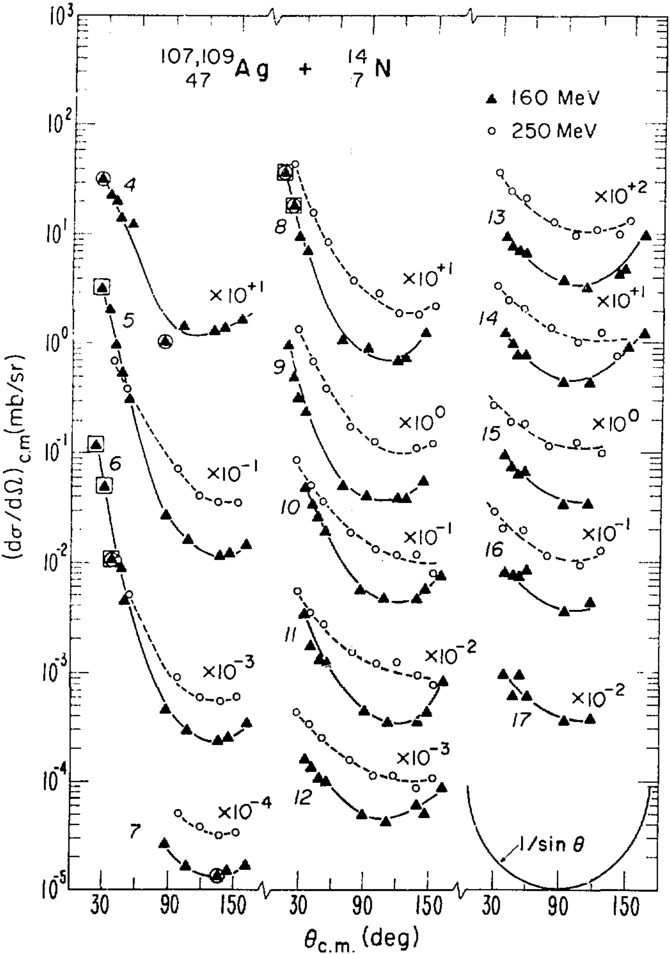

Fig. 34 Experimental center of mass angular distributions for the reaction N + Ag (Mo 75a).

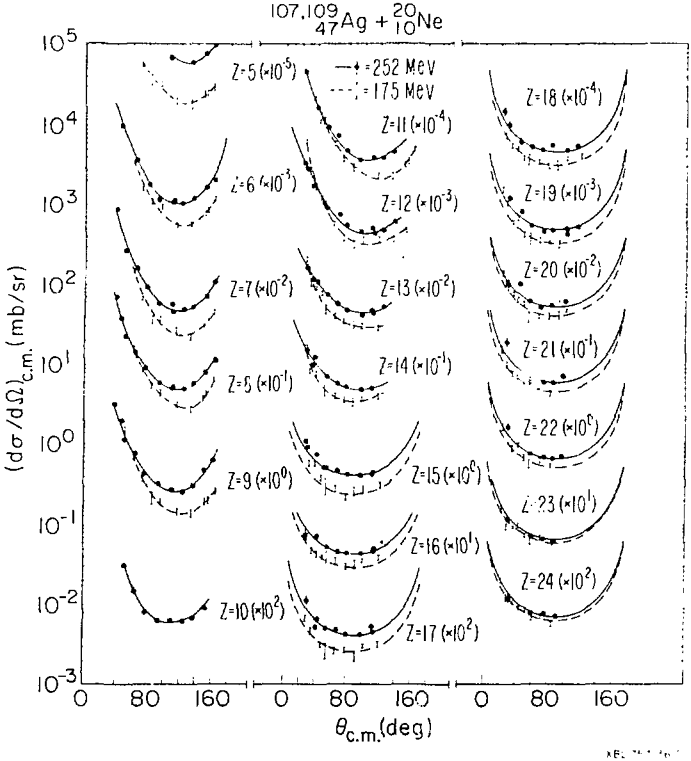

Fig. 35 Same as Fig. 34 for Ne + Ag (Ba 75).

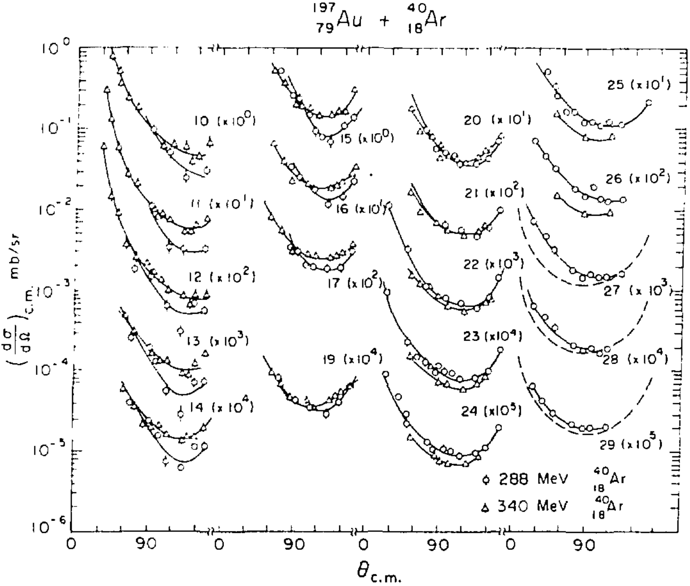

Fig. 36 Same as Fig. 34 for Ar + Au (Mo 76).

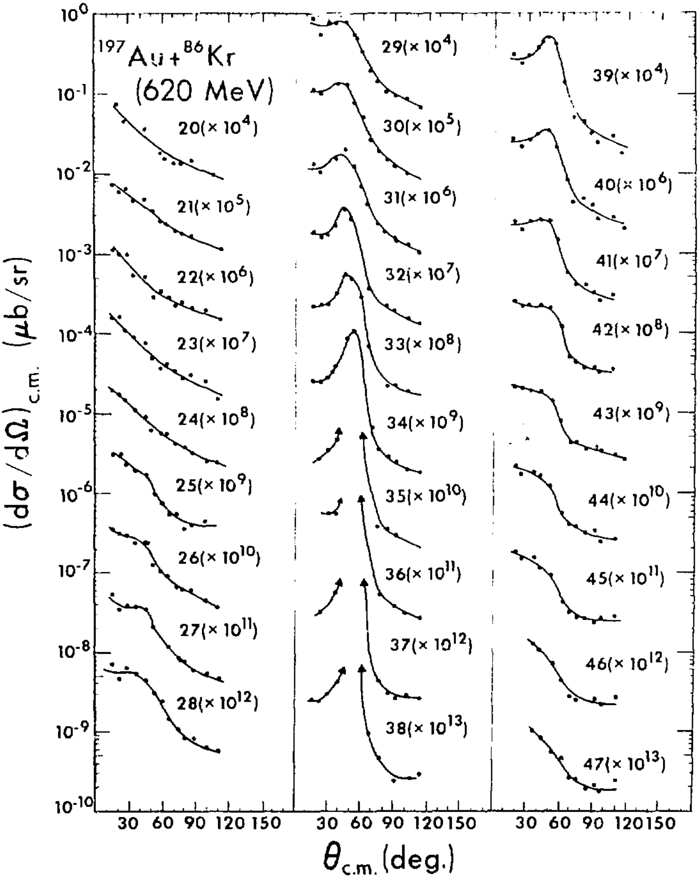

XBL 7512-9891

Fig. 37 Same as Fig. 34 for Kr + Au (Sv 76, Ru 77).

Another important implication arises from the fact that nearly all products exhibiting side- or forward-peaked angular distributions, also display nearly completely equilibrated kinetic energy spectra. This indicates that the relaxation of the kinetic energy occurs on a time scale which is quite short compared to both the rotational period and the relaxation time for the mass asymmetry degree of freedom.

By far the most revealing feature of the angular distributions is their change in shape with product Z. The degree of forward peaking (or side peaking in the case of Kr + Au) is stronger for fragments closer in Z to the projectile, and decreases progressively for fragments further removed from the projectile. This phenomenon finds its qualitative explanation in the time required for diffusive motion along the mass asymmetry coordinate. Products near in Z to the projectile are produced quickly and can decay with a short lifetime. The angular distributions for these products are then forward peaked (N, Ne or Ar projectiles), or side peaked (Kr + Au). Products more different in Z generally require longer diffusion times. Such products of N, Ne or Ar reactions display angular distributions which approach, in varying degree, the 1/sinθ shape expected of a reaction at high angular momentum which may rotate as much as one or several complete revolutions. The angular distributions of products of the Kr + Au reaction, both lighter and heavier than the projectile, display progressive recession and finally disappearance of the side-angle peak. As with the lighter projectiles, this indicates increasing lifetime of the reaction complex relative to the rotational period.

An interesting insight is obtained by noticing how the Z dependence of the angular distribution varies from one reaction to another. In the N + Ag and Ne + Ag reactions, the angular distributions remain quite asymmetrical, and strongly forward peaked, down to the lowest elements detected. On the other hand, the angular distributions of Z's above the projectile rapidly become symmetrical about 90°. For example, the angular distribution for element 15 in the Ne + Ag reaction has the form of $1/\sin\theta$. This has been explained by noting (Mo 76b) that the initial mass asymmetry of the projectile-target complex in these two reactions is (for most angular momenta) to the left of the Businaro-Gallone peak in the potential energy. (The Businaro-Gallone peak is the maximum in the potential energy, along the mass asymmetry axis. This maximum is seen very clearly in Fig. 28). Consequently, products lighter than the projectile are populated very quickly due to the rapid drift on the steep potential slope. On the other hand, products heavier than the projectile are more slowly populated by "uphill" spreading of the probability distribution. The consequence is rapid disappearance of forward peaked angular distributions for products heavier than the projectile.

It is now instructive to compare the Z dependence of the angular distribution for the Ar + Au reaction. In this case, the initial mass asymmetry of the projectile-target complex is to the right of the Businaro-Gallone peak, on a steep slope of the potential energy. The Z distribution rapidly drifts towards more symmetric configurations, and the angular distributions (Fig. 36) are observed to retain their forward peaking up to Z = 28. The expected decrease in forward peaking for products lighter than Ar is not observed. It has been pointed out in this connection (Mo 76b) that the kinetic energy spectra of these light products are not fully relaxed, while the products heavier than the projectile display equilibrated energy spectra.

2. The Ne + Au Reaction

Experimental center of mass differential cross sections for the 175 and 252 MeV reactions are shown in Figs. 38 and 39. Brief examination of these figures shows that products similar in mass to the projectile display angular distributions which are not symmetrical about 90°, but rather are strongly peaked at forward angles. The degree of forward peaking diminishes for products further removed from the projectile. One notices this decrease of forward peaking for products both lighter and heavier than Ne. In these features, the present angular distributions are similar in kind to those of the reactions just discussed.

A further interesting point is the noticeably different Z dependence of the angular distributions in the 175 and 252 MeV reactions. At the lower projectile energy the angular distributions are more sharply forward peaked, and retain their angular asymmetry to higher Z's, than at the higher energy. This same feature is seen also in the N + Ag, Ne + Ag and Ar + Au reactions discussed earlier. Two possible explanations are apparent. In connection with the Ar + Au reaction, it was suggested (Mo 76) that this may be a temperature effect. Because the diffusion depends on V_Z/T and not on V_Z alone, the driving force for diffusion may be stronger in the lower energy (lower temperature) reaction. It should be kept in mind that the range of angular momenta

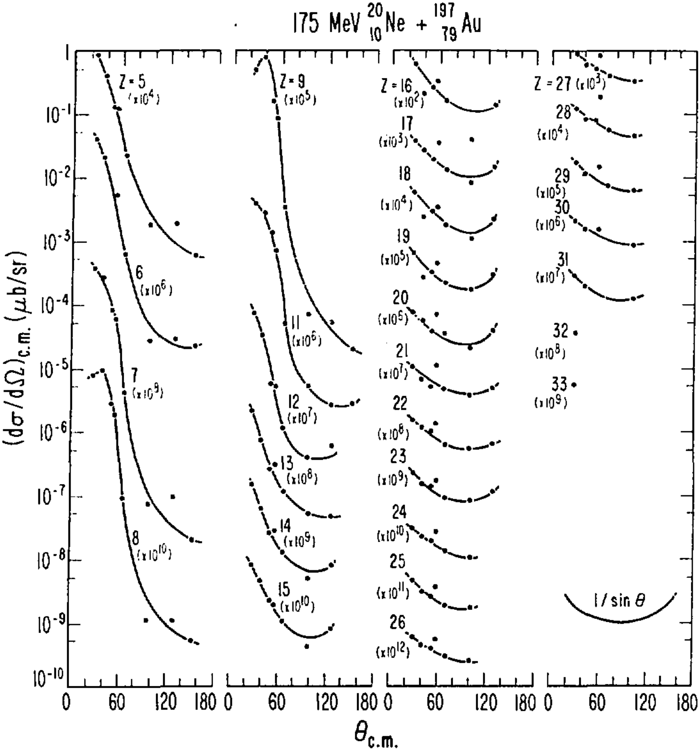

XBL 7710-2095

Fig. 38 Same as Fig. 34 for Ne + Au. 175 MeV projectile energy.

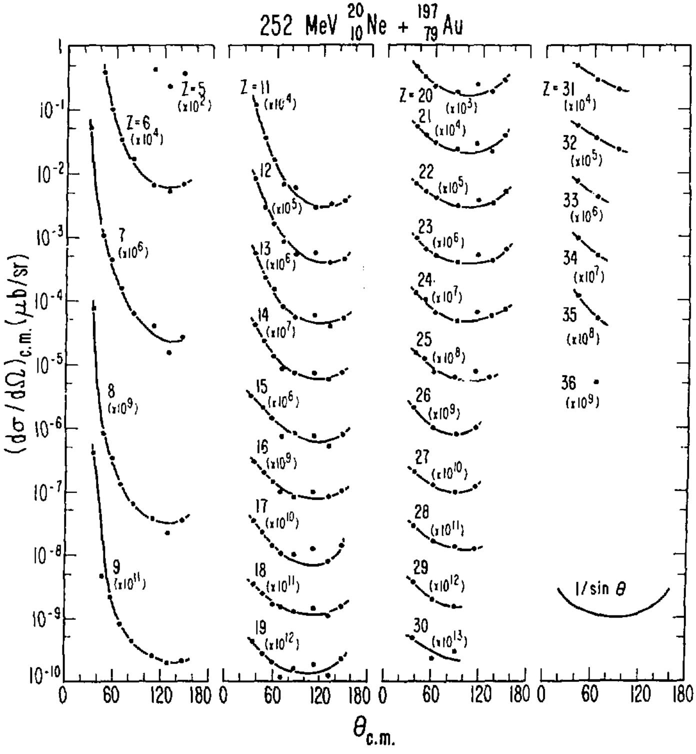

Fig. 39 Same as Fig. 34 for Ne + Au. 252 MeV projectile energy.

is different for the two reactions, and that therefore the average potential is different (and slightly steeper) at the higher energy. Alternatively, the higher angular momenta likely to contribute to the high energy reaction could possibly explain the less sharply peaked angular distributions by increasing the angular velocity of the reaction complex; the shape of the distribution depends on the relative magnitude of the lifetime and the rotational period. This also is not a clear-cut explanation. We know from our study of the kinetic energy spectra that the moment of inertia increases with angular momentum, thus perhaps preventing an increase in the angular velocity. It is fair to say that the widely observed phenomenon of increased angular symmetry with projectile energy is not thoroughly understood.

3. Estimation of the Ne + Au Reaction Lifetime

In Sections IIIA and B we have examined the extent of equilibration of the energy and Z distributions. We have completed our analysis of these fundamental features of deep inelastic reactions without any discussion of the absolute time scale in which these reactions proceed. It is from the angular distributions that we shall deduce -- in an approximate manner -- absolute lifetimes.

The angular distribution of a particular element is the result of the full distribution of reaction lifetimes for that product. Our first aim is to correlate the angle at which a particular event decayed, with the lifetime for that event. One needs to know the "zero time" decay angle (θ_0) to which the event would decay, where the complex to break up immediately after relaxation of the kinetic energy. One also must know the angular frequency (ω) with which the reaction complex rotates. 0_o is a function of the impact parameter, but in all cases we shall assume it to be a small angle from the forward beam axis, forward of the angular range of data collection. This rather drastic simplification is partly justified by noting that the largest contribution to the cross section arises from the larger impact parameters. Also it is to be expected that the projectile is deflected forward quite early in the reaction by the nuclear attraction which it experiences. Furthermore, that short lifetimes correspond to deflection to forward angles in this reaction is supported by the discussion, in the previous two sub-sections, of the Z dependence of the angular distributions.

The angular frequency with which the complex rotates likewise depends on the entrance channel angular momentum. It also fluctuates in time as the moment of inertia changes due to shape vibrations. We shall use that value of ω which arises from the equilibrium deformation of the touching nuclei at the average angular momentum. The calculation of the equilibrium deformation (in Section III.A) assumes that the nuclei are rigid ellipsoids. The following short table shows the value of ω and related quantities for the elements we shall examine.

Z	E_{proj} (MeV)	ρ_{eq} (fm)	L_{ave} ($\hbar$)	ω (10^{20} radians/sec)
14	175	1.29	67	3.03
17	175	1.31	67	2.71
23	175	1.34	67	2.24
14	252	1.33	97	4.18
18	252	1.36	97	3.55
23	252	1.38	97	3.08

Figures 40 and 41 show center of mass angular distributions (of the form $d\sigma/d\Omega$) for three elements produced in the 175 and 252 MeV reactions. The yield at any angle arises from both "left handed" and "right handed" reactions - those in which the projectile strikes either the left or right hemispheres of the target (as seen from an incoming projectile nucleus). The amount of rotation and hence the lifetime of the complex needed to direct the daughter light fragment θ degrees to one side of the beam axis is different for "left handed" and "right handed" reactions. Reactions of these two lifetimes are superimposed at any angle. Also superimposed are events in which the complex rotated by more than 360° from θ_o. This effect will be ignored. In the Z = 14, 17 and 18 cases this is quite well justified because the cross section falls so markedly at backward angles. For the Z = 23

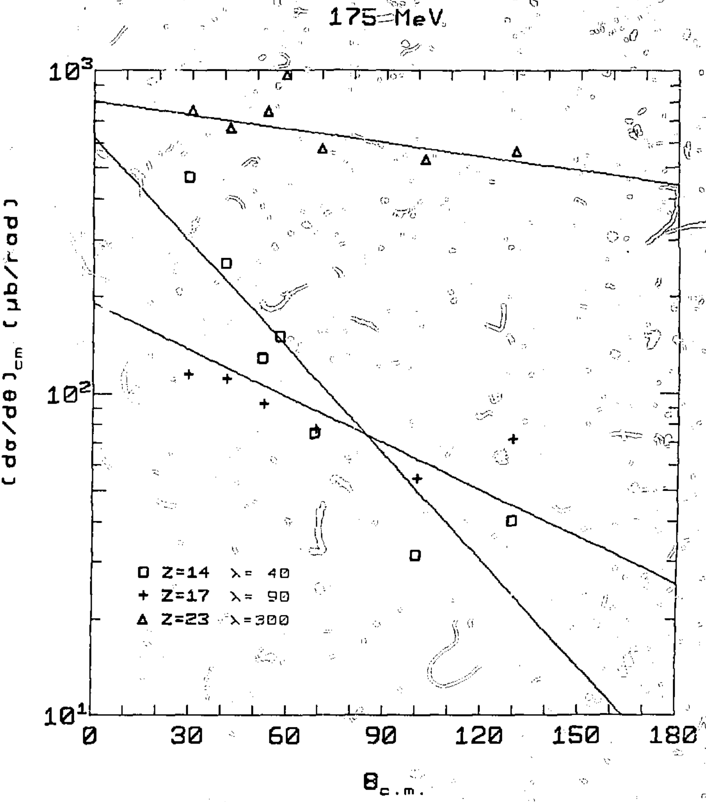

XBL 782-7036

Fig. 40 Selected angular distributions with fitting functions of the form exp $(-\Theta/\lambda)$. Fitting parameter shown for each element. 175 MeV projectile energy.

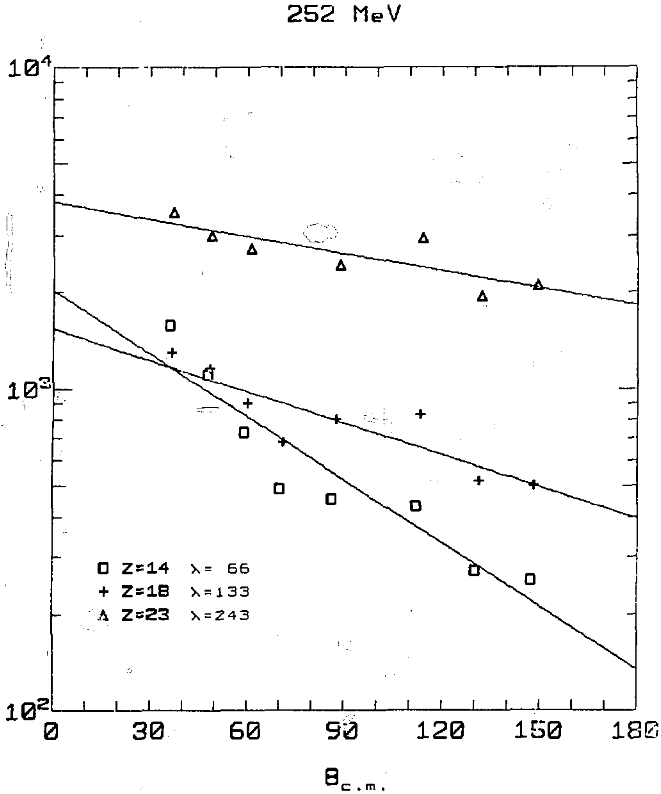

XBL 782-7037

Fig. 41 Same as Fig. 40 for 252 MeV projectile energy.

cases this is not so; the computed lifetimes for this element are to be seen as lower limits.

Contribution to the cross section on one side of the beam at angles larger than the "zero time" angle, Θ_o, is due primarily to reactions in which the projectile struck the target nucleus on the other side. Contribution to the cross section at angles larger than Θ_o by reactions in which the projectile struck on the same side of the target nucleus requires much longer rotation, approaching 360°, and can be ignored without introducing much inaccuracy. We are ignoring the variation of Θ_o with angular momentum, and are primarily considering those large L-waves which bear most of the cross section, and for which Θ_o is small. Our experimental measurements are approximately limited to angles larger than Θ_c and thus primarily represent the distribution of angular rotations for just "left handed" or "right handed" reactions.

Consequently the cross section for element Z at Θ degrees from the beam axis (where $\Theta > \Theta_o$) is proportional to the probability of the reaction complex rotating by $\Theta_o + \Theta$ degrees before decaying to produce element Z. The angular distribution for each Z has been reproduced for a number of reactions by employing the time dependent Z distributions calculated with the master equation (see Section III B). These distributions are summed over the range of impact parameters, with suitable weighting. With a model for the overall reaction lifetime, this sum is averaged over time to produce the angular distribution.

This is described more fully elsewhere (Mo 75, Sv 76). A much simpler and more qualitative approach is taken here. We shall empirically fit the angular distributions in the range for which they have been measured, and use the fitted functions to calculate the mean angular rotation over the full range of rotation. This fitting is done using a decaying exponential of the form $e^{-\Theta/\lambda}$ which, it is seen from Figs. 40 and 41, approximates the data reasonably well. The fitted values of λ, in degrees, are shown in the figures.

The lifetime associated with decay to angle Θ is $t = (\Theta + \Theta_o)/\omega$. Recall that Θ_o is the angle from the forward beam axis to which the complex would decay, were it to break up immediately after relaxation of the kinetic energy. For the purpose of our estimation of the average lifetime, we can ignore Θ_o as compared to Θ. The average lifetime is

$$t_{ave} = \frac{\int_o^{2\pi} \frac{\Theta}{\omega} \; e^{-\Theta/\lambda} \, d\Theta}{\int_o^{2\pi} e^{-\Theta/\lambda} \, d\Theta} \quad .$$

The following table shows the calculated average lifetimes.

Z	E_{proj} (MeV)	λ (radians)	t_{ave} (10^{-21} sec)
14	175	0.698	2.3
17	"	1.57	5.4
23	"	5.24	11
14	252	1.15	2.7
18	"	2.32	5.3
23	"	4.24	7.8

We have now achieved our aim of qualitatively estimating the absolute reaction lifetimes. In the Z range from 14 to 23 it increases from about 10^{-21} to 10^{-20} second. Lighter products are undoubtedly produced more quickly. In the previous section, we found that the lifetimes of Z's from 20 to 30 were all nearly the same. The lifetimes of such products, computed by the method of the present section, will be close to the value for element 23 because the angular distributions of these elements are all similar in shape. A lifetime of 10^{-20} second should be viewed as a lower limit for products heavier than atomic number 23. It is worthwhile to note that mean lifetimes for the Ar + Ag (Mo 75) and Kr + Au (Sv 76) reactions, calculated with more precise techniques, are 2.5 and 3.5 × 10^{-21} seconds respectively. (The latter is the value at $L = 0\hbar$).

A. Appendix I. Derivations

1. Derivation of Kinetic and Potential Energy Equations

The following basic quantities must be defined:

L = total angular momentum.

ℓ = orbital angular momentum.

I = total moment of inertia of the reaction complex.

I_j = moment of inertia for fragment j (= 1 or 2).

I_r = orbital moment of inertia of the reaction complex.

M_j = mass of fragment j.

M = reduced mass of the complex = $M_1M_2/(M_1 + M_2)$.

R_j = cylindrical symmetry semi-axis of fragment j.

b_j = transverse semi-axis of fragment j.

R_{jo} = spherical radius of fragment j = $1.225\ M_j^{1/3} + 1.0$ fm.

$\rho = R_1/R_{1o} = R_2/R_{2o}$.

The subscript o represents the subscripted quantity for spherical shape. We can now proceed to develop expressions for the kinetic and potential energies.

The moment of inertia of each ellipsoid (whether oblate or prolate) is (Pe 74, p. 80).

$$I_j = D\frac{4}{15}\pi R_j b_j^2(b_j^2 + R_j^2)$$

where D is the uniform density. The major and minor semi-axes are related by the constraint of constant volume:

spherical volume = $V_j = \frac{4}{3}\pi\ b_j^2 R_j$ = ellipsoidal volume.

So $b_j^{\,2} = \frac{3V_j}{4\pi R_j} = \frac{R_{jo}^3}{R_j}$

which results in

$$I_j = \frac{1}{5}\, DV_j R_j^{\,2} \left[1 + \left(\frac{R_{jo}}{R_j}\right)^3\right]$$

or

$$I_j = \frac{1}{5}\, M_j R_j^{\,2} \left[1 + \frac{1}{\rho^3}\right] = \frac{1}{2}\,\rho^2 \left(1 + \frac{1}{\rho^3}\right) I_{jo} \qquad (1)$$

where $$I_{jo} = \frac{2}{5}\, M_j R_{jo}^2 \quad .$$

The relative moment of inertia is

$$I_r = M(R_1 + R_2)^2 = \rho^2 M(R_{1o} + R_{2o})^2 = \rho^2 I_{ro} \quad . \qquad (2)$$

The total moment of inertia can be written explicitly in terms of ρ as $I = I_1 + I_2 + I_r$

$$= \frac{1}{2}\,\rho^2 (1 + \frac{1}{\rho^3})(I_{1o} + I_{2o}) + \rho^2 I_{ro}$$

$$= \frac{1}{2}\,\rho^2 (\frac{1}{\rho^3} - 1)\ (I_{1o} + I_{2o}) + \rho^2\ I_o$$

$$= \rho^2 I_o \left[\frac{1}{2}\,(\frac{1}{\rho^3} - 1)\ \frac{I_{1o} + I_{2o}}{I_o} + 1\right] = I_o F(\rho) \qquad (3)$$

which defines $F(\rho)$.

The total rotational energy is

$$E_r = \frac{\hbar^2 L^2}{2I} = \frac{\hbar^2 L^2}{2 I_o F(\rho)} = \frac{E_{ro}}{F(\rho)} \qquad (4)$$

Employing the assumption of rigid sticking rotation, the total angular momentum is related to the angular frequency ω, as $L = Iw = (I_1 + I_2 + I_r)\, w$ from which we see that the orbital angular momentum is

$$\ell = I_r w = \frac{I_r}{I} L = \frac{\rho^2 I_{ro} L}{F(\rho) I_o} = \frac{\rho^2}{F(\rho)} \ell_o \quad . \qquad (5)$$

The orbital rotational energy is

$$E_{orb} = \frac{\hbar^2 \ell^2}{2\, I_r} = \frac{1}{2} \frac{\rho^2}{F(\rho)^2} \frac{I_{ro}}{I_o^2} \hbar^2 L^2 = \frac{\rho^2}{F(\rho)^2} E_{orb,o} \qquad (6)$$

The surface energy of each fragment is calculated as $E_{sj} = e_s S_j$ where e_s is the surface energy per unit area of a spherical nucleus and equals 0.801 $\frac{\text{MeV}}{\text{fm}^2}$ and S_j is the ellipsoidal surface area of fragment j. The surface area of a prolate ellipsoid is (Ho 46, p. 246)

$$S_j = 2\pi b_j^2 + \frac{2\pi}{\varepsilon} R_j b_j \sin^{-1}\varepsilon$$

where ε = eccentricity of the ellipse $= \sqrt{\frac{R_j^2 - b_j^2}{R_j}} = \sqrt{1 - \frac{1}{\rho^3}}$

In terms of ρ , the surface area is

$$S_j = S_{jo}\left[\frac{1}{2\rho} + \frac{\rho^2}{2\sqrt{\rho^3-1}}\sin^{-1}\sqrt{1-\frac{1}{\rho^3}}\right] = S_{jo}\,G_p(\rho) \tag{7}$$

where $S_{jo} = 4\pi R_{jo}^2$, and which defines $G_p(\rho)$.

The surface area of an oblate ellipsoid is (Ho 46, p. 264)

$$S_j = 2\pi b_j^2 + \frac{\pi R_j^2}{\varepsilon}\ln\frac{1+\varepsilon}{1-\varepsilon}$$

where ε = eccentricity of the ellipse = $\dfrac{\sqrt{b_j^2 - R_j^2}}{b_j} = \sqrt{1-\rho^3}$.

In terms of ρ, the surface area is

$$S_j = S_{jo}\left[\frac{1}{2\rho} + \frac{1}{4}\frac{\rho}{\sqrt{1-\rho^3}}\ln\left(\frac{1+\sqrt{1-\rho^3}}{1-\sqrt{1-\rho^3}}\right)\right] = S_{jo}\,G_o(\rho) \tag{8}$$

which defines $G_o(\rho)$. The Surface energy for both ellipsoids is

$$E_s(\rho) = e_s(S_{1o} + S_{2o})\,G_x\,(\rho) = E_{so}\,G_x(\rho),\quad x = p \text{ or } o\quad . \tag{9}$$

The exact Coulomb interaction between collinear ellipsoids is expressed by the following equation (Qu 69)

$$E_c(\rho) = \frac{1.44\,Z_1Z_2}{R_1+R_2}\cdot\frac{3}{40}\left\{\frac{1}{x_1^2\,x_2^2}(1 + 11\,x_1^2 + 11\,x_2^2) + \frac{1}{4}\left[F(x_1,x_2) + F(-x_1,x_2) + F(x_1,-x_2) + F(-x_1,-x_2)\right]\right\} = E_{co}W(x_1,x_2) \tag{10}$$

which defines $W(x_1,x_2)$ and

where $x_i^2 = \frac{R_i^2 - b_i^2}{(R_1+R_2)^2} = \frac{\rho^3-1}{\rho^3}\,\frac{R_i^2}{(R_1+R_2)^2}$, $i = 1,2$

and $F(x_1,x_2) = \frac{(1+x_1+x_2)^3}{x_1^3\ x_2^3}\ (1 - 3(x_1+x_2)+12\ x_1x_2 - 4(x_1^2+x_2^2\ )\ln(1+x_1+x_2)$

and E_{co} = monopole component of the interaction $\frac{1.44\ Z_1Z_2}{R_1+R_2}$ MeV .

Equation (10) is a real function when both ellipsoids are prolate. When either or both are oblate, Eq. (10) is a complex function, in which case only the real part is of physical interest. This has been checked by comparing the real part of Eq. (10), for complex x_1 and x_2, with the multipole expansion given by Cohen and Swiatecki (Co 62, p. 167).

The self Coulomb energy of two spherical nuclei is

$$E_{sco} = 0.710\left(\frac{Z_1^2}{A_1^{1/3}} + \frac{Z_2^2}{A_2^{1/3}}\right)\text{MeV}.$$

When they are prolate the self Coulomb energy is

$$E_{sc}(\rho) = E_{sco}\,\frac{1}{2}\,(1-\varepsilon^2)^{1/3}\ \frac{1}{\varepsilon}\,\ln\frac{1+\varepsilon}{1-\varepsilon} = E_{sco}K_p(\rho) \tag{11}$$

where ε = eccentricity of the ellipse = $\sqrt{1 - \frac{1}{\rho^3}}$.

When they are oblate the self Coulomb energy is

$$E_{sc}(\rho) = E_{sco}\ (1+y^2)^{1/3}\ \frac{1}{y}\ \tan^{-1}y = E_{sco}K_o(\rho) \tag{12}$$

where $y^2 = \frac{1}{\rho^2} - 1$ (this is not the eccentricity of the ellipse). So in general, the self Coulomb energy of two ellipsoids is

$$E_{sc}(\rho) = E_{sco}\, K_x(\rho) \quad , \; x = p \text{ or } o \; . \tag{13}$$

2. Evaporation Recoil Energy

We begin by considering the frame of reference in which the parent fragment is at rest before evaporation begins. The fragment's momentum, $\vec{P}_n$, when all evaporation has been completed (N steps) can be written as the vectorial sum of the momentum of each emitted particle, $\vec{P}_i$.

$$\vec{P}_n = \sum_{i=1}^{N} \vec{P}_i \; .$$

Squaring both sides yields

$$P_n^{\,2} = \sum_{i=1}^{N} P_i^{\,2} + 2 \sum_{i=1}^{N} \; \sum_{j=i+1}^{N} \vec{P}_i \cdot \vec{P}_j$$

$$= \sum_{i=1}^{N} P_i^2 + 2 \sum_{i=1}^{N} \; \sum_{j=i+1}^{N} P_i P_j \cos\Theta_{ij} \tag{14}$$

where Θ_{ij} is the angle between the i^{th} and j^{th} particle directions. We shall assume that there is no correlation between the direction of emission of the particles, and that this emission is isotropic. This means that $\cos\Theta_{ij}$ varies randomly between -1 and +1. When we average Eq. (14) over many events, the double sum vanishes, and we find

$$\langle p_n^2 \rangle = \sum_{i=1}^{N} \langle p_i^2 \rangle \tag{15}$$

This means that the mean square momentum of the recoiling fragment, in the pre-emission fragment frame of reference, equals the sum of the mean square momenta of the particles it emitted. The average momentum of the emitted particles decreases along the decay chain, because the temperature is reduced by the evaporation. The mean square momentum along the decay chain is defined as

$$p_a^2 = \frac{1}{N} \sum_{i=1}^{N} \langle p_i^2 \rangle$$

So the root mean square (RMS) fragment momentum is related to the RMS particle momentum as

$$p_r \equiv \sqrt{\langle p_n^2 \rangle} = \sqrt{N}\, p_a \quad , \tag{16}$$

The pre-emission velocity of the parent fragment is $\vec{v}_o$, its post-emission velocity is $\vec{v}_f$ and its recoil velocity in the pre-emission frame of reference is $\vec{v}_r = \vec{p}_r/M_f$, where M_f is the post-emission fragment mass. These three velocities are related vectorially:

$$\vec{v}_f = \vec{v}_o + \vec{v}_r \tag{17}$$

The post-emission center of mass (CM) energy of the fragment is

$$E_f = \frac{1}{2} M_f\, v_f^2 = \frac{1}{2} M_f [\, v_o^2 + 2\vec{v}_o \cdot \vec{v}_r + v_r^2 \,]$$

So the post-emission energy can be written explicitly as a function of the net recoil angle, Θ_e, with respect to the pre-emission direction of the fragment:

$$E_f(\Theta_e) = \frac{M_f}{M_o} E_o + \frac{NM_n}{M_f} E_n + 2\sqrt{\frac{NM_n}{M_o} E_o E_n} \cos\Theta_e \tag{18}$$

where $E_o = \frac{1}{2} M_o v_o^2$ = pre-emission fragment energy in the CM.

M_n = neutron mass.

E = mean energy of the emitted particle = $\frac{P_a^2}{2M_n}$.

M_o = pre-emission fragment mass.

Let us define the evaporated mass fraction as $n = \frac{NM_n}{M_o}$. Then Eq. (18) can be written as

$$E_f(\Theta_e) = (1-n)E_o + \frac{n}{1-n} E_n + 2\sqrt{nE_oE_n} \cos\Theta_e \tag{19}$$

The distribution of recoil directions of the parent fragment with respect to its pre-emission direction is isotropic, because the particle emission directions are random and isotropic. This means that the probability of recoil at angle Θ_e is

$$P(\Theta_e) = \frac{2\pi \sin\Theta}{4\pi}$$

So we can calculate the moments of the final kinetic energy over all possible recoil angles. This first moment is

$$
\begin{aligned}
\langle E_f \rangle &= \frac{1}{2}\int_0^{\pi} E_f(\Theta)\ \sin\Theta\ d\Theta \\
&= (1-n)E_o + \frac{n}{1-n} E_n
\end{aligned}
\qquad (20)
$$

The standard deviation is

$$
\begin{aligned}
\sigma_{E_f} &= \left[\langle E_f^2 \rangle - \langle E_f \rangle^2\right]^{\frac{1}{2}} \\
&= 2\sqrt{\frac{1}{3} n E_o E_n}
\end{aligned}
\qquad (21)
$$

3. Moments of Evaporation Recoil Energy for a Finite Detector

We can calculate the moments of the kinetic energy due to evaporation as

$$
\langle E^n \rangle = \frac{\displaystyle\int_0^{\phi_{max}} 2\pi\sin\phi \left[\int_{\Theta_{f,min}}^{\Theta_{f,max}} E(\Theta_f)^n f(\Theta_f)\alpha(\Theta_f)d\Theta_f\right] d\phi}{\displaystyle\int_0^{\phi_{max}} 2\pi\sin\phi \left[\int_{\theta_{f,min}}^{\Theta_{f,max}} f(\Theta_f)\alpha(\Theta_f)d\Theta_f\right] d\phi} \qquad (22)
$$

where (refer to Fig. 42):

ϕ = angle from the center of the detector to pre-emission direction of the fragment.

Θ_f = CM angular deflection of the fragment from its pre-emission direction.

ϕ_{max} = half-angular acceptance (in the CM) of the detector, Θ_a, plus the maximum deflection of the fragment.

$E(\Theta_f)$ = CM energy of the fragment.

$f(\Theta_f)$ = probability of deflection by Θ_f radians = $\frac{2\pi\sin\Theta_f}{4\pi}$

$a(\Theta_f)$ = probability of a particle, deflected by Θ_f, reaching the detector. See Fig. 42 and the discussion further on.

The vectorial relation between $\vec{v}_f$, $\vec{v}_o$ and $\vec{v}_r$ -- Eq. (17) -- leads to the following relation between the CM deflection angle, Θ_f, and the recoil angle in the fragment's pre-emission frame of reference, Θ_e:

$$\sin\Theta_f = \frac{v_r}{v_f}\sin\Theta_e$$

$$= \frac{J\sin\Theta_e}{[1+J^2+2J\cos\Theta_e]^{1/2}} \qquad (23)$$

where $J = \sqrt{\frac{n E_n}{(1-n)^2 E_o}}$

With the typical values used earlier, we see that J = 0.0384, giving a maximum deflection (at Θ_e = 90°) of 2.2 degrees.

We can invert Eq. (23) to give Θ_e as a function of Θ_f:

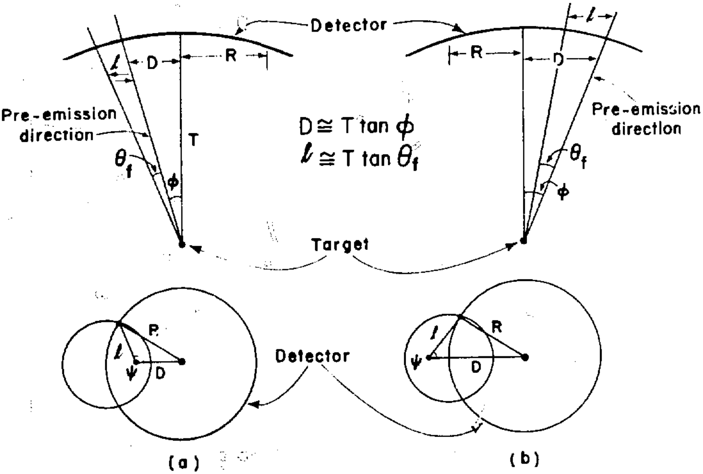

XBL 782 136

Fig. 42 Explanation of angles used in Eq. (22) for Appendix I.3. In Fig. (a) the pre-emission direction of the fragment is within the area subtended by the detector window. The particle remains within the detector cone after evaporative deflection by Θ_f degrees. In Fig. (b) the pre-emission direction is outside the area of the window and the particle is deflected into the detector.

$$\cos\Theta_c = -\frac{\sin^2\Theta_f}{J} \pm \left[\frac{\sin^4\Theta_f}{J^2} - \frac{1+J^2}{J^2}\sin^2\Theta_f + 1\right]^{1/2} \tag{24}$$

This equation, with Eq. (18), allows us to calculate the CM energy as a function of CM deflection angle Θ_f.

Figure 42 explains the derivation of $\alpha(\Theta_f)$. Figure 42(a) depicts the situation in which the initial particle direction is within the solid angle subtended by the detector. In this case the range of Θ_f values which reach the detector is between 0 and $\phi + \Theta_a$. In Fig. 42(b) the initial particle direction is outside the solid angle of the detector. In this case the range of Θ_f values which reach the detector is between $\phi - \Theta_a$ and $\phi + \Theta_a$. In terms of the quantities defined in Fig. 42,

$$\alpha(\Theta_f) = \begin{cases} 1, \text{ if } D \leq R \text{ and } \ell < R-D \\ \frac{2\psi}{2\pi} \text{ otherwise} \end{cases} \tag{25}$$

$$\cos\psi = \frac{\tan^2\phi + \tan^2\Theta_f - \Theta_a^2}{2\tan\phi\,\tan\Theta_f} \tag{26}$$

where Θ_a is in radians.

B. Appendix II. Calibration of the Pulse Height Defect in Solid State Detectors

1. Introduction

As the capability of heavy ion accelerators expands to include heavier and heavier nuclei at ever greater energies, a greater need develops for accurate calibration of the energy and mass non-linearity of solid state detectors. These non-linearities are defined relative to the detector response to alpha particles. In general terms, the pulse height defect (PHD) is the difference between the detector response to a heavy ion and to an alpha particle of the same energy. (A more precise definition will be given later). The PHD for a given incident energy increases markedly with mass. For 100 MeV projectiles, the PHD is roughly 0.6% of the ion energy for Ne, 3% for Ar, 8% for Kr, 12% for Xe, and 20% for Au. The PHD also increases in magnitude with ion energy, being about 2 MeV for Kr at 10 MeV incident energy and 8 MeV for 100 MeV Kr.

Extensive work on the physical basis of the PHD has identified the major contributing factors. These factors can be grouped into four categories: 1) loss of free electrons by recombination of ion pairs; 2) loss of energy in low-energy non-ionizing collisions with lattice atoms, leading to phonon excitations; 3) loss of energy in the Au entrance window and underlying surface dead layer (when it exists); and 4) loss of free electrons at "trapping sites" such as lattice defects or impurities. (Ax 65, Kr 67, Ko 65, Ei 67, Fo 67, Wi 71, St 72, Fi 73).

Identification of the factors contributing to the PHD has been accompanied by attempts to reproduce each factor with model calculations

(St 72, Li 63, Ha 66, Fi 73a). However, the most widely used techniques (Ka 74, Sc 65) for reproducing measured values and estimating corrections due to the PHD have been strictly empirical formulae which lump all contributing factors into one or several parameters. Schmitt and co-workers (Sc 65) developed a widely used 4-parameter calibration equation relating the true energy to the observed pulse height. Like most other efforts of that time, the procedure was based on measuring the energy centroids of the low- and high-mass fission peaks of ^{252}Cf. (Thermal-neutron fission of ^{235}U has also been used (Fi 73). Subsequently, Kaufman et al. (Ka 74), utilizing beams from a Van de Graaff to recoil-scatter heavy target nuclei into a Si counter, developed an empirical 1-parameter formula which fit data measured between 4.5 and 80 MeV. More recently, Finch et al. (Fi 77) have used a mass separator with unit mass resolution to study the PHD of fission fragments having masses between 85-105 and 130-140 amu and energies up to 100 MeV. A major limitation of the above approaches is imposed by the limited range of ion energies, and masses available from fission (Sc 65, Fi 77, Br 64) and the restricted energy range of Tandem Van de Graafs (Wi 71, St 72, Ka 74).

In the present (Mo 78) work we present PHD measurements made at Lawrence Berkeley Laboratory's 88-Inch Cyclotron. These measurements cover a larger mass and energy range than previously reported work, and use a direct irradiation technique which avoids some errors inherent in recoil scatter measurements and which provides fragments with unit atomic number and mass resolution. The experimental technique is is described in section 2. In section 3 we discuss a simple, accurate power-law formula for representing the measurements, and a reliable method of deducing calibrations for a large number of elements from the measurement of the PHD for just a few. Finally, in section 4 a comparison is made with the calibration technique of Kaufman et al. (Ka 74).

2. Experimental Procedure

Recent use of the Berkeley 88-Inch cyclotron as a mass spectrometer for trace heavy-element detection (St 78), radio-isotope dating (Mu 77) and quark searches (Mu 77a) led to the present use of direct cyclotron beams for PHD calibrations. Since it is a source of projectiles of any stable isotope, over a large energy range, the cyclotron is an extremely useful tool for PHD determinations. The energy range is limited at the upper end primarily by the maximum charge state which the ion source can produce, and at the lower end by the ability of the machine to accelerate particles on high harmonics of the lowest cyclotron frequencies. (The harmonic on which a particle is accelerated is defined as the ratio of the oscillation frequency of the cyclotron's electric field to the frequency of revolution of the particle in its orbital motion within the machine.) Charge states of Au from 6+ to 14+ were extracted from the ion source, and accelerated to energies ranging from about 25 to 140 MeV. Since the cyclotron beam energies are known quite accurately (± 0.5% is an upper limit of the absolute error) the degree of accuracy required for PHD measurements is routinely achieved. Extremely low intensities of essentially DC beam can be reliably obtained, permitting direct irradiation of the sample detectors without danger of detector damage. The corrections inherent in scattered-beam experiments (corrections due to uncertainties in the laboratory scattering angle, detector angular acceptance and target thickness) are completely avoided.

In this work, a Penning Ion Gauge (PIG) source was fed with a mixture of noble gases (Ne, Ar, Kr, Xe). In addition, either Au or a combination of rare earths were mixed with Ta and used in the ion source as a mixed pellet at the edge of the ion discharge, opposite the anode opening. In this way many charge states of elements over a large mass range were produced by the ion source and injected into the cyclotron. Tuning of the cyclotron frequency, the dee voltage and electrostatic deflector voltages allowed quick selection of a particular isotope and charge state. Low intensity beams of 45 different ions were accelerated and extracted from the cyclotron during a typical 16 hour run. An old, expendable "search" detector was used to monitor the beam intensity before exposing the detector to be calibrated, to prevent damage to this detector by an excessive beam current. Sometimes slight frequency de-tuning was necessary to lower the beam intensity to acceptable levels. Typical beam currents ranged from ten's to thousand's of particles per second impinging on the detector. Ion energies from 5 to 160 MeV were achieved, without exhausting the potential of the machine.

Since the cyclotron can be tuned very precisely to select one value of the charge-to-mass ratio, it provides just one specific isotope at a time to the experimental area in nearly all cases. The extremely low backgrounds obtained for several Au beams are illustrated in Fig. 43.

Fig. 43 Pulse height spectrum of counts vs. energy for Au^{7+}, Au^{9+}, Au^{11+}, and Au^{13+} beams. Note the near absence of background events.

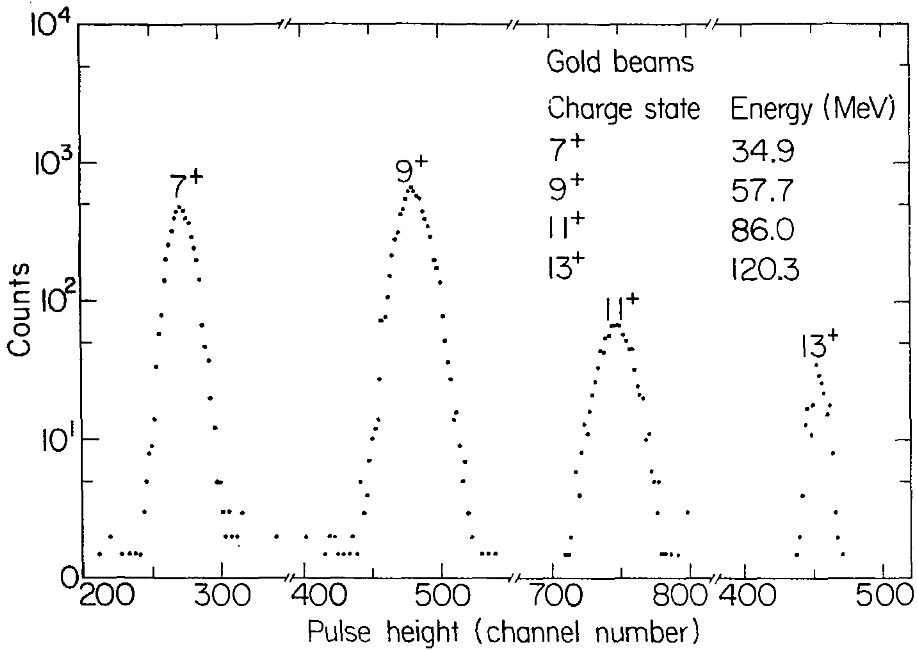

XBL 7710-2090

The ability to readily provide monoisotopic and monoenergetic beams over a broad energy and mass range makes a cyclotron a superb tool for investigating the mass, charge and energy dependence of the PHD.

Because the cyclotron parameters are known for each ion, and because no intermediate scattering in a target occurs, the true energy incident at the detector is known very accurately. The particle energy is related to its charge Q, mass M, the magnetic field B and the cyclotron radius R by the uniform field cyclotron equation: $E = Q^2B^2R^2/2M$. Because the magnetic field varies azimuthally, the product $B \cdot R$ is determined empirically for a given setting of the main field and trim coil magnet currents. The same magnetic field was used in accelerating all the beams of one run. The absolute energy scale was determined from parameter systematics of the cyclotron (Hi 69, Ba 72). The value of the ion charge and mass were determined unequivocally in nearly all cases from knowledge of the exact cyclotron frequency and the approximate ion energy as described more fully elsewhere (St 78).

The pulse height response of the detector to alpha particles was measured using a thin ^{212}Pb source, which emits two alpha particles of substantially different energies in its decay chain. This calibration was extrapolated to higher energies using a mercury pulser. The alpha particle calibration defines an "alpha energy", E_α, for the centroid of each spectrum. The true total energy, E_T, minus the energy loss E_w of the heavy ion in the detector window, yields the "deposited energy", E_d. The PHD is then defined as the difference between the deposited energy and the alpha energy:

$$PHD = (E_1 - E_W) - E_\alpha = E_d - E_\alpha \tag{1}$$

It should be noted that this definition of the PHD differs from that used by some other workers (e.g. ref. Ka 74) by excluding the energy loss in the detector surface dead layer from the PHD. Because the surface dead layer thickness can be measured without great difficulty, and since it varies from one detector type to another, it seems better to treat it separately in a general method for calibrating the PHD.

The experiments reported on in this work were performed with a single heavy ion Si surface barrier detector (ORTEC 15-016C) of 300 μm depletion depth and 1000 Ω-cm resistivity which was operated at its specified bias voltage of 150 volts. The variation of the PHD with detector type has been previously investigated extensively (Wi 71, St 72, Ka 74), and due to machine time constraints we have chosen to extensively study one detector rather than to perform a more limited study of many different detectors and detector types. The thickness of the Au window of the detector was checked by an X-ray fluorescence measurement, which agreed to within 10% with the thickness of 39.7 μg/cm^2 specified by the manufacturer. The effective surface dead layer of the detector was inferred from data obtained by irradiation with a 14.0 MeV $^{40}Ar^{2+}$ beam incident at three different angles to the surface: 90°, 45° and 30°. The shift in the energy centroid with angle was somewhat greater than expected from the Au window alone. Since in the X-ray fluorescence measurement no peaks were observed for elements other than Au and Si, we assumed an additional thin Si dead layer (16.3 μg/cm^2) beneath the Au window whose thickness was calculated using standard range-energy tables (No 70). Such an additional dead layer may be due to any of several factors: a thin undepleted surface region, an oxygen impurity at the surface which acts as an electron acceptor, charge diffusion against the electric field gradient, or prior use of the detector with heavy ions (Ca 70). It should be noted, however, that the measured FWHM of 45 keV for 8.785 MeV alpha particles indicates good bulk collection properties.

The "search" and "data" detectors were mounted on a rotating platform and moved successively into the axis of each beam. Pulses from each were amplified first by a charge sensitive preamplifier, then by a double delay line amplifier, and were digitized by a 4096 channel analogue-to-digital converter, and written on magnetic tape with the aid of a computer.

The accuracy of the PHD data is limited by the accuracy to which three different quantities can be measured or calculated: the total ion energy E_T, the "alpha energy" E_α, and the energy loss in the surface dead layer E_W. Experience with measuring the absolute energies of beams from the 88-Inch cyclotron using a magnetic analysis system (Go 78) has led to an upper limit on the error of E_T of ±0.5%. The accuracy of E_α depends on the measurement of the energy centroids of the two alpha particle peaks and the extrapolation to higher energies with a linear pulser. The error in this extrapolation has been estimated to be ± 0.36% of E_α. The error of E_W arises from the uncertainties in the dead layer thickness and in the range-energy relations (No 70). The error of E_W has been estimated as ± 2.5% of E_W based on the reproducibility of the dead layer measurements. The window correction is comparable to the PHD only for lighter masses, and in all cases makes only a negligible contribution to the PHD error. The net uncertainty in the PHD is less than the size of the data points shown in Fig. 44.

3. Results and Discussion

PHDs have been measured for elements ranging from Ne to Au, for energies from about 5 to 160 MeV. The PHD data for one counter is shown in Fig. 44 in MeV units and log-log format. Two important features should be noticed: the PHD is linear with E_d for each element, and different elements lie on different lines. The four solid lines represent linear least-square fits to the Au, Ta, Xe and Kr data. The good agreement with the data reveals the utility of a simple power-law fitting function:

$$\mathrm{PHD} = 10^{b}\, E_d^{\,a} \tag{2}$$

where a is the slope and b is the y-intercept of a plot of log PHD versus log E_d. The fitted slopes and y-intercepts for these four elements are given in Table A1. Both the slopes and the intercepts increase with atomic number (Z) and a typical value for the slope is 0.6.

Since the data for each element cluster on separate lines, it is desirable to have a procedure for mathematically generating calibration lines for all elements from lines measured for just a few. This has been done by fitting the slope and intercept parameters of Eq. (2) to simple functions of the atomic number (Z) and mass number (A). Figure 45

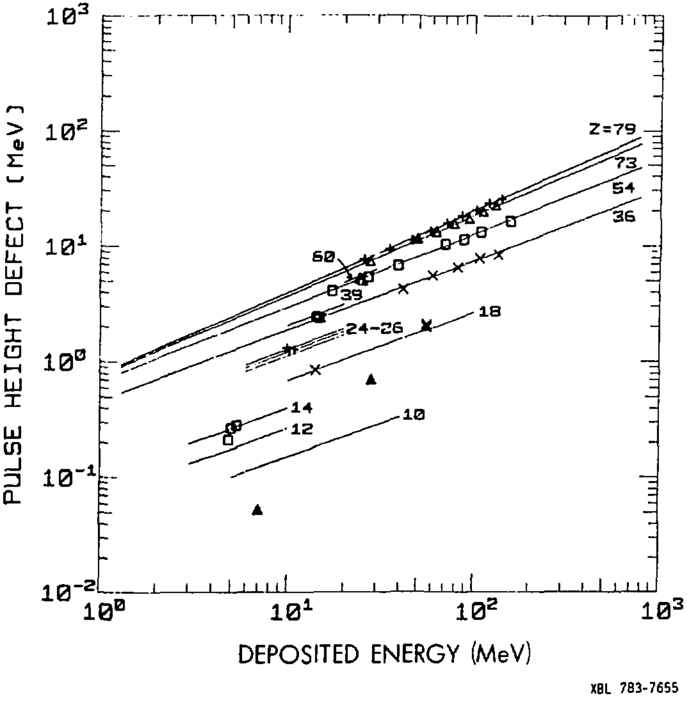

Fig. 44 PHD of a silicon surface barrier detector vs. deposited energy. The PHD is defined to exclude the energy loss in the surface window (see text). Long lines are linear least-square fits to the data with equal weights: short lines are extrapolations using method described in the text. Errors are less than the size of the data points, (See discussion in text).

TABLE A1. Measured coefficients for PHD calibration lines.

Isotope	a	b
$^{197}_{79}Au$	0.7060	-0.1036
$^{181}_{73}Ta$	0.6902	-0.1057
$^{129}_{54}Xe$	0.6295	-0.1538
$^{84}_{36}Kr$	0.5990	-0.3227

shows linear fits of the slope, a, to the square of Z and A for the Au, Ta, Xe and Kr data shown in Fig. 44. The fitting functions are:

$$a(Z) = 0.02230 \left(\frac{Z^2}{10^3}\right) + 0.5682 \tag{3}$$

$$a(A) = 0.03486 \left(\frac{A^2}{10^4}\right) + 0.5728 \quad . \tag{4}$$

Using one of these correlations for the a parameter, a value of the intercept, b, can be calculated from the measured PHD and the deposited energy (E_d) according to the following equation:

$$b = \log \left(\frac{\mathrm{PHD}}{E_d{}^a}\right) \quad . \tag{5}$$

Values for -b based on Eqs. (3) and (5) and the data of Fig. 44 are shown in Fig. 46 plotted versus 100/Z and 100/A. Equivalent results can be obtained using Eq. (4) instead of Eq. (3). With the exception of the lightest elements (Ne and Mg), where the PHD is very small and the percent error is large, the calculated intercepts are accurately represented by a straight line. The fitting equations are

$$b(Z) = -0.1425 \left(\frac{100}{Z}\right) + 0.0825 \tag{6}$$

$$b(A) = -0.2840 \left(\frac{100}{A}\right) + 0.0381 \quad . \tag{7}$$

The slope and the intercept calculated from Eqs. (3) or (4) and (6) or (7) can be used in Eq. (2) to compute the PHD for any element.

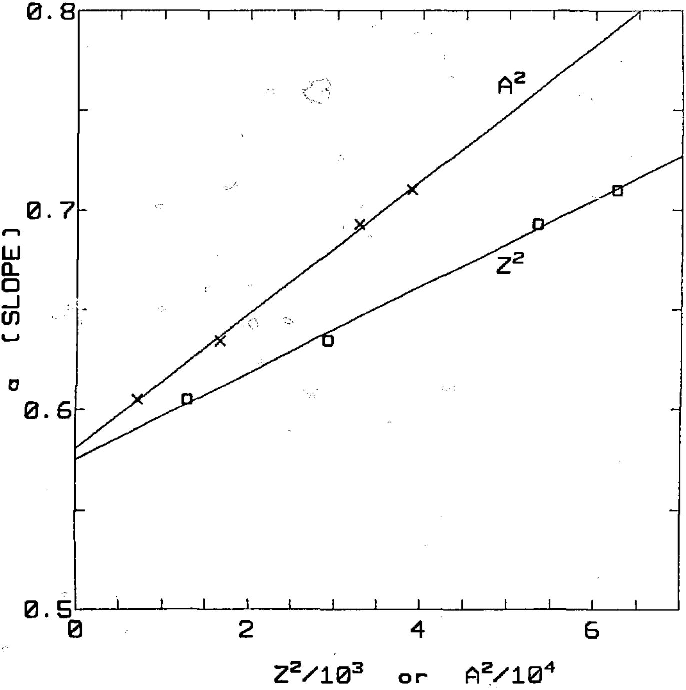

XBL 783-7427

Fig. 45 Measured values of the parameter a (of Eq. (2) of Appendix II) for Au, Ta, Xe and Kr, plotted versus Z^2 and A^2. Lines are linear least-square fits to the data with equal weights.

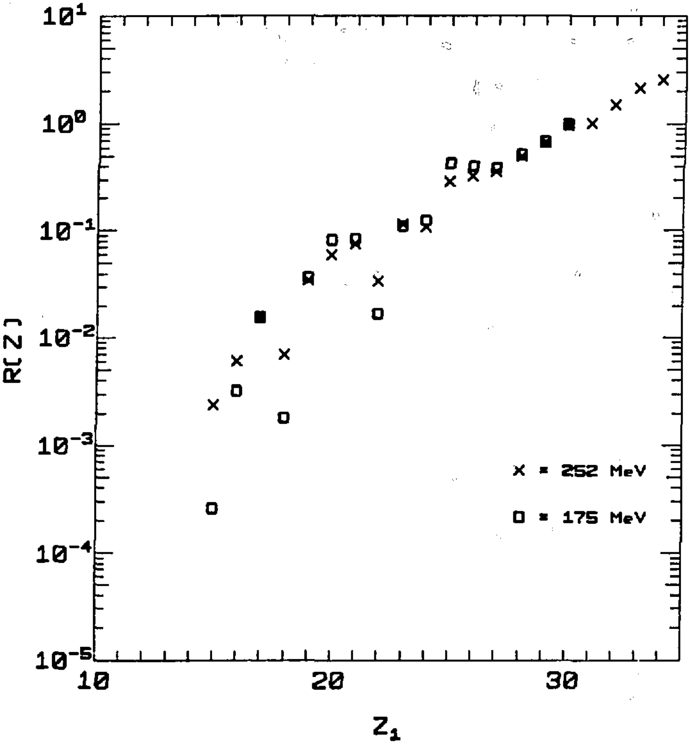

XBL 783-7429

Fig. 29 R(Z) versus the atomic number of the light fragment. See text.

As a test of the scheme, the PHD lines were calculated from Eq. (2) for the remaining elements in Fig. 44. The slope and intercept were calculated from Eqs. (3) and (6). The results, shown by the dashed lines in Fig. 40, provide good agreement with the observed PHD. This calibration scheme is valid for elements from Ne to Au and energies from 5 to 160 MeV.

Computed PHDs from Eqs. (3) and (6) have been displayed in several ways to facilitate their use by other scientists. The range of applicability of these results will be discussed later. Figure 47 displays calculated PHD versus deposited energy calibration lines for a range of elements from Ne to U. These lines are useful for a quick assessment of the PHD to be expected in a particular experimental situation. It is also useful to plot the PHD versus the alpha energy, since this is an observable quantity. Equations (1) and (2) can be combined to write the alpha energy in terms of the total energy as

$$E_\alpha = E_d(1 - 10^b E_d{}^{a-1}) \tag{8}$$

Equations (2) and (8) allow one to uniquely generate the curves in Fig. 48, which relate the PHD to the alpha energy. With these curves one can find the PHD directly from the alpha energy. It is useful to notice that these curves are quite nearly linear over a large energy range, and could be parameterized easily.

The effect of atomic mass on the PHD of four Xe isotopes at 130 MeV has been measured; however the data is too limited to understand the systematics of the PHD with atomic mass. The standard deviation of the PHD for isotopes 128,130,131, and 132 is 0.25 MeV, which is

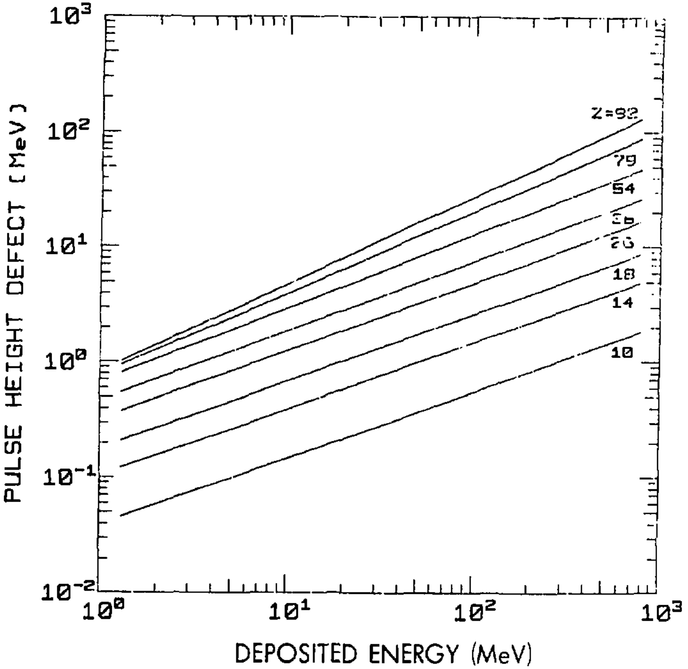

XBL 783-7654

Fig. 47 Computed PHD vs. the deposited energy. Lines generated by the procedure described in text. Range of reliability discussed in the text.

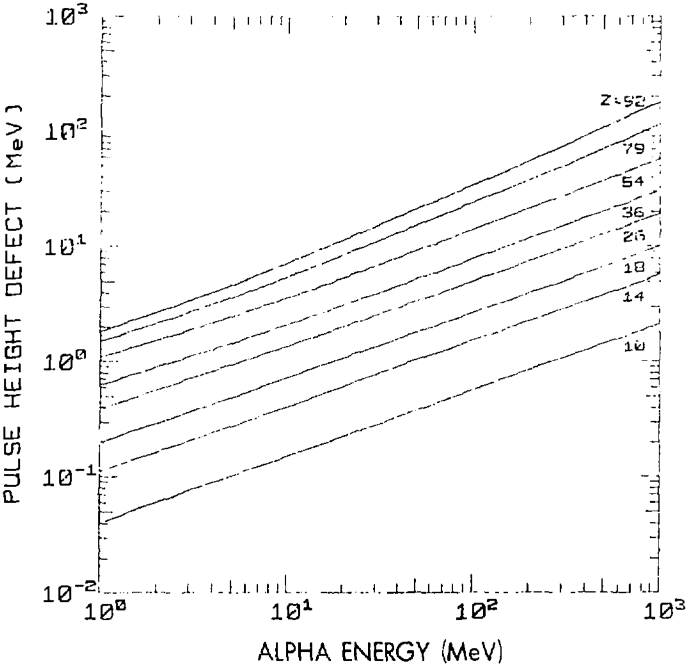

XBL 783-7653

Fig. 48 Computed PHD vs. the alpha energy. See Fig. 47 and text.

within the estimated error of measurement. Thus the isotopic effect seems to be smaller than the effect arising from the same fractional change of Z.

Comparison of our PHD predictions with data from Wilkins, et al. (Wi 71) in Fig. 49 indicates generally good agreement (6-10% of the PHD), even though the resistivity of their detector is 380 ohm-cm (our detector had a resistivity of 1000 ohm-cm). Their data overlap somewhat with the low-energy range of ours. In Fig. 49, data (adapted from Tables 2, 3 and 4 of Wi 71) for three elements (Au, Ag and Cu) are compared with our PHD calibration lines for the same elements. The Au line is a fit to our measured data, and the Ag and Cu lines are calculated with our calibration procedure. In this comparison the energy loss in the detector surface window has been subtracted from their tabulated PHD values, in accordance with our definition. This is evidence that the application of our calculated PHD lines to other detectors of similar type is probably reliable to better than 10% of the PHD.

4. Comparison with the Kaufman Calibration Procedure

The PHD of solid state detectors has been previously studied by Kaufman and his associates (Wi 71, St 72, Ka 74) over an energy range of 4.5 to 80 MeV. They included the energy loss in the detector window as part of the PHD, and fit the energy dependence of the PHD for all elements simultaneously with a 1-parameter formula. This formula relates the PHD, $\Delta\varepsilon$, to the total energy, ε, as

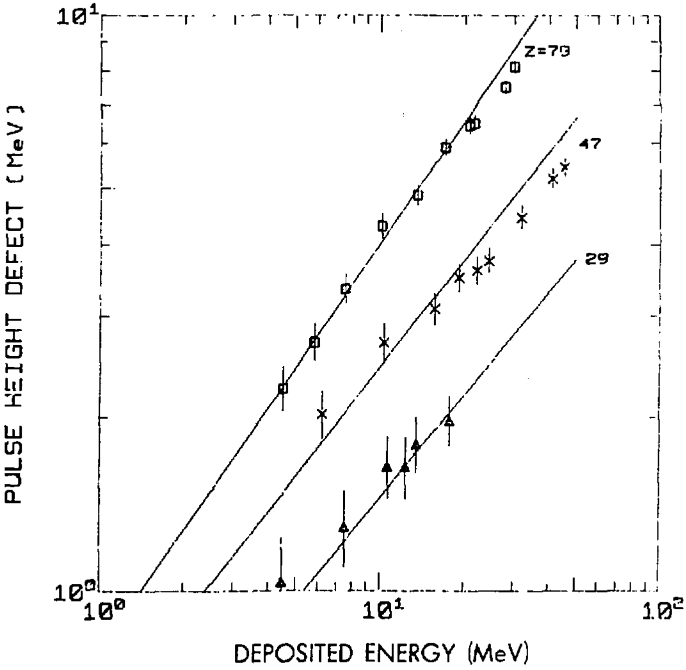

Fig. 49 PHD vs. the deposited energy. Data from Wilkins et al. (Wi 71). Lines generated from data presented in this paper.

$$\Delta\varepsilon = \frac{6\varepsilon}{8+\varepsilon} \frac{A}{1 + 525\varepsilon^{-1.407}} \quad . \tag{9}$$

Both the PHD and the total energy are in LSS units (Li 63). The A-parameter has been observed to vary (Ka 74) by up to 7% from one detector to another (of comparable resistivity, bias voltage, age, etc.) and must be determined by calibration.

To test the PHD scheme of Ka 74, our data have been plotted in Fig. 50 in LSS units and with the window losses included in the PHD (in accordance with the definition of PHD in Wi 71, St 72, and Ka 74.) In the low LSS range one sees the clustering of the measured elements, as observed by Kaufman. In the intermediate and high energy range this clustering clearly breaks down. This failure of our data to cluster on a universal curve in LSS space confirms recent results by Finch et al. (Fi 77) who observed that the PHDs of the light fission fragments fell below the LSS curve on which all of the heavy fission fragment data fell. The same data for Kr, Xe and Au are shown in Fig. 51 along with three curves calculated with Eq. (9) for different values of the A parameter. The divergence of the data from the calculated curves is very apparent in this figure, especially at higher energies. One should note that because of the bending of the curve below the data, extrapolation to high energies with this formula will predict PHDs that are too small. On the other hand, the comparison between the predictions of our PHD calibration scheme and the lower energy data (Wi 71) indicate that our scheme is useful at lower energies as well.

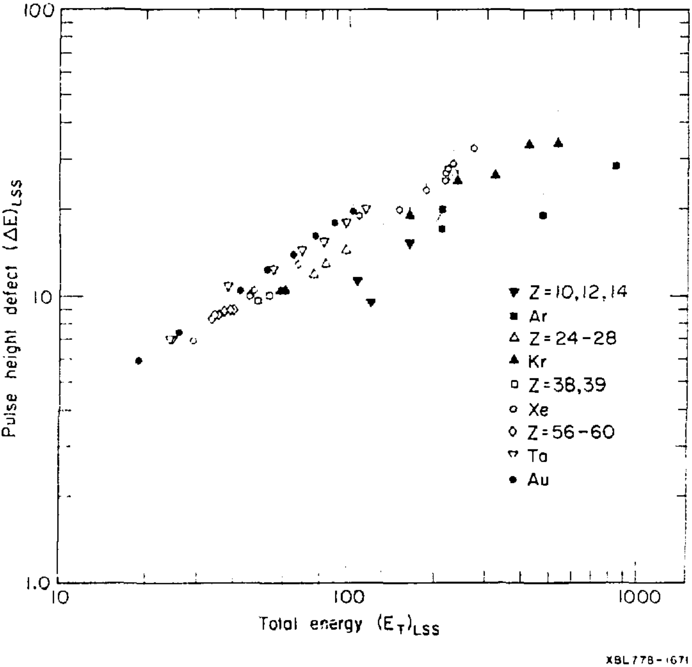

Fig. 50. Measured PHD vs. the total energy in LSS units for several elements. Our PHD data, have been plotted with the energy loss in the surface window included, in accordance with Kaufman's usage (Ka 74).

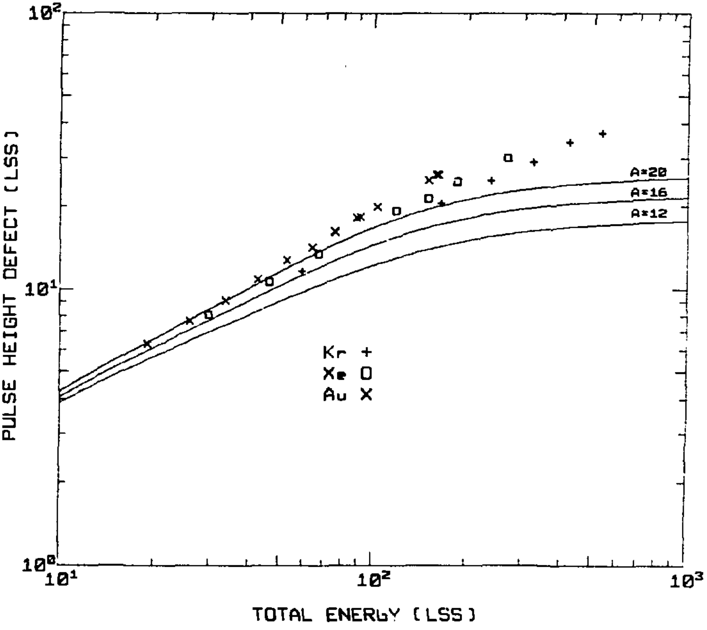

XBL 7710-10309

Fig. 51 Measured PHD vs. total energy in LSS units for three elements. See Fig. 50. Curves calculated with Eq. (9) of Appendix II.

5. Summary

Use of the cyclotron as a source of monoisotopic heavy ion beams of known energy for PHD determinations of solid state detectors has been described. The PHD of an ORTEC surface barrier detector has been measured for elements from Kr to Au, from 15 to 160 MeV and for elements from Ne to Fe between 5 and 50 MeV. The data have been fit with a simple power law formula. A new procedure for generating PHD calibration lines for any element from lines measured for a few elements has been described. The accuracy of this procedure is confirmed to ±0.5% of the total energy, between about 15 and 160 MeV. This accuracy is within the experimental error. Supporting data suggest that the range of reliability extends down to 4.5 MeV. Application of the specific calibration lines presented here, to other detectors with resistivities between several hundred and one thousand Ω-cm is probably accurate to within 10% of the PHD and may be accurate to within a few percent. For energies above 50 MeV, the clustering of the measured PHD values for different elements produced by use of LSS units breaks down. The observed strong dependence of the PHD on atomic number and energy in LSS space limits the usefulness of formulae such as Eq. (9) to estimate PHD data and indicates that the response of a silicon surface barrier detector to heavy ions cannot be accounted for by such a model.

REFERENCES

Al 78 M. M. Aleonard, G. J. Wozniak, P. Glässel, M. A. Deleplanque, R. M. Diamond, L. G. Moretto, R. P. Schmitt and F. S. Stephens, Phys. Rev. Lett., 40 622 (1978).

Ar 00 Aristotle, *Analytical Posterloro*, 87^b 28-39.

Ax 65 R. C. Axtmann and D. Kedem, Nucl. Instr. Meth., 32 70 (1965).

Ba 75 R. Babinet, L. G. Moretto, J. Galin, R. Jared, J. Moulton and S. G. Thompson, Nucl. Phys., A258 172 (1975).

Ba 72 A. D. Bacher, E. A. McClatchie, M. S. Zisman, T. A. Weaver and T. A. Tombrello, Nucl. Phys. A181 453 (1972).

Bl 52 J. M. Blatt and V. F. Weisskopf, *Theoretical Nuclear Physics*, John Wiley and Sons, N.Y., 1952.

Bl 72 M. Blann and F. Plasil, Phys. Rev. Lett., 29 303 (1972).

Br 64 H. C. Britt and G. C. Benson, Rev. Sci. Inst., 35 842 (1964).

Ca 70 J. M. Caywood, C. A. Mead and J. W. Mayer, Nucl. Inst. Meth., 79 329 (1970).

Ca 75 C. Cabot, H. Gouvin, Y. LeBeyec and M. Lefort, J. de Physique, 36 L289-292 (1975).

Ca 78 B. Cauvin, R. P. Schmitt, G. J. Wozniak, P. Glässel, P. Russo, R. C. Jared, J. B. Moulton and L. G. Moretto, Nucl. Phys A294 225 (1978).

Co 62 S. Cohen and W. J. Swiatecki, Ann. Phys. 19 67 (1962).

Co 63 S. Cohen and W. J. Swiatecki, Ann. of Phys. 22 406 (1963).

Eg 76 R. Eggers, M. N. Namboodiri, P. Gonthier, K. Geoffroy and J. B. Natowitz, Phys. Rev. Lett., 37 324 (1976).

Ei 67 P. L. Eisler, Nucl. Inst. Meth., 48 103 (1967).

Er 60 T. Ericson, Adv. in Phys., 9 425 (1960).

Fi 73 E. C. Finch and A. L. Rodgers, Nucl. Instr. Meth., 113 29 (1973).

Fi 73a E. C. Finch, Nucl. Instr. Meth., 113 41 (1973).

Fi 77 E. C. Finch, M. Asghar, M. Forte, G. Siegart, J. Grief, R. Decker and 'Lohengrin' Collaboration, Nucl. Instr. Meth., 142 539 (1977).

Fo 67 V. Forque and S. Kahn, Nucl. Inst. Meth., 48 93 (1967).

Fo 74 M. Fowler and R. C. Jared, Nucl. Instr. Meth., 124 341 (1974).

Ga 74 J. Galin, D. Guerreau, M. Lefort and X. Tarrago, Phys. Rev. C. 9 1018 (1974).

Ga 75 J. Galin, L. G. Moretto, R. Babinet, R. Schmitt, R. Jared, and S. G. Thompson, Nucl. Phys., A255 472 (1975).

Gl 77 P. Glässel, R. S. Simon, R. M. Diamond, R. G. Jared, I. Y. Lee, L. G. Moretto, J. O. Newton, R. Schmitt and F. S. Stephens, Phys. Rev. Lett., 38 331 (1977).

Go 78 R. A. Gough, private communication.

Ha 66 E. L. Haines and A. B. Whitehead, Rev. Sci. Instr. 37 190 (1966).

Hi 69 R. E. Hintz, F. B. Selph, W. S. Flood, B. G. Harvey, F. G. Resmini and E. A. McClatchie, Nucl. Instr. Meth., 72 61 (1969).

Ho 46 C. D. Hodgman, Handbook of Chemistry and Physics, Chemical Rubber Co., Cleveland, 1946.

Ka 74 S. B. Kaufman, E. P. Steinberg, B. D. Wilkins, J. Unik and A. J. Gorski, Nucl. Inst. Meth., 115 47 (1974).

Ke 62 E. L. Kelley, Nucl. Instr. Meth., 18, 19 33 (1962).

Ko 65 E. Konecny and K. Hetwer, Nucl. Inst. Meth., 36 61 (1965).

Kr 67 A. H. Krulisch and R. C. Axtmann, Nucl. Inst. Meth., 55 238 (1967).

La 69 L. D. Landau and E. M. Lifshitz, Course of Theoretical Physics, Vol. 5, Statistical Physics, Addison Wesley Pub. Co., Reading, Mass., 1969.

Li 63 J. Lindhard, V. Nielsen, M. Scharff and P. V. Thomsen, Mat. Fyss. Med. Dan. Vid. Selsk., 33 #10, #14 (1963).

Ma 74 E. des Mateosian, O. C. Kistner and A. W. Sangar, Phys. Rev. Lett., 33 596 (1974).

Mo 73 L. G. Moretto, Physics and Chemistry of Fission, Proceedings of the 3rd IAEA Symposium, Rochester, N.Y., 13-17 August 1973. p 329.

Mo 75 L. G. Moretto and J. S. Sventek, Phys. Lett., 58B 26 (1975).

Mo 75a L. A. Moretto, S. S. Kataria, R. C. Jared, R. Schmitt, and S. G. Thompson, Nucl. Phys. A255 429 (1975).

Mo 75b L. G. Moretto, Nucl. Phys. A247 211 (1975).

Mo 75c L. G. Moretto, R. P. Babinet, J. Galin and S. G. Thompson, Phys. Lett., 58B 31 (1975).

Mo 76 L. G. Moretto, J. Galin, R. Babinet, Z. Fraenkel, R. Schmitt, R. Jared and S. G. Thompson, Nucl. Phys., A259 173 (1976).

Mo 76b L. G. Moretto and J. S. Sventek, Invited paper to "Symposium on Macroscopic Features of Heavy Ion Reactions", ANL, Argonne, Ill., April 1-3, 1976.

Mo 76c L. G. Moretto and R. Schmitt, J. de Physique, Colloque C5, 37 109 (1976).

Mo 78 J. B. Moulton, E. J. Stephenson, R. P. Schmitt and G. J. Wozniak, Lawrence Berkeley Laboratory report, LBL-7101, Submitted to Nucl. Instr. Meth.

Mu 77 P. A. Muller, Science, 196 489 (1977).

Mu 77a P. A. Muller, L. W. Alvarez, W. R. Holley, and E. J. Stephenson, Science 196 521 (1977).

My 77 W. D. Myers, W. J. Swiatecki, T. Kodama, L. J. El-Jaick and E. R. Hief, Phys. Rev. C, 15 2032 (1977).

Ni 63 J. R. Nix, Proc. 3rd Conf. Reactions Between Complex Nuclei, Pacific Grove, Cal. April 14-18, 1963. Ed. A. Ghiorso, R. M. Diamond and H. E. Conzett, p. 306.

Ni 65 J. R. Nix and W. J. Swiatecki, Nucl. Phys. 71 1 (1965).

Ni 67 J. R. Nix, Ann. of Phys., 41 52 (1967).

Ni 69 J. R. Nix, Nucl. Phys., A130 241 (1969).

No 70 L. C. Northcliffe and R. F. Schilling, Nucl. Data Tables, A7 233 (1970).

No 74 W. Nörenberg, Phys. Lett., 52B 289 (1974).

No 75 W. Nörenberg, Z. Physik, A274 241 (1975).

No 76 W. Nörenberg, J. de Physique, Colloque 5, 37 141 (1976).

Pe 74 C. E. Pearson, Handbook of Applied Mathematics, Van Nostrad Reinhold Co., N.Y., 1974.

Qu 69 P. Quentin, J. de Physique, 30 497 (1969).

Re 65 F. Reif, Fundamentals of Statistical and Thermal Physics, McGraw-Hill, N.Y. 1965.

Ru 77 P. Russo, R. P. Schmitt, G. J. Wozniak, R. G. Jared, P. Glässel, B. Cauvin, I. S. Sventek and L. G. Moretto, Nucl. Phys., A281 509 (1977).

Sc 65 H. W. Schmitt, W. E. Kiker and C. W. Williams, Phys. Rev. B., 137 837 (1965).

So 56 A. Sommerfeld, Lectures on Theoretical Physics, Vol. 5, Thermodynamics and Statistical Mechanics, Academic Press, N.Y., 1956.

St 72 E. P. Steinberg, S. B. Kaufman, B. D. Wilkins and C. R. Gross, Nucl. Inst. Meth., 99 309 (1972).

St 78 F J. Stephenson, D. J. Clark, R. A. Gough, W. R. Holley, and A. Jain, (Lawrence Berkeley Laboratory report #LBL-659). To be published.

Sv 76 J. S. Sventek and L. G. Moretto, Phys. Lett. 65B 326 (1976).

Sv 78 J. S. Sventek and L. G. Moretto, Phys. Rev. Lett., 40 697 (1978).

Sw 72 W. J. Swiatecki, European Conf. on Nucl. Phys., Aix-en-Provence, France, June 26-July 1, 1972.

Va 73 R. Vandenbosch and J. R. Huizenga, Nuclear Fission, Academic Press, N.Y., 1973.

We 37 V. Weisskopf, Phys. Rev., 52 295 (1937).

We 76 M. P. Webb and R. Vandenbosch, Phys. Lett., 62B 407 (1976).

Wi 71 B. D. Wilkins, M. J. Fluss, S. B. Kaufman, C. E. Gross and E. P. Steinberg, Nucl. Inst. Meth., 92 381 (1971).

Wo 77 G. J. Wozniak, R. P. Schmitt, P. Glässel, and L. G. Moretto, Lawrence Berkeley Lab #LBL-6532, Submitted to Nucl [illegible].